ENGINEERING MATERIALS: METALS AND ALLOYS

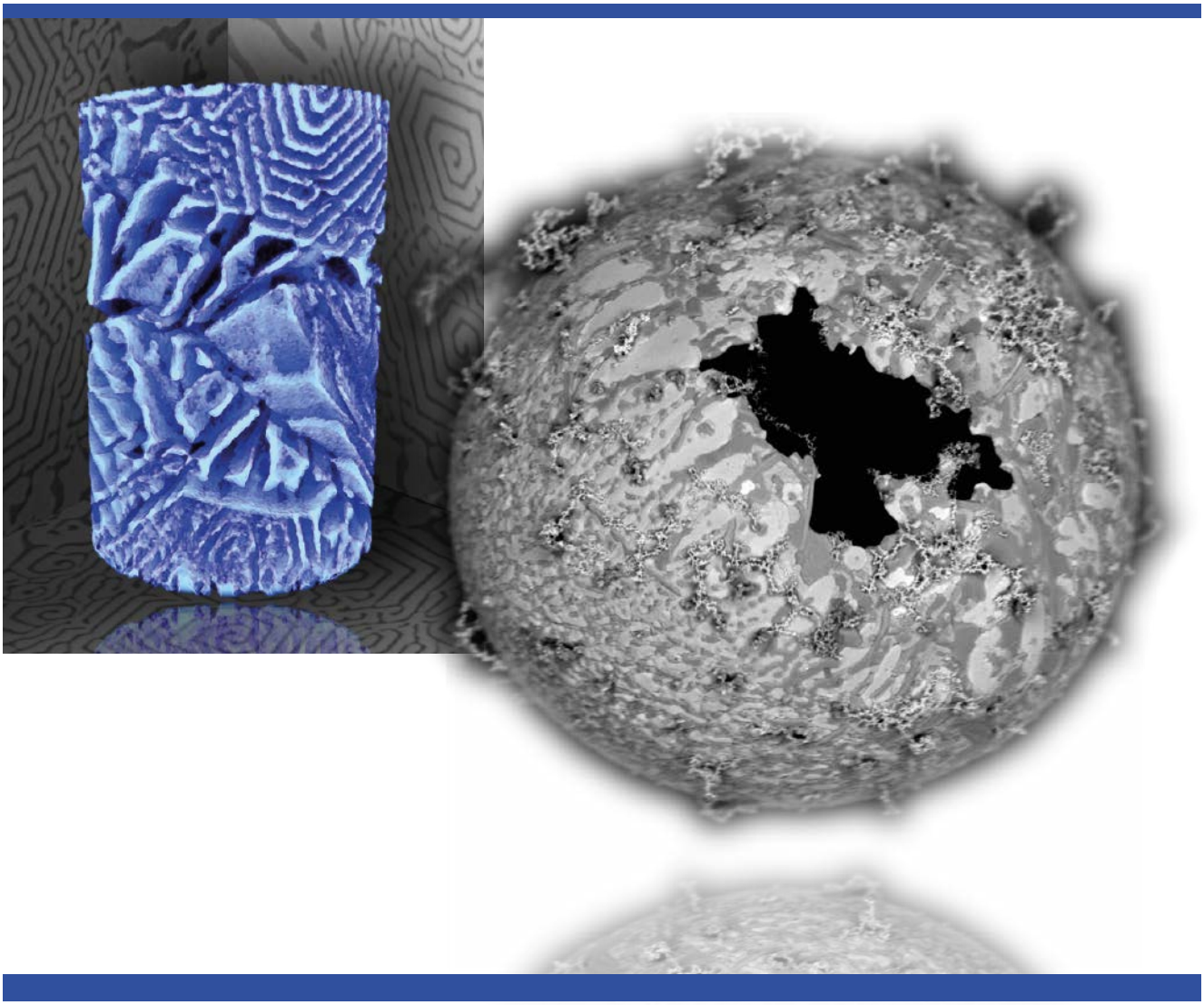

WILEY

Imprint

© Wiley-VCH GmbH
Boschstr. 12, 69469 Weinheim,
Germany
Email: info@wiley-vch.de

Carl Zeiss Microscopy GmbH
Carl-Zeiss-Promenade 10,
07745 Jena,
Germany
www.zeiss.com/microscopy

Editor-in-Chief:
Dr Christina Poggel

Senior Account Manager:
Dr. Stefanie Krauth

Printer:
AC medienhaus GmbH,
Wiesbaden, Germany

Editorial

From the dawn of early civilizations, the discovery of metals has played a pivotal role in shaping the course of human history, creating new revolutions along the way. Metals have played a foundational role in human development right from the creation of early metal tools and weapons to advancement of agriculture, construction and transport – ultimately forging the path to today's modern society. Each era, starting with the Gold, Bronze and Iron Ages, advanced our fundamental knowledge and has led us to discovering newer alloys along with innovative techniques to produce stronger and more customized materials. By the mid-20th century, all of the metals in the sub-transuranic periodic table had been discovered and several of their alloys with increasingly remarkable properties had been created.

However, prominent breakthroughs in the field of metallurgy and materials science began when early researchers started investigating why metals and alloys fail in certain ways. The pursuit of understanding materials to make them stronger, lighter and more reliable, unravelled the fact that there is a deep-rooted connection between the microstructure, properties, processing and performance of any given material. In parallel to the materials discoveries taking place, significant scientific breakthroughs in imaging using light, electron and X-rays paved the way for characterizing materials down to their atomic arrangements and enabling the study of materials in ways never before possible; **microscopy would soon become the centrepiece of materials science.**

More recently, with the synergies of technologies such as machine learning and advanced manufacturing methods such as 3D additive manufacturing, far more complex materials can be explored. Today's metals research is propelled by the requirement to adapt the world to a low carbon economy, free of fossil fuel pollution. This paradigm shift requires stronger, lighter and more durable alloys and advanced steels to lead us into the middle of the 21st century and beyond.

This booklet aims to give you an overview of recent achievements in engineering materials research. A brief introduction details some advanced microscopy techniques from ZEISS and their specific benefits for your research. This is followed by a selection of peer-reviewed articles from various Wiley journals, condensed into a digestible format with links to the original article DOIs.

In a concluding interview, Dr Kaoru Sato from JFE-Techno-Research Corporation shares his views on current challenges and future developments in microscopy applications for engineering materials, particularly in metals and alloys.

Dr Benjamin Tordoff
Head of Materials Science Sector
ZEISS Research Microscopy Solutions

Dr Hrishikesh Bale
Market Solutions Manager
ZEISS Research Microscopy Solutions

Contents

3 Editorial

5 Introduction

9 Effects of Initial δ Phase on Creep Behaviors and Fracture Characteristics of a Nickel-based Superalloy
Lin YC, Yin L-X, Luo S-C, He D-G, Peng X-B

13 Ultrastrong and Ductile Soft Magnetic High-entropy Alloys via Coherent Ordered Nanoprecipitates
Han L, Rao Z, Filho IRS, Maccari F, Wei Y, Wu G, *et al.*

18 The Role of Microstructural Constituents on Strength–Ductility–Local Formability of a Transformation-Induced-Plasticity-Aided Bainitic Steel
Tang S, Huifang L, Jianping Li H, Liu Z, Wang G

22 Enhancing Ductility and Fatigue Strength of Additively Manufactured Metallic Materials by Preheating the Build Platform
Nezhadfar PD, Shamsaei N, Phan N

27 Multiscale Additive Manufacturing of Metal Microstructures
Ercolano G, Zambellii T, van Nisselroy C, *et al.*

31 Multi-step Crystallization of Self-organized Spiral Eutectics
Moniri S, Bale H, Volkenandt T, *et al.*

36 X-ray Microtomography of Thermal Cycling Damage in Sintered Nano-silver Solder Joints
Regalado IL, Williams JJ, Joshi S, Dede EM, Liu Y, Chawla N

40 3D Grain Reconstruction from Laboratory Diffraction Contrast Tomography
Bachmann F, Bale H, Gueninchault N, Holzner C, Lauridsen EM

44 Advanced Microscopy Characterization of Metals and Alloys: an Interview with Kaoru Sato

Introduction

New stronger, tough, durable, lightweight and fracture-resistant materials open doors to new technologies, whether it is in the applications of high-speed air or ground transportation, long lasting and economical construction, safe nuclear installation, or more advanced space exploration technologies. Designing and developing the engineering materials for tomorrow's innovation challenges demands an ever-better understanding of the complex connections between processing, properties and the underlying structures that, collectively, influence how a material performs and why it might fail.

The demands for materials to meet a variety of structural needs has spawned advancements in an assortment of fields including advanced alloys with exceptional corrosion resistance, high temperature performance, fatigue and fracture resistance and high strength-to-weight ratio composite structures.

Developing and improving these types of engineering materials takes a detailed understanding of the connections between processing, structure, performance and properties throughout the material's life cycle. This is even more important as advanced technologies such as additive manufacturing become increasingly prolific and more complex. Microscopy characterization techniques are central to this paradigm, enabling observation of the microstructure of any given material revealing its grain structure, crystallographic texture, phases and phase transitions, inclusion and impurity distributions, and surface finish.

Among all of the engineering materials classes, metals and alloys present the widest range of properties that can be highly tailored through processing as per the applications needs, for example strength, hardness, malleability, good electrical and thermal conductivity, and corrosion resistance. Commercial metal alloys attempt to combine beneficial mechanical, electrical or chemical properties in order to create metals more useful for particular applications than any of their component elements. Some of the key characteristics of metals that make them an attractive and sought after engineering material are the ease of production, availability, scalability in production, recyclability and most importantly the ability to control properties through processing and microstructure control.

In contrast to traditional development approaches in metals and alloys, present day research engages significantly in engineer-

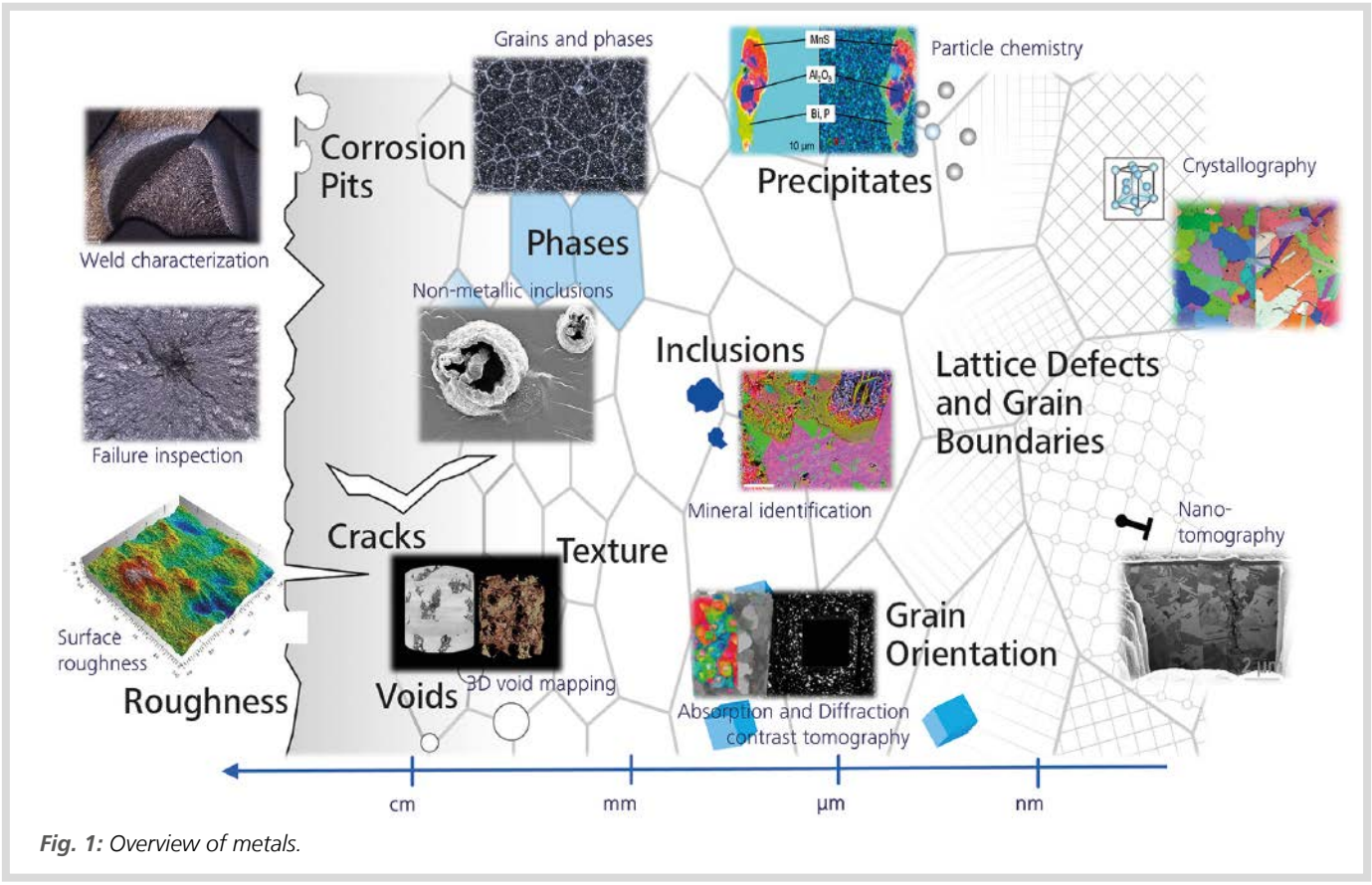

Fig. 1: Overview of metals.

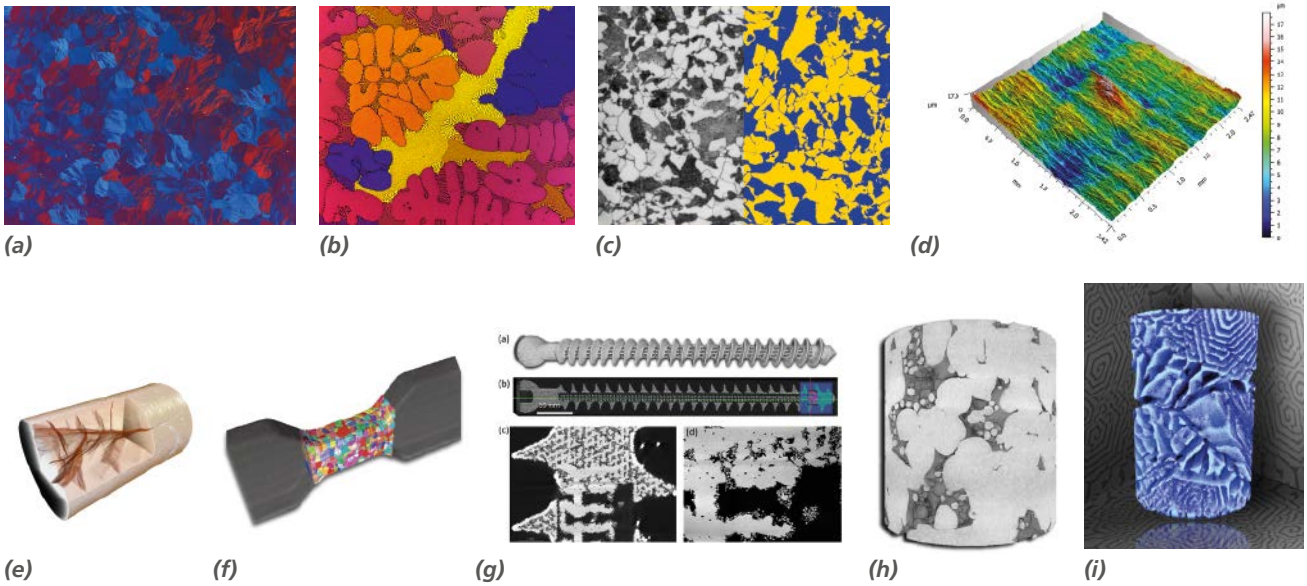

Fig. 2: *(a) Light microscopy image of a pure magnesium sample using polarization contrast shows the structural anisotropy; (b) polarization contrast light microscopy image from a Barker etched anodized AlNi3.5 sample; (c) ferrite and pearlite phase in steel imaged using light microscopy and quantitatively analyzed; (d) laser polished surface of stainless steel test piece. 3D view of colour-coded height map shows surface texture of areas with different process parameters; (e) non-destructive 3D rendering of crack networks formed due to corrosion fatigue in the shank section of a load-bearing steel bolt (XRM); (f) 3D grain map of an Al-4wt%Cu sample with gauge section dimension of (length) 1.25 mm, (width) 1.0 mm and (thickness) 0.5 mm. Sample scanned using Lab based Diffraction Contrast Tomography (LabDCT); (g) volumetric rendering of a 3D printed Ti-6Al-4V screw (top). Blue dotted line indicates cross-sectional view from a region of interest scan, (bottom) reveals local microstructure and defects such voids and unsintered powder particles; (h) 3D volumetric rendering of sintered CoCr particles. The consolidated bulk after sintering and portions of unsintered powder can be observed; (i) 3D rendering of a reconstructed nanoscale X-ray tomography dataset obtained from a Zn–Mg spiral eutectic sample.*

ing the microstructure in order to enhance mechanical, thermal and electrical properties. Using data-guided precise control of the grain size, engineering the grain boundaries and distribution of precipitates and controlling the presence of inclusions, voids and other defects, remarkable improvements in the properties of traditional metals and alloys can be achieved. At the heart of engineering such complex materials lie material characterization techniques.

As shown in Figure 1, the microstructure of any metal or alloy encompasses diverse features ranging from surface roughness, pits and cracks; grain characteristics (size, crystallographic orientation and morphology), texture, twinning, voids, inclusions and precipitates at the 10–100 µm range; and ultimately nanoscale features such as dislocations, nano-precipitates, lattice defects, crack initiation sites and nano-crystalline grain features. Such a detailed microstructural evaluation drives the need to include several microscopy techniques providing different imaging modalities, each revealing uniquely important pieces of information. The mechanisms that individually contribute to strength, toughness and other important properties can originate from very different length scales in a material's structural architecture and it is very important to capture their interplay in their native state. This has led to the emergence of correlative microscopy approaches that combine information gathered from various modalities at different length scales, enabling researchers to gather comprehensive information for a given material system.

Understanding impact of macroscale features on material properties and performance

At the macroscale, materials insights related to geometric defects, surface roughness, cracks, voids and inclusions can be characterized effectively using light and X-ray microscopy methods (Figure 2). Through a variety of modes including brightfield, darkfield and polarization contrast, light microscopy can generate a wealth of information readily on metals samples. While light microscopy provides rapid information from the surface over a wide area, X-ray methods enable peering into the sub-surface non-destructively delivering three-dimensional (3D) information on complex microstructural features such as crack networks, void distributions, etc. With advances in diffraction contrast tomography, 3D crystallographic grain characterization is now possible. This non-destructively delivers information on grain size, morphology and orientations, which provides an early macroscale overview of the sample before needing further high resolution insights from some of the electron microscopy techniques. With its ability to capture the microstructural information in 3D in a single snapshot, X-ray microscopy methods are particularly best suited for new-age manufacturing methods such as 3D printing where structural parts with an ever increasing material and structural complexity are being produced. Recent advances in

X-ray microscopy now enable 3D nanoscale microstructural characterization, providing information on nanoprecipitates, eutectic microstructures, etc.

Comprehensive characterization from micro- to nanoscale

Electron microscopy techniques have become an integral part of materials characterization workflow and to many researchers the scanning electron microscope (SEM) is the go-to 'Swiss-knife' among all of the characterization techniques. SEM provides a unique opportunity for characterizing materials from micron to sub-nanometer scale, through a variety of imaging modalities, all on a single imaging platform. Offering the flexibility to augment imaging with a wide-ranging detector probe landscape, an SEM instrument readily delivers critical information related to chemical makeup, crystallographic microstructure (Figure 3) and phase identification. Within the area of metals and alloys analysis, an SEM can quickly deliver qualitative as well as quantitative information on inclusions, precipitates and other morphological features. Advanced detector technology with improved secondary and backscattered electron imaging performance, along with highly refined electron beam column designs, supports combining information from multiple detectors, delivering exceptional contrast that can discern crystal defects, crystal orientations, and subgrain information such as twinning and slip band formations (Figures 4 and 5).

Surface characterization of fracture at high resolution delivers information necessary for the determination of the fracture mode and in the analysis of crack propagation, successively enables researchers to study the relationship between microstructure and fracture resistance. These methodologies are an integral part of the root cause analysis workflows used to study structural failures of critical parts used in engineering applications. Furthermore, these imaging modalities can also be combined with *in situ* imaging for microstructure characterization during deformation.

A gamut of modalities to assess grain characteristics and deformation behaviour

In addition to the core modality of electron backscattered imaging, additional probes enable other important measurements that are highly essential to metals and alloys research. Energy dispersive X-ray spectros-

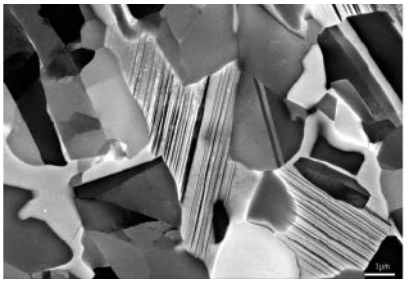

Fig. 3: *Scanning electron microscopy (SEM) delivers extremely high contrast of crystal orientations and defects in the high temperature alloy $TiAl_2$. $TiAl_2$ is an alloy of intermetallic compounds with lower density and superior oxidation resistance. The image is taken with the AsB detector at 15 kV. The presence of crystal defects and the preferential crystalline orientations observed in such images may be correlated with improved desired mechanical properties.*

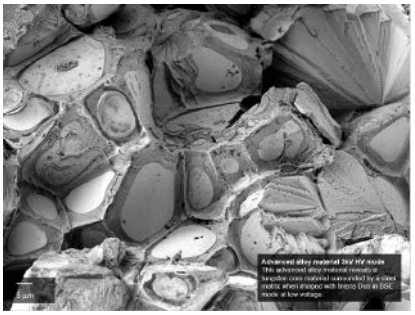

Fig. 4: *Advanced alloy material imaged at 3kV in HV mode. This advanced alloy material reveals a tungsten core material surrounded by a steel matrix when imaged with Inlens Duo in BSE mode at low voltage.*

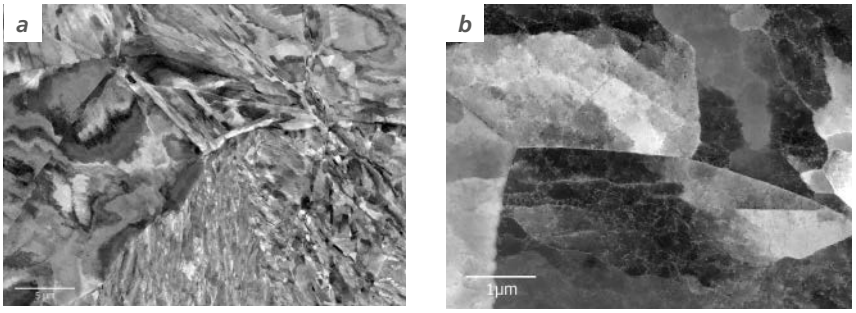

Fig. 5: *Channeling contrast imaging of dislocation networks in highly deformed stainless steel. The sample is imaged at 30 kV electron beam energy. (a) Strong crystalline orientation changes within the grains. (b) Dislocation networks formed by the deformation.*

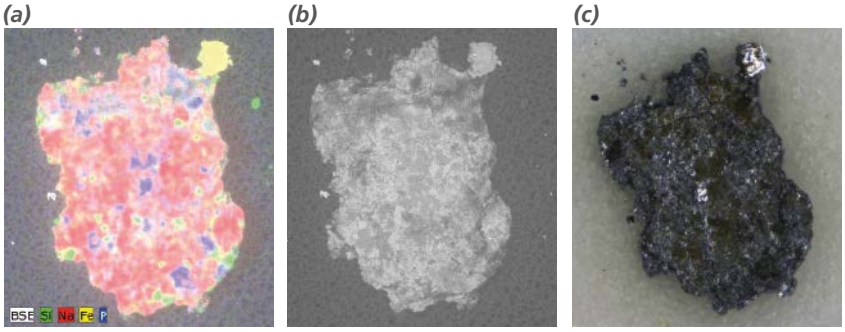

Fig. 6: *Particulate contamination is an important aspect of technical cleanliness. Multi-modal SEM imaging of a contamination particulate provides: (a) elemental composition though EDS mapping, (b) and (c) morphological details through backscattered electron microscopy and light microscopy, respectively.*

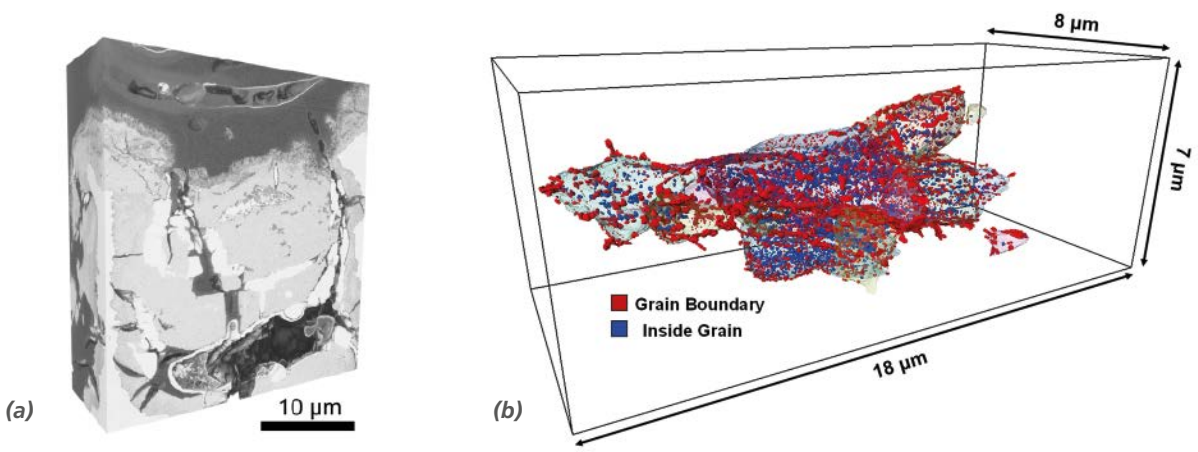

Fig. 7: *(a) High resolution serial section FIB-SEM tomography (8 nm/voxel) from a correlative microscopy experiment to study the process of intergranular corrosion observed in a magnesium alloy. Sample courtesy of the University of Manchester; (b) 3D FIB-SEM tomography data on the precipitate distribution in aluminum 7075 alloy. The 3D data provides quantitative information on the spatial distribution of precipitates with respect to the grain boundaries. Sample courtesy of Prof. N. Chawla, Purdue University.*

copy (EDS) enables a highly detailed and correlated chemical analysis of precipitates and inclusions (Figure 6). Understanding of the chemical makeup and distribution of the inclusions and precipitates enables metallurgists to modify the materials processing route and chemistries and fine tune the properties and performance of a metal or alloy system.

The electron backscattered diffraction (EBSD) technique brings an exceptional capability to electron microscopy by allowing the measurement of grain size, crystallographic orientation, texture, and grain boundary character distribution with a sufficiently high resolution down to 10 nm. EBSD enables material characterization at different length scales providing information on a number of key microstructural characteristics. Since the mechanical properties of metals and alloys are strongly coupled to several microstructural aspects such as the size, shape, and distribution of grains, the presence of texture, grain boundary character, and also the grain boundary plane distribution, EBSD is one of the prime characterization methods used in the study of metals and alloys.

The knowledge of the distribution of lattice defects such as dislocations and stacking faults within grains and their location with respect to grain boundaries and orientations offers key insights into the deformation behaviour and fracture properties of metals and alloys. Electron channelling contrast imaging (ECCI) is the adaptation of scanning electron microscopy to directly observe the lattice defects quantitatively using electron channelling along crystal planes. The technique can also be combined with *in situ* deformation of metals samples to make direct observations of the formation of dislocation networks under the influence of mechanical loads and elevated temperatures.

Precise, high-throughput cross-sectioning for high-resolution sub-surface microstructural characterization

Site-specific characterization using a suitable probing modality is extremely important in order to isolate and understand many of the underlying mechanisms that operate at the microstructural length scale. The first step in such a study is to precisely target a feature of interest, for example, a unique void feature, a precipitate located along a certain grain boundary or a specific grain boundary with unique boundary surface characteristics. Focused ion beams (FIB) offer the excellent capability of precise sectioning to reveal the sub-surface features, while maintaining a virtually deformation free microstructure. Thin serial sectioning using FIB milling combined with standard live SEM imaging (Figure 7) or a combination of EDS or EBSD imaging (Figure 8) enables high resolution multichannel 3D tomography focusing on specific sub-surface sites. This facilitates the investigation of grain boundary interactions with precipitates, influence of grain orientation and grain boundary surface on the material properties such as fracture toughness, corrosion, thermal and electrical properties in metals and alloys. More recently even more massive material removal, at least three orders of magnitude more than traditional FIB milling has been made possible by incorporating femto-second lasers on the FIB-SEMs. This new rapid milling capability enables high throughput characterization of larger sample areas or deeper regions of interest (Figure 8).

Fig. 8: *Laser-polished sample surfaces produce satisfactory EBSD grain maps without the need for Ga-FIB polishing steps in cases where a quick overview of a large area of the sample is sufficient. For deeper analysis and high resolution grain maps, a region of interest can be selected from the overview EBSD maps and used to run high resolution grain mapping after gallium polishing.*

Effects of Initial δ Phase on Creep Behaviors and Fracture Characteristics of a Nickel-based Superalloy

Lin YC, Yin L-X, Luo S-C, He D-G, Peng X-B

Literature review on creep behaviour of Ni-superalloys

Nickel-based superalloys are predominantly used in structural components such as turbine blades, guide vanes, and turbine discs with service temperatures near to or above 700°C. Particular attention is given to the creep properties at elevated temperatures while designing these components. The creep behaviour of Ni-based alloys involves time-dependent plastic deformation with varying stresses, and noticeable creep deformation with an increase in temperature and stress leading to crack formation and growth. Therefore, many researchers have attempted to understand the creep behaviour and related fracture mechanisms of different Ni-based alloys, for example, FGH97, superalloy reinforced with HF carbides, Rene N4, GH4169, Inconel-713C, Inconel 718, Allvac 718Plus, etc.

It has been found that Inconel 718 with δ phase on the grain boundaries has a high creep rate, whereas size of γ" precipitate determines the steady-state creep rate. The creep resistance can be enhanced by the presence of γ' and γ" precipitates via double ageing heat treatment. The combined effect of localized necking and microvoid coalescence leads to the intergranular fracture, which is the main failure mode for Inconel 718. Micro-twinning is observed as a dominant creep deformation mechanism in Allvac 718Plus. The focus of the study here aims at furthering our understanding of the influence of the δ phase on high temperature creep and fracture behavior of nickel-based superalloys. Different volume fractions of initial δ phases are obtained via double ageing treatments followed by uniaxial creep tensile tests conducted at elevated temperatures, which are used to analyse the effects of initial δ phase on the creep features and fracture mechanism of GH4169 superalloy.

Experimental details

The cylindrical creep samples of 50 mm gauge length and 10 mm diameter were made according to ISO 204:2009 from a GH4169 superalloy. After solution treatment at 1040°C for 45 min, samples were further aged with five different treatments (shown in Table 1) to understand the influence of initial δ phase on the creep features and fracture behaviour. For the uniaxial creep experiments, the samples were heated to 670°C and soaked for 20 min to ensure homogeneous temperature distribution. The tests were conducted on the MTS-GWT2015 test machine with applied stress of 700 MPa and the creep strain was measured through the averaging extensometer system. The initial microstructures of etched samples were observed using optical microscopy and the morphologies of creep-ruptured specimens were examined using a ZEISS-EVO-M10 scanning electron microscope.

Table 1: The detailed ageing treatment procedures

Case ID	Ageing treatment processing
1	720°C x 8h/FC + 620°C x 8h/AC
2	900°C x 2h/AC + 720°C x 8h/FC + 620°C x 8h/AC
3	900°C x 4h/AC + 720°C x 8h/FC + 620°C x 8h/AC
4	900°C x 8h/AC + 720°C x 8h/FC + 620°C x 8h/AC
5	900°C x 16h/AC + 720°C x 8h/FC + 620°C x 8h/AC

Note: *AC indicates the air cooling to the room temperature, while FC represents the furnace cooling to 620°C at 50°C h^{-1}.*

Microstructures after solution and ageing treatments

Figure 1 shows the microstructure of the etched samples. Fine equiaxed grains, clear grain boundaries, and annealing twins can be observed in case 1 (Figure 1a), whereas presence of a small amount of δ phase precipitate is observed at the twin boundaries and grain boundaries for case 2 (Figure 1b) and case 3 (Figure 1c). For case 4 (Figure 1d), short rod-like δ phases are observed at twin boundaries and grain boundaries, whereas few of the spherical δ phases appear within grains. The volume fraction of δ phases significantly increases for case 5 (Figure 1e), where long needle-like δ phases precipitate from the matrix.

Image-Pro Plus 6.0 software has been used to calculate the volume fraction of initial δ phase in each case and the average volume fraction is statistically measured as 1.62%, 2.56%, 4.56%, and 10.8% for cases 2, 3, 4, and 5 respectively. Almost no δ phase is observed for case 1. The precipitation process of δ phase is typically diffusion-controlled and thus longer ageing time

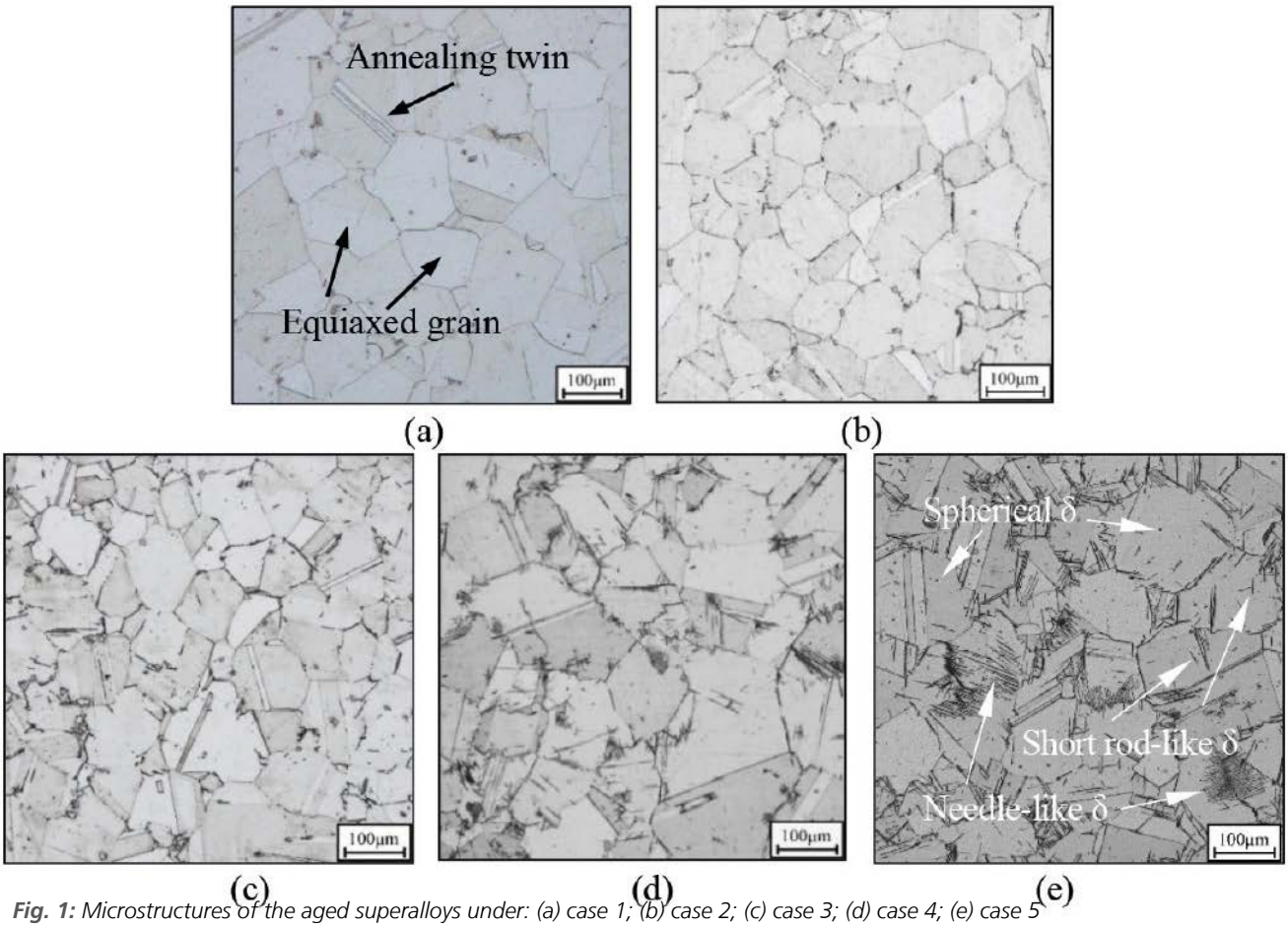

Fig. 1: Microstructures of the aged superalloys under: (a) case 1; (b) case 2; (c) case 3; (d) case 4; (e) case 5

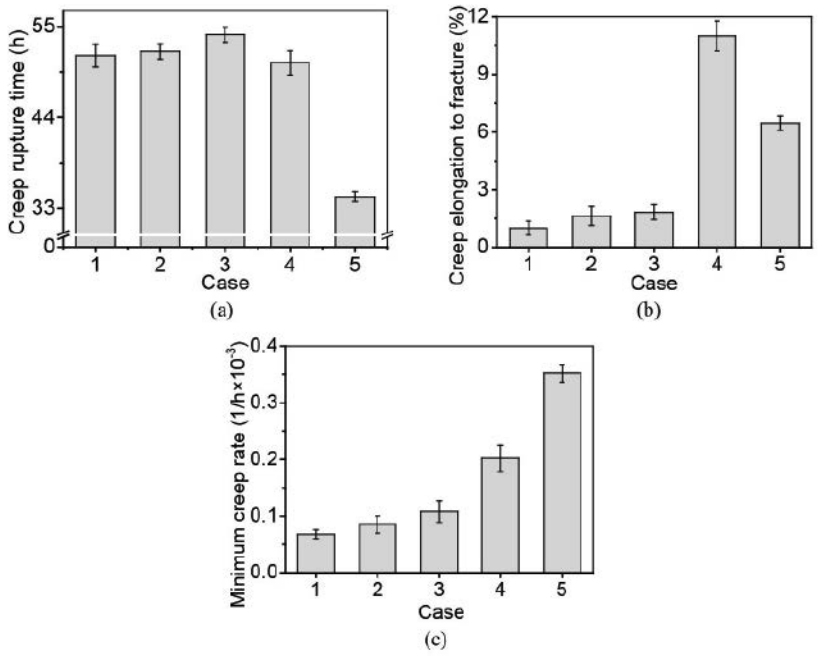

Fig. 2: Creep properties of the aged superalloy: (a) creep rupture time; (b) elongation to fracture; (c) minimum creep rate

can provide enough energy and duration for the nucleation and growth of δ phase. So, the volume fraction of the initial δ phase increases with ageing time, and its distribution becomes uniform.

Creep behaviour of the aged superalloy

The aged superalloys show three distinct creep stages – primary, steady-state, and accelerating stages. With an increase in creep time, the creep rate rapidly decreases to a minimum, followed by either a steady-state or a rapid increase. The initial decrease of creep rate is associated with the rapid increase of dislocation density as a result of work hardening. During steady-state creep, the accumulation of void or crack damage and coarsening of the second phase weakens the creep deformation resistance. The increased creep rate is due to the aggregation of the creep micro-voids and the reduction of effective bearing area.

The variations of creep rate with creep time are not significant for cases 1–3, when ageing time is short but becomes very distinct for cases 4 and 5. Figure 2 shows the creep properties of the aged superalloy including creep rupture time, elongation to fracture, and minimum creep rate. The creep rupture time (Figure 2a) initially increases to a maximum value (about 54 hours), followed by a rapid decrease. This is attributed to the compact grain structure in cases 1–3 (Figure 1a–c), which effectively delays the initiation and propagation of micro-cracks along the grain boundaries in the early creep stage leading to higher creep rupture time.

No obvious changes in the elongation to fracture are observed for cases 1–3, whereas it sharply increases for case 4 and falls for case 5 (Figure 2b). The volume fraction of δ phases at the grain boundaries gradually increases from case 3 to case 4 (Figure 1c, d), thus promoting the pinning effect of the initial δ phase on grain boundary sliding for case 4 over case 3. The presence of δ phases at grain boundaries further benefits the ductility and toughness.

When minimum creep rates of different aged superalloys are considered, the strong presence of coherent γ" phases and the occasional presence of δ phases at the grain boundaries lead to relatively low minimum creep rates for cases 1–3 compared with cases 4 and 5 (Figure 2c). The presence of δ phase accelerates the creep deformation at the early creep stage and increases the minimum creep rate, which in turn gradually decreases the time to 0.2% and 0.5% creep strains with increased ageing time at 900°C. But the presence of a large number of needle-like δ phases deteriorates the creep properties particularly for case 5.

Fracture morphologies and fracture mechanisms

Figure 3 shows the SEM images indicating fracture surface morphology of the creep-ruptured specimens. Case 1 shows smooth fracture characteristics with rock-candy-block morphology, where long and large wedge cracks propagate along the grain boundaries indicating typical intergranular fracture (Figure 3a, b). Similar failure modes are observed for both case 2 (Figure 3c, d) and case 3 (Figure 3e, f), but the wedge cracks appear smaller with increase in ageing time at 900°C. For case 4, non-uniformly distributed thin shallow dimples and some bright white tearing edges appear in the fracture surface indicating a typical ductile intergranular fracture mode (Figure 3g, h). Presence of facets and small cracks in the

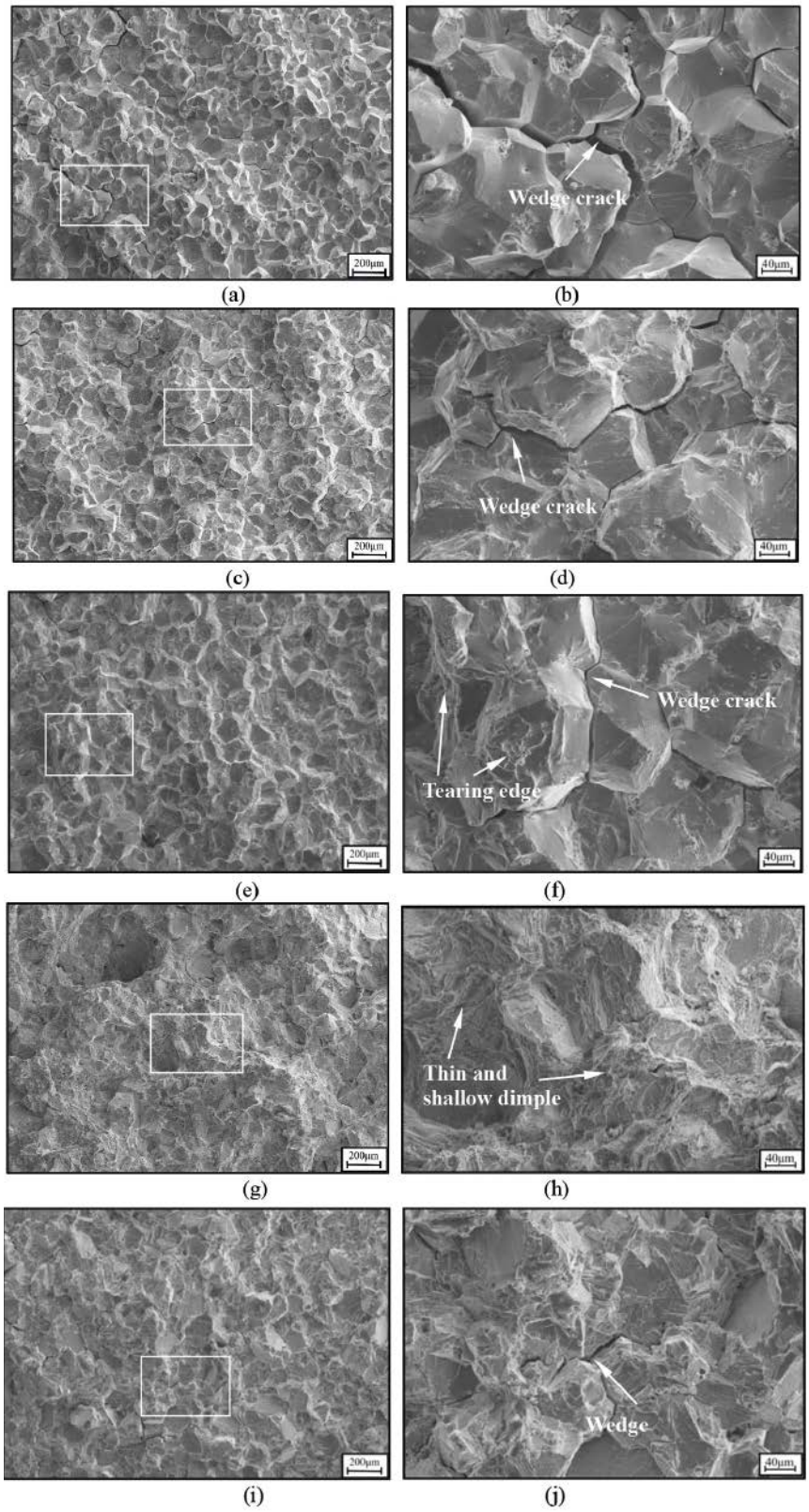

Fig. 3: SEM fractographs of creep-ruptured nickel-based superalloy under: (a,b) case 1; (c,d) case 2; (e,f) case 3; (g,h) case 4; (i,j) case 5

fracture surface of case 5 denotes typical intergranular cleavage fracture (Figure 3i, j).

This failure behaviour can be explained by their respective microstructures. The dispersive presence of γ' and γ" precipitates strengthens the grains in a transgranular direction. The grain boundaries parallel to the external stress are easy to slide but tend to crack when they are perpendicular to the external stress. High temperature accelerates the diffusion rate of atoms along the grain boundaries, which in turn decreases the resistance to deformation. The grain boundary sliding therefore occurs easily when long-term external stress is applied. Cases 1–3 have smooth and straight grain boundaries with fewer δ phases (Figure 1a – c), so the boundaries can slide easily in the later creep stage leading to the elongation to fracture to less than 2% (Figure 2b). Moreover, the length and width of cracks are gradually reduced with the increase in ageing time from 0 hours (case 1) to 4 hours (case 3), and the pinning effects of δ phase are strongly relieved when the ageing time is increased to 8 hours. A plastic deformation zone is formed when the strengthening element (Nb) in γ" phase near the grain boundary is consumed resulting in a straightaway increase in ductility and therefore elongation to fracture. Particularly for case 4, the elongation to fracture reaches 11% and the ductile intergranular fracture becomes the failure mode. When the ageing time is further increased to 16 hours, a large number of needle-shaped δ phases at the grain boundaries weaken the bonding strength and accelerates the initiation and expansion of cracks at grain boundaries. Therefore, a reasonable initial δ phase hinders grain boundary sliding and enhances the elongation to fracture, whereas excessive initial δ phase reduces the creep resistance of the aged superalloy, and accelerates the failure process.

Summary

The influence of initial δ phase on the creep features and fracture behaviour of GH4169 superalloy is studied. With an increase in the volume fraction of initial δ phase, the minimum creep rate increases, while the rupture time and elongation to fracture show initial increase followed by decrease. A reasonable amount of initial δ phase at the grain boundaries improves creep ductility and prolongs creep rupture time. The failure mode changes from a typical intergranular fracture to the mixed fracture pattern of ductile intergranular and cleavage fracture with increasing volume fraction of initial δ phase. A good creep property with accepted morphology and content of initial δ phase has been obtained by the double ageing treatment at 900°C for 4 hours.

Digest of
Lin YC, Yin L-X, Luo S-C, He D-G, Peng X-B; Effects of initial δ phase on creep behaviors and fracture characteristics of a nickel-based superalloy; Advanced Engineering Materials 2018, 20, 1700820.

Ultrastrong and Ductile Soft Magnetic High-entropy Alloys via Coherent Ordered Nanoprecipitates

Han L, Rao Z, Filho IRS, Maccari F, Wei Y, Wu G, et al.

Introduction

Soft magnetic materials (SMMs) have high demand in electrical power generation, transformation, and sensor industries due to their high saturation magnetization (M_s), permeability, resistivity, low coercivity (H_c), and core losses. Under high mechanical loads, SMMs typically require excellent soft magnetic performance, high strength and good ductility. Several SMMs show a good combination of strength and soft magnetic properties, but their brittleness and dimensional restrictions often limit the application. Many studies have already addressed the excellent mechanical, thermal, electrical, and magnetic properties of high-entropy alloys (HEAs), among which ultrafine-grain FeCoNi$Cu_{0.2}Si_{0.2}$ HEA produced via melt-spinning particularly shows a promising balance between strength and soft magnetic properties at the expense of modest (~7%) ductility. Most of the mechanical strengthening approaches cause higher magnetic hysteresis losses, therefore three different ways have been introduced to obtain an optimal balance between strength, ductility, and soft magnetic properties. Introducing a high volume fraction of coherent and ordered nanoprecipitates into the HEA matrix is a possible way, where nm-sized precipitates do not interact with ~50 nm to a few μm thick Bloch walls in soft magnetic materials. The other two routes to maintain a good combination of mechanical and soft magnetic properties are the incorporation of coherent precipitates into the alloy matrix and increasing the degree of super-lattice ordering in a nanocrystalline alloy. In this study, the first route has been implemented with a non-equiatomic $Fe_{35-x/3}Co_{30-x/3}Ni_{30-x/3}Ta_5Al_x$ (x=3,5,7 at%) HEA system, where ferromagnetic elements (Fe, Co, Ni) form a strong and ductile magnetic matrix, and non-ferromagnetic elements (Ta, Al) are likely to create ordered nanoprecipitates coherent with the matrix.

Results and Discussion

The as-cast 10-mm thick base $Fe_{35}Co_{30}Ni_{30}Ta_5$ (at%) HEA plates (B-HEA) were hot-rolled at 1473K to 50% thickness reduction,

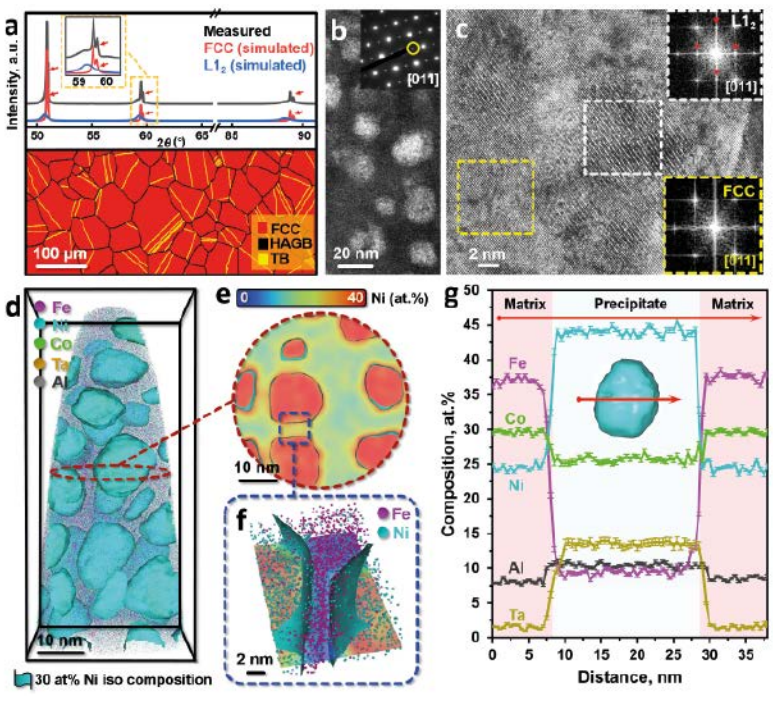

Fig. 1: Microstructure of the 7Al-HEA from micro- to near atomic-scale, (a) XRD pattern and EBSD phase map. The Cu Kα2 radiation causes additional diffraction peaks, marked by the red arrows. (b) Centered dark-field TEM image of the precipitates using the (011) superlattice spot (see inset, highlighted by a yellow circle). (c) HRTEM image of the nanoprecipitation hardened HEA. The fast Fourier transformation (FFT) image (bottom right) acquired from the region highlighted by the yellow rectangle confirms the fcc structure with the zone axis of [011]. By contrast, the white rectangle region's FFT image (top right) reveals a pattern with pronounced superlattice spots. (d) 3D reconstruction map of an APT tip highlighting the nano-region showing the distribution of Fe and Ni atoms. (e) 2D projection of the NI concentration slice acquired from the central part of the APT tip shown in (d). (f) Enlarged view of the groove region showing the distribution of Fe and Ni atoms. (g) 1D compositional profiles showing the compositional changes across a selected precipitate along the red arrow shown in the inset. Error bars in (g) refer to the standard deviations of data points.

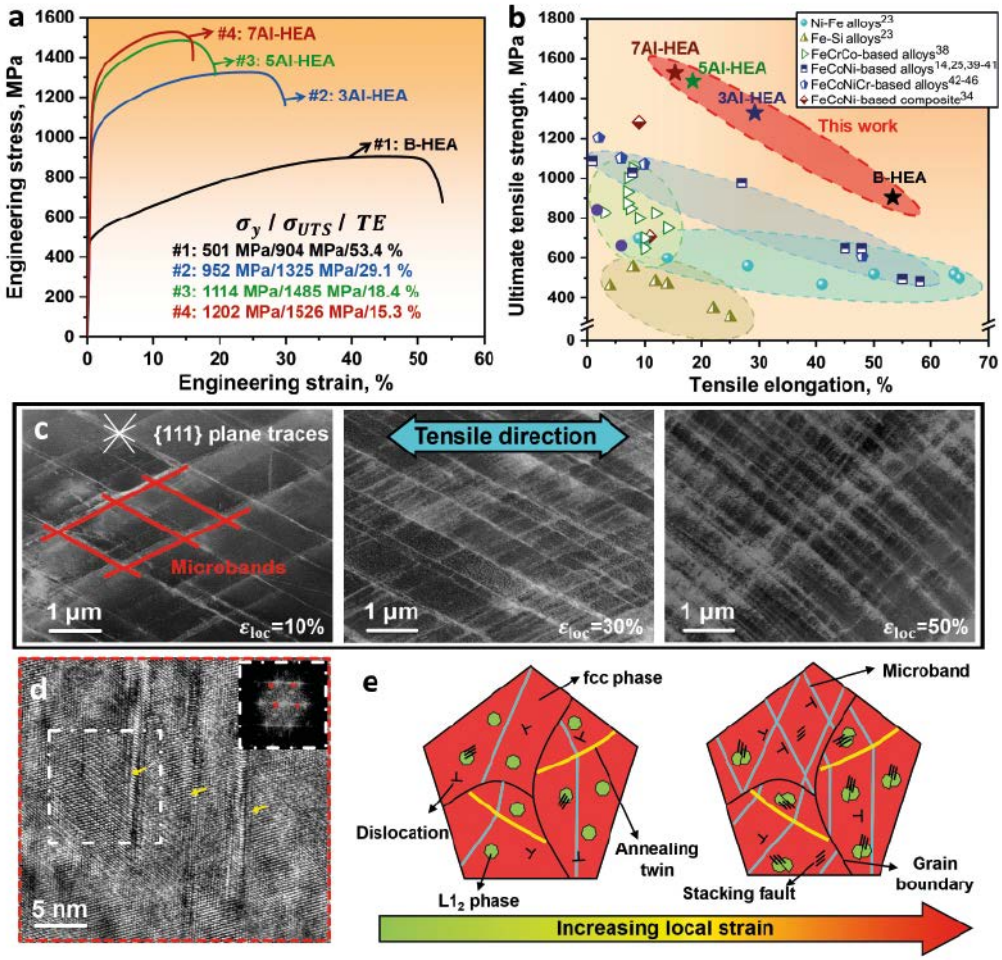

Fig. 2: Mechanical behaviour and deformation mechanisms of the 7Al-HEA. (a) Room temperature tensile stress-strain curves for the B-HEA, 3Al-HEA, 5Al-HEA, and 7Al-HEA. σ_y, σ_{UTS}, and TE represent the yield strength, the ultimate tensile strength and the tensile elongation, respectively. (b) σ_{UTS} - TE profiles of various classes of soft magnetic materials, including the newly developed soft magnetic HEAs investigated in this work. (c) Electron channeling contrast imaging analysis revealing the evolution of the substructure in the 7Al-HEA with increasing local strain during tensile deformation; the distance between the parallel microbands decreases with increasing local strain. (d) HRTEM image of a region of ε_{loc} = 50% showing that the $L1_2$ nanoprecipitates have been sheared by nano-spaced stacking faults (SFs); the inserted FFT pattern confirms the ordered structure of the nanoprecipitates in the fcc matrix. (e) Schematic illustration of the micro-processes in the precipitate-containing HEAs during plastic straining.

followed by 10-min homogenization at the same temperature and water quenching. The homogenized $Fe_{35-x/3}Co_{30-x/3}Ni_{30-x/3}Ta_5Al_x$ HEAs containing 3at%, 5at%, and 7at% Al are termed as 3Al-HEA, 5Al-HEA, and 7Al-HEA respectively. Figure 1a shows the FCC matrix of 7Al-HEA with an average grain size of 65.3±10.3 μm, whereas B-HEA shows a single FCC phase structure having 64.8±9.8 μm average grain size as revealed by XRD and EBSD analyses. The microstructure of 7Al-HEA was further characterized by atom probe tomography (APT) and TEM. Figure 1b shows the dark-field TEM image of the homogeneously distributed nanoprecipitates with an average size of 13.5±2.5 nm. Figure 1c shows an HR-TEM image, where the fast Fourier transformation (FFT) pattern acquired from a nanoprecipitate reveals an ordered structure. Figure 1d shows a 3D reconstruction map of an APT tip highlighting the nanoprecipitates, where the average volume of near-spherical $L1_2$ nanoprecipitates (2294±125 nm³) is found below the critical size for the sphere-to-cuboid shape transition based on Khachaturyan's theory. Figure 1e shows a cross-sectional 2D projection of the Ni concentration slice acquired from the APT tip's central part. Two representative precipitate/matrix interfaces indicated by the blue dashed square are chosen for further characterization and the enlarged views in Figure 1f prove Ni and Fe enrichments in the precipitates and matrix respectively. Figure 1g shows 1D compositional profiles acquired across a selected precipitate, where Ni, Ta, and Al are preferentially partitioned into the $L1_2$ nanoprecipitates. These profiles show a stoichiometry of $Ni_{42}Co_{24}Ta_{14}Al_{11}Fe_9$ (at%), whereas the FCC matrix holds a Fe-Co-rich composition of $Fe_{37}Co_{30}Ni_{24}Al_8Ta_2$ (at%). The chemical

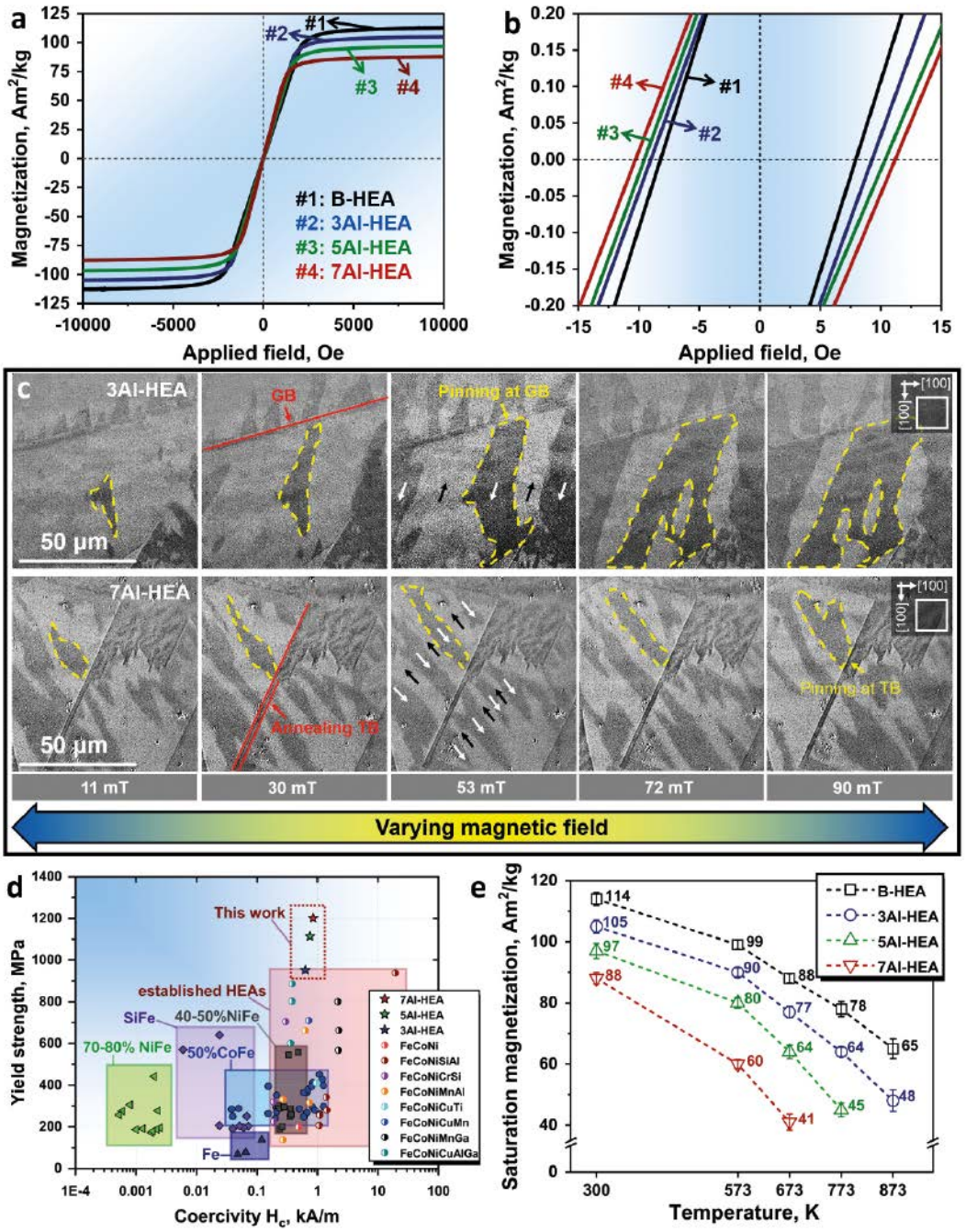

Fig. 3: Soft magnetic behaviour of the HEAs and associated Bloch wall pinning mechanisms. (a) Hysteresis loops acquired up to ± 10 000 Oe at room temperature. (b) Hysteresis loops measured at a fine step size of 2 Oe per second, showing the coercivity of the alloys. (c) Growth of the magnetic domain structure in the 3Al-HEA and 7Al-HEA, imaged by Kerr-microscopy, under external magnetic fields. (d) Yield tensile strength-coercivity profiles of the investigated soft magnetic HEAs compared to those of other soft magnetic materials, such as NiFe, CoFe, SiFe, Fe, and established HEAs. (e) Plot of the temperature dependence of the saturation magnetization of the investigated HEAs.

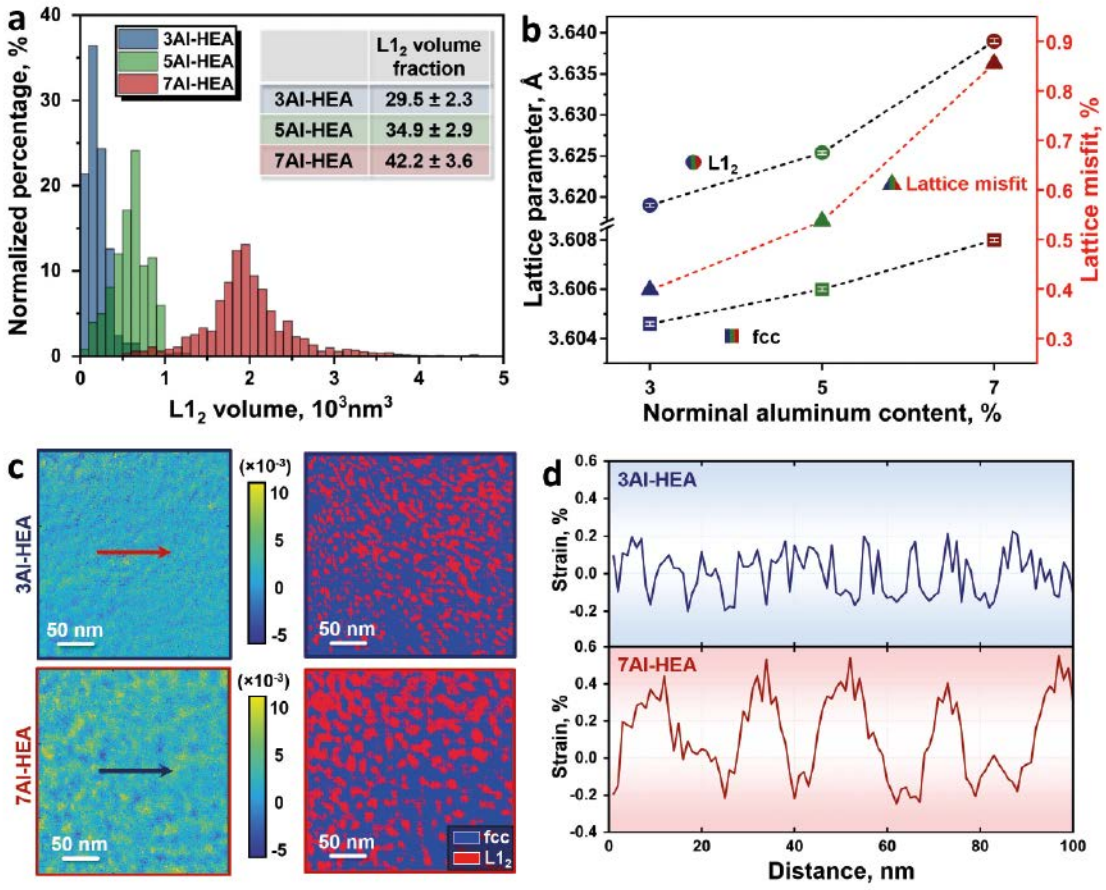

Fig. 4: Statistic volume distribution of the $L1_2$ nanoprecipitates and quantitative lattice misfit and lattice strain in the HEAs. (a) Normalized percentage with respect to the single precipitate volume, the inset shows the overall volume fractions of $L1_2$ precipitates. (b) Lattice parameter and lattice misfit of the $L1_2$ and fcc phases. The lattice misfit (ε) is calculated using the equation $\varepsilon = 2(\alpha_{L12} - \alpha_{fcc}) / (\alpha_{L12} + \alpha_{fcc})$, where α_{L12} and α_{fcc} are the lattice parameters of the $L1_2$ and fcc phases, respectively.[36] (c) Local strain distribution map and corresponding phase distribution map of the 3Al-HEA and 7A-HEA. (d) 1D strain distributions along the arrows in (c).

compositions of the FCC matrix and the $L1_2$ phases derived and averaged from several APT sub-volumes indicate that an increase in global Al content leads to repetitive enrichment of Fe and Al in the FCC matrix, while Ni, Ta, and Al are preferentially partitioned to the $L1_2$ phase. On the other hand, APT measurements reveal the absence of nano-segregation at near atomic-scale for B-HEA and randomised elemental distribution with an overall composition of $Fe_{34.7}Co_{30.2}Ni_{30.3}Ta_{4.8}$ (at%).

The representative tensile stress-strain curves of the investigated HEAs are shown in Figure 2a. B-HEA has a relatively low yield strength (σ_y=501 MPa) and high tensile elongation (TE=53.4%) as compared to 7Al-HEA (σ_y=1202 MPa, TE=15.3%). Moreover, 7Al-HEA shows a pronounced work-hardening behaviour during plastic straining. Figure 2b shows σ_{UTS}–TE profiles of several HEAs. Electron channelling contrast imaging (ECCI) and TEM were used to investigate the deformed microstructure and to understand the relevant deformation mechanisms at various local strain (ε_{loc}) levels. Figure 2c shows the evolution of deformation substructures developed in the HEAs during tensile straining. Microbands consisting of high dislocation densities are formed at the early deformation stage (ε_{loc}=5%) and significant dynamic microband refinement behaviour is observed with increasing Al content. For example, the mean distance between parallel microbands has reduced from 735±251 nm to 163±35 nm for 7Al-HEA when ε_{loc} increases from 30% to 50%. These results confirm dynamic microband refinement as the primary strain-hardening mechanism. Figure 2d shows the HRTEM image of a region at ε_{loc}=50%, where $L1_2$ nanoprecipitates have been sheared by a stacking fault (SF). Figure 2e schematically illustrates the strengthening mechanisms of such HEAs activated during deformation.

Vibrating sample magnetometry (VSM) was used to measure the HEAs' magnetic responses. Figures 3a and 3b show the Ms and Hc values from the magnetization curves. Increasing the (Fe+Co+Ni)-to-Al ratio linearly increases Ms values and slightly increases the Hc values from 3Al-HEA to 7Al-HEA (8.6 Oe to 10.7 Oe) indicating the investigated HEAs falling into the soft magnetic materials category. Figure 3c shows the magnetic domain structure growth in 3Al-HEA and 7Al-HEA under externally applied magnetic fields using magneto-optical Kerr-microscopy. The average magnetic domain width (W_{SD}) of 3Al-HEA and 7Al-HEA are found as

23.5±5.8 μm and 12.3±2.3 μm respectively, which are smaller than the average grain size of ~65 μm. Electrical Fe-Si steels with comparable W_{SD} show similar behaviour, which is attributed to the Al/Si enrichment within the matrix that changes the magnetic anisotropy constant of the matrix and domain wall energy, eventually leading to a variation in the domain size. The magnetic anisotropy is also impacted by the nanoscale chemical heterogeneity associated with nanoprecipitation and contributes to the refinement of magnetic domains and increased coercivity. The Bloch walls' movement under different applied magnetic fields is indicated by the yellow dashed area, which shows relatively smooth domain growth and confirms no notable magnetic pinning forces by coherent nanoscaled $L1_2$ precipitates on the domain walls' movement. Figure 3d shows σ_y versus Hc plot to establish a useful combination of HEAs' mechanical and magnetic properties. They demonstrate excellent σ_y and σ_{UTS} values and good Hc outperforming other SMMs. Figure 3e shows the temperature dependence of Ms up to 873K indicating good temperature resistance, which is further attributed to the high thermal stability of the $L1_2$ phase along with the Fe-Co-rich matrix.

Figure 4a shows the statistical volume distribution of the $L1_2$ precipitates in the Al-HEAs obtained from APT data sets. The average volume of nanoprecipitates increases from 168±27 nm^3 (3Al-HEA) to 2294±125 nm^3 (7Al-HEA). Figure 4b shows the XRD analysis indicating an increase in the volume fraction of the $L1_2$ precipitates and the corresponding lattice misfit with increasing global Al content. As lattice strain at the coherent interface can exert a pinning effect on the Bloch walls motion, thus 4D-STEM was used to measure lattice strain distribution between the $L1_2$ nanoprecipitates and the FCC matrix. Figure 4c shows the local strain map and the corresponding STEM phase map for both 3Al-HEA and 7Al-HEA, whereas Figure 4d illustrates 1D local strain distribution along the arrows marked in Figure 4c. The estimated average strain is found lower (-0.2% and 0.2%) for smaller precipitate sizes (3Al-HEA), but higher (-0.2% and 0.5%) for larger precipitates (7Al-HEA).

Overall, the studied HEAs contain ordered and coherent nanoprecipitates exhibiting ultra-high σ_y (952 MPa for 3Al-HEA, 1202 MPa for 7Al-HEA), σ_{UTS} (1325 MPa for 3Al-HEA, 1526 MPa for 7Al-HEA) and good TE values (15% for 7Al-HEA, 29% for 3Al-HEA). Particularly, 7Al-HEA shows a significant increase in σ_y by 245% as compared to B-HEA. This considerable improvement in mechanical properties comes from three different strengthening mechanisms. The first mechanism is the massive solid solution strengthening, which arises from the high concentrations of the multiple elements (Fe=32%, Ni=28%, Co=28%, Al=7%, and Ta=5% for 7Al-HEA) in the FCC matrix. This adjusts the SF energy into a regime where dislocation glide becomes planar. Precipitation strengthening by a high volume fraction of the ordered $L1_2$ nanoprecipitates and large-sized precipitates is the second mechanism. Dynamic microband refinement is the third mechanism leading to high strain hardening rates and high uniform deformation. Besides this, the large lattice parameter of $L1_2$ nanoprecipitates leads to a positive lattice misfit beneficial for the high-temperature mechanical properties.

The HEAs retain a good soft magnetic behaviour with high Ms (105 $Am^2\ kg^{-1}$ for 3Al-HEA, 88 $Am^2\ kg^{-1}$ for 7Al-HEA) and low Hc (8.6 Oe for 3Al-HEA, 10.7 Oe for 7Al-HEA) values at room temperature. The first mechanism explaining this behaviour is the addition of non-ferromagnetic elements Ta and Al, which reduces the total magnetization per formula unit and leads to a slightly lower Ms (88 at% for 7Al-HEA and 92 at% for 3Al-HEA). The second mechanism is the coercivity of SMMs controlled by the displacement of magnetic domain walls, which are strongly affected by the grain/twin boundaries and incoherent phase interfaces. As the average grain size of HEAs and conventional SMMs are comparable, thus it is believed that the HEA grain boundaries do not act as a deteriorating factor for the relatively low Hc (<11 Oe) required for the soft magnetic applications. The slightly increased Hc observed for the Al-HEAs (Figure 3b) is mainly associated with the increasing volume fraction of the $L1_2$ phase (Figure 4a) and the corresponding lattice misfit (Figure 4b). Moreover, the pinning effect on the Bloch walls movement exerted by the precipitates is insignificant compared to that from high-angle and twin boundaries as revealed by the *in situ* observations of the domain wall movement (Figure 3c).

Summary

Introducing homogeneously distributed coherent and ordered nanoprecipitates into a non-equiatomic FeCoNiTaAl HEA system, a good balance of strength, ductility and soft magnetic response can be tailored. These nanoprecipitates are formed due to the strong interaction among Al-Ta and Al-Ni respectively, which promotes the formation of intermetallic phases with solid solution variation on the sub-lattices. A good combination of strength and ductility is derived from massive solid solution, nanoprecipitation and dynamic microband strengthening. The full coherency of the ordered nanoprecipitates and the matrix contributes significantly to the strength with only a slight increase in coercivity. This alloy design concept shows the development of a novel soft magnetic material with improved mechanical properties as required for the electrification of industry and transportation.

Digest of
Han L, Rao Z, Filho IRS, Maccari F, Wei Y, Wu G, et al.; Ultrastrong and Ductile Soft Magnetic High-Entropy Alloys via Coherent Ordered Nanoprecipitates; Advanced Materials 2021, 33, 2102139. © 2021 The Authors. Advanced Materials published by Wiley-VCH GmbH.
https://doi.org/10.1002/adma.202102139

The Role of Microstructural Constituents on Strength–Ductility–Local Formability of a Transformation-induced-plasticity-aided Bainitic Steel

Tang S, Huifang L, Jianping Li H, Liu Z, Wang G

Introduction

High-strength steels are often used to reduce car body weight but lack adequate local formability, such as stretch flangeability and bendability. Local formability is typically quantified as the hardness ratio between soft and hard phases, which leads to localized strain affecting the micro-void formation and crack propagation. The hole-expansion ratio (HER), a characterization of stretch flangeability, depends on the strength of the matrix and the contrast in hardness between soft and hard phases. For example, a high ferrite/bainite hardness ratio leads to better hole-expansion performance, resisting void nucleation, and crack propagation. As a result, the transformation-induced-plasticity (TRIP)-aided bainitic steels having uniform microstructure shows homogenous strain distribution, and therefore a high local ductility, before failure as compared to the multiphase steels. In literature, both tensile strength (TS) and total elongation (TEL) have been considered to predict the local formability. HER has been reported to be closely related to TS within the range of 300–700 MPa, beyond which it has been influenced by several factors such as yield strength (YS), TS, coefficient of normal anisotropy, TEL, post-uniform elongation (PEL) and reduction in area. To have a clear understanding of the local formability of the TRIP-aided bainitic steels, the austenitizing temperature was varied to produce three different microstructures with different ratios of ferrite and bainite. The microstructure, uniaxial tensile properties, stretch flangeability, and bendability was investigated and evaluated.

Experimental details

The steels with relatively high Si (1.4%) and Nb (0.045%) were prepared as 150 kg ingots in a vacuum induction furnace. The ingots were hot forged into blocks and austenitized at 1200°C for 2h. A multi-pass hot rolling at 900°C followed by air cooling was used to convert the blocks initially into the 4.5 mm plate thickness and then they were further cold-rolled to 1.2 mm plate thickness with a total of 73.3% rolling reduction. This cold-rolled plate was machined to small specimens to understand the effect of the austenitizing temperature via 2-step continuous annealing experiments as detailed in Figure 1. The microstructure was investigated through EBSD and XRD analyses, whereas the mechanical properties were quantified via tensile test, hole-expansion experiment, and 3-point bend test. The average TS, TEL, HER, and bending ratio (BR) were calculated from these experiments and correlated with the microstructural changes.

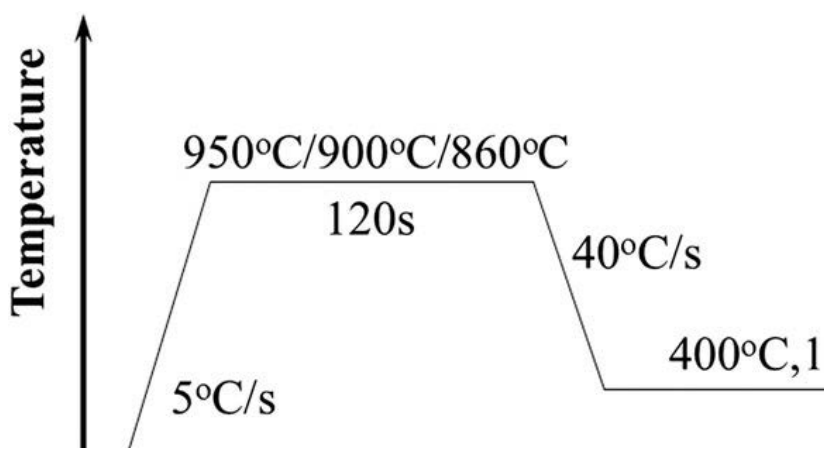

Fig. 1: Schematic diagrams for continuous annealing experiments.

Microstructure and retained austenite (RA) characterization

Figure 2 shows the optical micrographs of the austempered samples. At 860°C, a large quantity of pro-eutectoid ferrite (PF, light brown) and blocky martensite/austenite (M/A) islands (shown with white arrows), located between PF and bainite colonies, are observed (Figure 2a). The PF and blocky M/A islands are retained till 900°C, but with reduced quantity and refined size. Simultaneously, the volume fraction of the lath bainitic microstructure is increased (Figure 2b). At 950°C, the PF finally disappears and the microstructure becomes dominantly lath bainite with a low quantity of tiny blocky M/A constituents in the matrix (Figure 2c). At lower austenitizing temperature, the PF formation is favoured through prior austenite grain size (PAGS) refinement, and accordingly, the bainite transformation kinetics is decreased. As a result, the untransformed austenite may transform to martensite with a part of austenite retained at room temperature. Figure 3 shows the image quality map with retained austenite (RA) distribution as measured by EBSD. RA shows

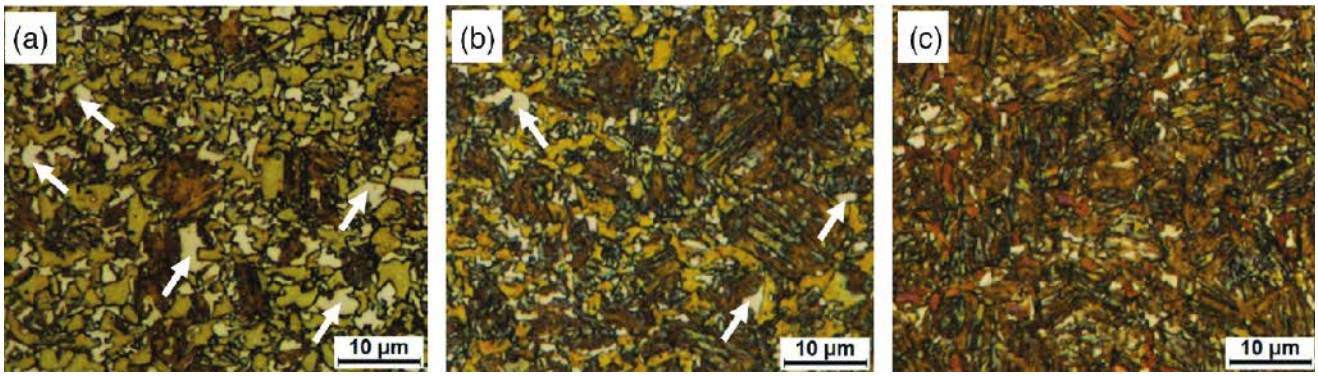

Fig.2: Optimal micrographs for specimens austempered at 400°C under different austenitizing temperatures (a) 860°C, (b) 900°C, and (c) 950°C.

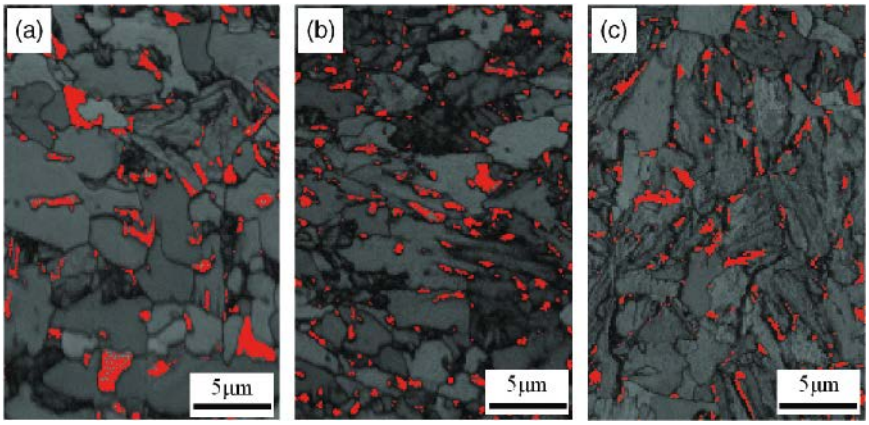

Fig.3: Image quality map with retained austenite distribution measured by EBSD under different austenitizing temperatures: (a) 860°C, (b) 900°C, and (c) 950°C.

mostly blocky morphology at 860°C, which is changed to rod-like formation at 900°C and the quantity is reduced simultaneously up to 950°C. Both Figures 2 and 3 indicate that the origin of the blocky RA is the M/A islands, which are influenced by the carbon enrichment contributed by the PF transformation and the incomplete bainitic transformation. The rod-like RA is located mainly inside the bainitic colonies.

Figure 4 shows the volume fraction of RA (Vγ) and its carbon concentration (Cγ) for different austenitizing temperatures as measured by XRD. With an increase in the austenitizing temperature, Vγ is decreased due to the carbon rejection from PF to austenite and the higher thermal stability of austenite for refined PAGS. As the austenitiz-

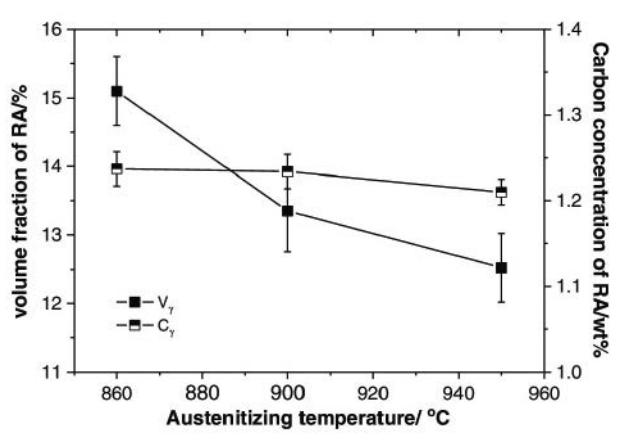

Fig.4: Volume fraction and carbon concentration of retained austenite for different annealing temperatures.

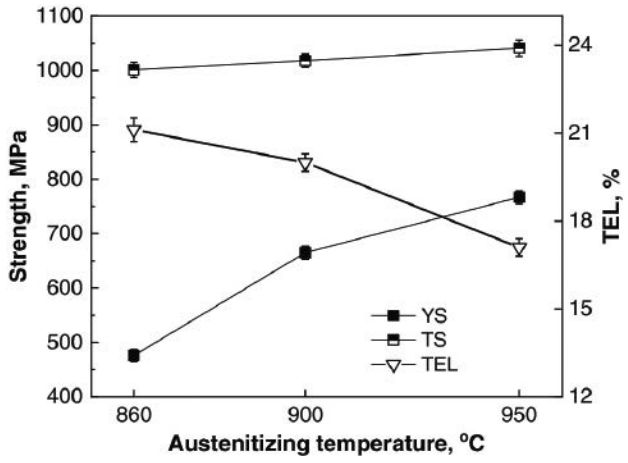

Fig.5: Relationship between austenitizing temperature and strength-ductility.

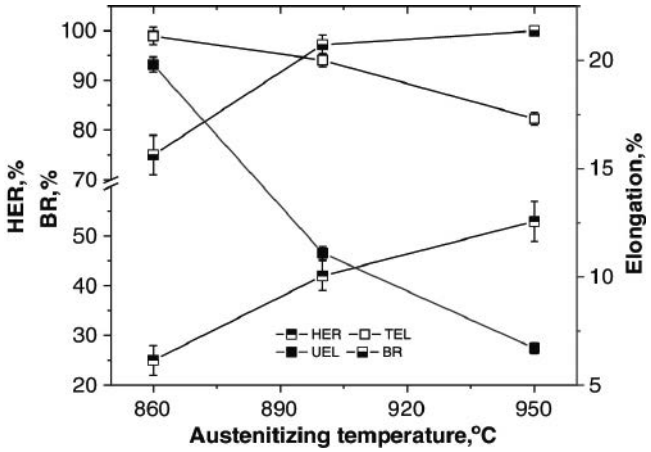

Fig.6: HER, BR, and elongation for different austenitizing temperature.

ing temperature reaches 950°C, the carbon concentration of RA is slightly decreased. The bainitic ferrite shows a lath morphology, which is useful to entrap a part of solute carbon atoms into the high-density dislocation areas. As a result, the surrounded RA is enriched with less amount of carbon.

Tensile properties, stretch flangeability, and bendability

Figure 5 shows the effect of austenitizing temperature on mechanical properties such as YS, TS, and TEL%. With an increase in austenitizing temperature from 860°C to 950°C, sharp and slight increases are observed for YS and TS respectively, but a noticeable decrease is found for TEL%. The true stress-strain curves indicate a uniform strain increase and gradual decrease of the strain hardening rate with the decrease in the austenitizing temperature. Figure 6 shows the increase of both HER and BR and the decrease of both UEL and TEL with the increase in the austenitizing temperatures. Higher HER and BR lead to higher PEL, which delays the final fracture after the onset of necking representing the exact failure caused by these two local forming processes. For similar strength steel grades, a linear relationship is observed between the local formability and HER, where a single-phase microstructure corresponds to a higher HER, and therefore higher PEL, compared to a multiphase microstructure (such as DP steel, ferrite–bainite steel, and TRIP steel). When the difference between the ferrite and the hard phase is large, both HER and PEL are reduced. A good bendability depends on both strength-elongation balances as well as microstructural homogeneity. Typically, YS and TS are determined by the hardness of the soft and hard phases respectively, and thus, YR is calculated to represent the hardness ratio of soft/hard phases. Figure 7 shows a linear relationship between YR and both HER, BR, and their balance with TS under different austenitizing temperatures. So, PEL plays a consistent role with YR in determining both HER and BR by replacing the multiphase microstructures (observed at austenitizing temperatures of 860°C and 900°C) with the uniform bainitic microstructure (formed at 950°C austenitizing temperature).

Figure 8 shows the cross-sectional SEM images close to the main crack after hole-expansion and bending tests during 860°C and 900°C austenitizing temperatures. Severely deformed ferrite and large-sized voids at the vicinity of ferrite/martensite interfaces are observed at 860°C (Figure 8a, c). The dominant cracking mechanism during hole expansion is the strain incompatibility between the soft and hard phases. A lower ferrite/martensite hardness ratio leads to a higher degree of strain partitioning to the softer ferrite phase and therefore potentially induces more damage to the matrix close to the hard phase resulting in nucleation and growth of the voids in these regions. On the other hand, Figure 8b, d shows tiny cracks among the fine bainite laths with film-like M/RA (some RA may transform to martensite due to the TRIP effect during hole expansion). These film-like RA may be able to inhibit the crack propagation, however, the large blocky RA may deteriorate the microstructure uniformity while transforming into the martensite during initial local deformation. This leads to the lower HER and BR by

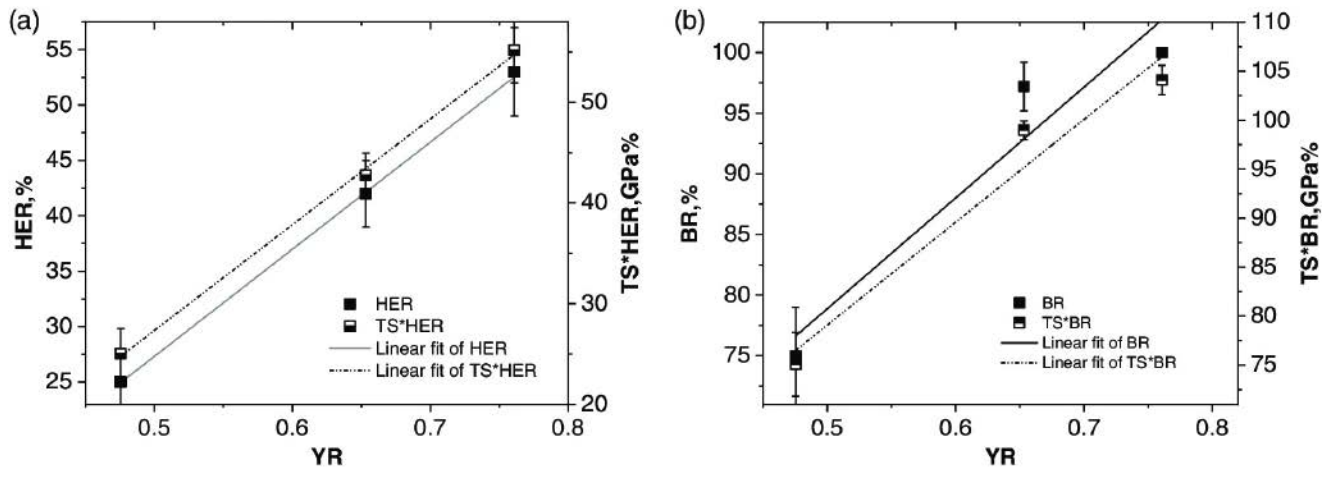

*Fig.7: HER, BR, TS*HER, and TS*BR versus YR.*

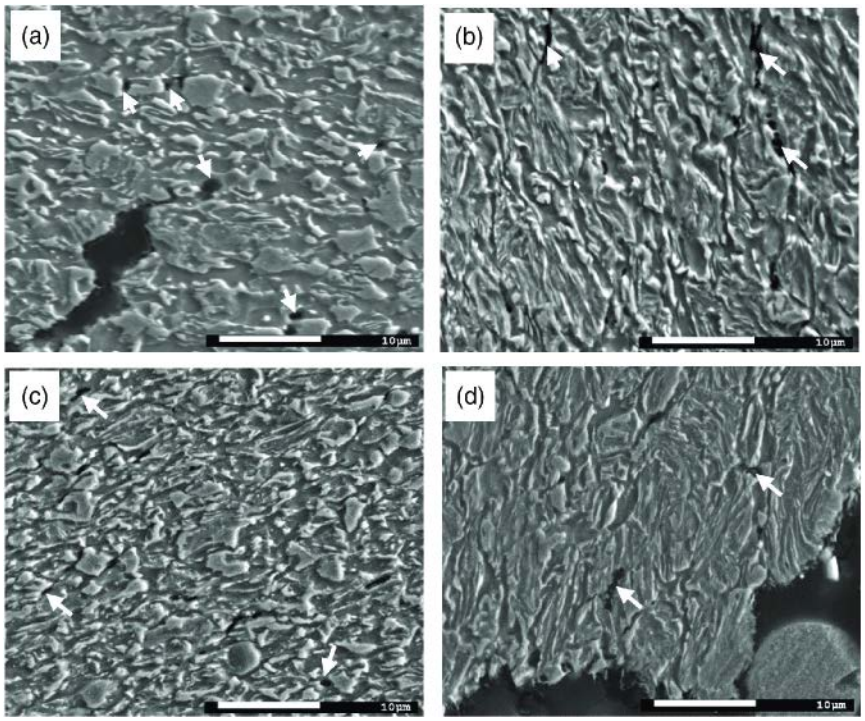

Fig.8: *SEM morphology of cross-sectional area near the main crack after hole expansion: (a) 860°C austenitizing, (b) 950°C austenitizing and bending, (c) 860°C austenitizing and (d) 950°C austenitizing.*

early failure at the vicinity of ferrite/martensite interfaces through a void or crack formation. The volume fraction and the stability of RA might influence the HER, BR, or fracture behaviour, however that could not be quantitatively derived from this study.

Summary

The effect of the microstructural constituents on the microstructural and mechanical properties of the TRIP-aided bainitic steel and its local formability was investigated. With a decrease in austenitizing temperature, the PF was formed due to the refinement of PAGS and large blocky M/A constituents appeared. With an increase in the austenitizing temperature, the blocky RA was significantly reduced with a change in morphology from blocky to rod-like and thus it was considered as blocky RA originated from the M/A islands. The rod-like RA was located mainly inside the bainitic colonies as its formation was attributed to the carbon enrichment contributed by the PF transformation and the incomplete bainitic transformation. The blocky RA further contributed to the higher strain hardening rate during initial deformation and gradual decrease of the strain hardening rate resulting in the higher UEL but lower PEL with a decrease in the austenitizing temperature. Both HER and BR showed a linear relationship with PEL, but an opposite trend to both UEL and TEL with a change in the austenitizing temperature. Simultaneously, both HER, BR and their balance with TS maintained a linear relationship with YR. PEL played a consistent role with YR in increasing the balance of strength and local formability and thereby replacing the multiphase microstructure with uniform bainitic microstructure.

Digest of
Tang S, Huifang L, Jianping Li H, Liu Z, Wang G; The Role of Microstructural Constituents on Strength–Ductility–Local Formability of a Transformation-Induced-Plasticity-Aided Bainitic Steel; Steel Research 2021, 92, 2000474. ©2020 WILEY-VCH GmbH.
https://onlinelibrary.wiley.com/doi/10.1002/srin.202000474

Enhancing Ductility and Fatigue Strength of Additively Manufactured Metallic Materials by Preheating the Build Platform

Nezhadfar PD, Shamsaei N, Phan N

Introduction

The static strength of additive manufactured (AM) materials is typically higher than the wrought counterparts due to the finer microstructure resulting from the high solidification rate. However, it can also lead to the formation of volumetric defects (such as gas-entrapped pores and lack of fusion), residual stresses and heterogeneous anisotropic microstructures, which are detrimental to the fatigue resistance of the material. One of the main challenges for the adoption of AM technology by several key industries is to qualify AM materials for load-bearing applications prone to cyclic loading. For example, the presence of the volumetric defects formed during the AM processes deteriorates the fatigue performance of several materials such as Inconel 718, Ti-6Al-4V and SS as compared to their wrought counterparts. The thermal history, particularly the solidification rate, temperature gradient and consequently the cooling rate, associated with any AM part deeply influences the formation of volumetric defects, and therefore final microstructure. For example, a more homogenized microstructure with fewer volumetric defects is produced when the part is large or the interlayer time interval is short, or when the process parameters (such as laser power, scan speed and scan strategy) are optimised. Altering the thermal history also extends to the pre-heating of the build platform, which has been found effective in varying the microstructures of both electron beam powder bed fused (EB-PBF) Inconel 718 and laser beam powder bed fused (LB-PBF) Al-Mg(-Sc)-Zr samples. The effect of preheating the build platform on the residual stresses and final microstructure has been researched to some extent, however the same on the fatigue performance of the AM parts has not yet been studied. Therefore, this work aims to evaluate the effect of build platform preheating on both the microstructural and mechanical properties of LB-PBF-processed 316 SS due to its higher ductility and lower sensitivity to volumetric defects under cyclic loading.

Experimental details

The Renishaw AM 250 additive system was used to fabricate the specimens from the austenitic 316L SS powder (17.7Cr-0.02C-12.6Ni-0.87Mn-0.67Si-2.29Mo) using an LB-PBF method. One set of specimens was fabricated without preheating the build platform, i.e. non-preheated (NP), whereas the build platform was preheated to a maximum of 150°C (P150) for fabricating the second set to study the effect of build platform preheating on the microstructural and mechanical properties of the material. The same process parameters (200 W laser power, 0.11 mm hatching distance, 1833.3 $mm.s^{-1}$ scan speed and 0.05 mm layer thickness), except the preheating temperature, were used to fabricate all the parts without application of any heat-treatment. The round fatigue and tensile test samples were produced following ASEM E606 and ASTM E8 respectively. The effect of preheating the build platform on the microstructural features, including the melt pool, defect size and population, and grain structure, was studied in the gauge section of the fabricated specimens via X-ray CT scans and EBSD. The quasi-static tensile and uniaxial fully reversed, strain-controlled fatigue tests were repeated twice with extensometers for both NP and P150 test conditions. The fractography analysis was performed on the fracture surfaces using the SEM to understand the fatigue failure mechanisms.

Microstructure characterization

Figure 1 shows the melt pool analysis for NP and P150 samples on their longitudinal plane parallel to the build direction (YZ plane). NP condition shows a shallow melt pool (~90 µm) as compared to the P150 condition (~150 µm). The melt pool depth (d_p), overlap depth (d_o), and layer thickness (t_l) altogether influence the formation of volumetric defects. The d_p/t_l and d_o/t_l ratios calculated for NP condition (1.8 and 1.3 respectively) are found less than the P150 condition (3 and 1.85 respectively), which are attributed to the effect of preheating the build platform. The higher temperature of the previously fused layers during fabrication of a new layer leads to deeper melt pools in P150 condition. The lower temperature difference between the previously solidified layers and the newly fabricated layer can result in a lower solidification rate, fewer pores and lack of fusion (LoF) defects, and sufficient overlap depth. During simulation, a 14% reduction in the solidification rate is observed for the P150 condition as compared to the NP condition. Moreover, P150 condition decreases the size and population of the defects throughout the gauge section as compared to NP condition. Particularly, fewer and smaller defects are observed in the bottom (~25 µm far from the build platform) and middle of the gauge section as compared with the top part (~40–45 mm far from the build platform).

Figure 2A and B show both the visual and statistical evaluation of volumetric defects via X-ray CT scan in the middle of the gauge section for NP and P150 specimens. NP condition contains more and larger volumetric defects as compared to the P150 condition and some examples of LoF defects and gas-entrapped pores are highlighted by red and green colours respectively. The probability of formation of LoF defects is reduced significantly when d_o/t_l ratio becomes close to 2. For NP conditions, the d_o/t_l ratio is larger than 1 but not close to 2, which increases the chance for the formation of gas-entrapped pores and LoF defects (Figure 2A). The d_o/t_l ratio is found to be 1.85 (i.e. close to 2) for P150 condition, thus smaller and

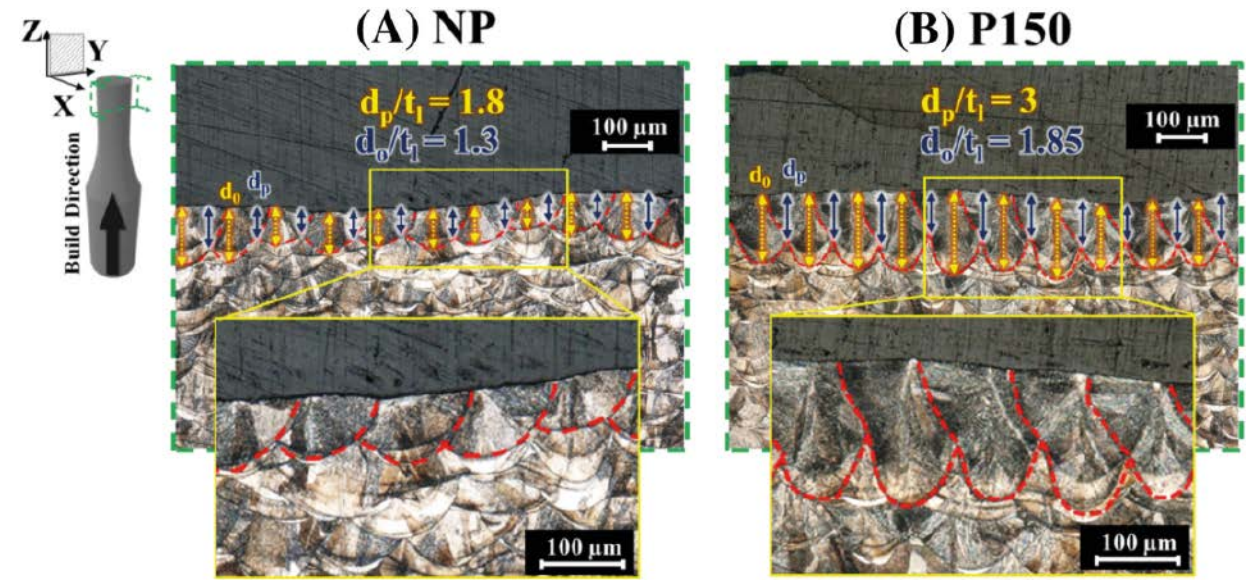

Fig. 1: Melt pool characterization following the method proposed by NASA for (A) non-preheated (NP) and (B) preheated to 150°C (P150) conditions

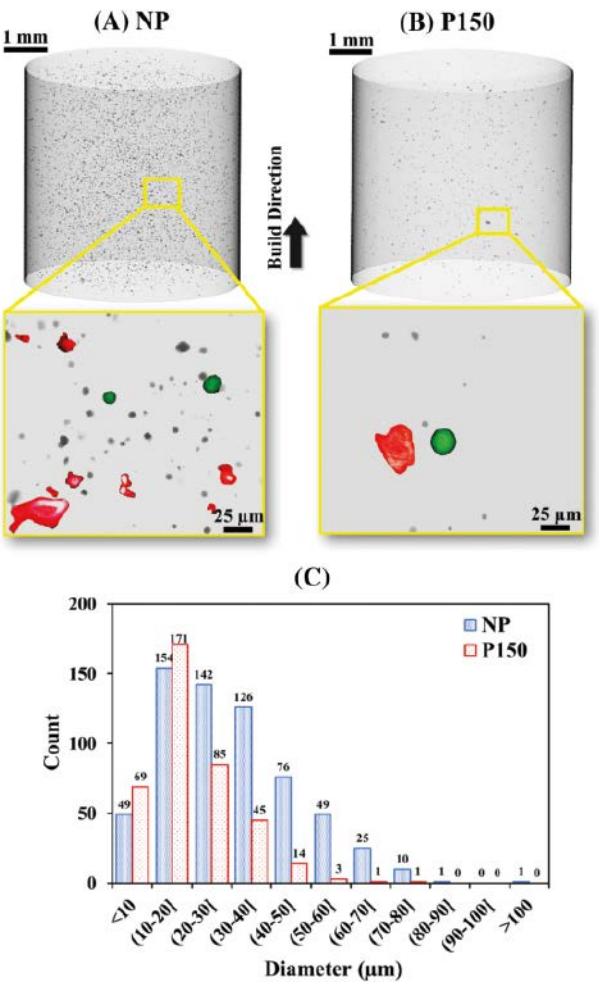

Fig. 2: X-ray CT scan results from a small section (~5mm) of the gage section of machined laser beam powder bed fused (LB-PBF) 316L stainless steel (SS) specimens for (A) non-preheated (NP) and (B) preheated to 150°C (P150) conditions, as well as (C) defects size distributions based on 100 radial cross-sections

fewer gas-entrapped pores and LoF defects are formed (Figure 2B). The diameter of the defects are statistically represented in Figure 2C, but without showing the entire pore size distribution.

The inverse pole figure (IPF) maps of the LB-PBF 316L SS in NP and P150 conditions are presented in Figure 3, where elongated grains along the heat dissipation path towards the build platform are observed. The IPF of NP condition shows the austenite γ grains mostly oriented at <001> direction (Figure 3A), which is a typical solidification growth direction for FCC and BCC structures with the presence of epitaxial grains. The crystallographic orientation of the γ grains is changed from <001> to <110> and <111> directions for P150 direction (Figure 3B), which is mostly associated with the lower thermal gradient and the solidification rate. For the same reason, an equiaxed and finer cellular structure is observed for P150 sample as compared to NP sample. The formation of the sub-grains is particularly observed in the P150 condition, however, the sub-grains can not be turned into the grains with high angle boundaries and leads to grain refinement due to insufficient preheating temperature to provide an adequate driving force for recrystallization.

Quasi-static tensile behaviour

The quasi-static tensile stress-strain curves of NP and P150 conditions indicate ~18%

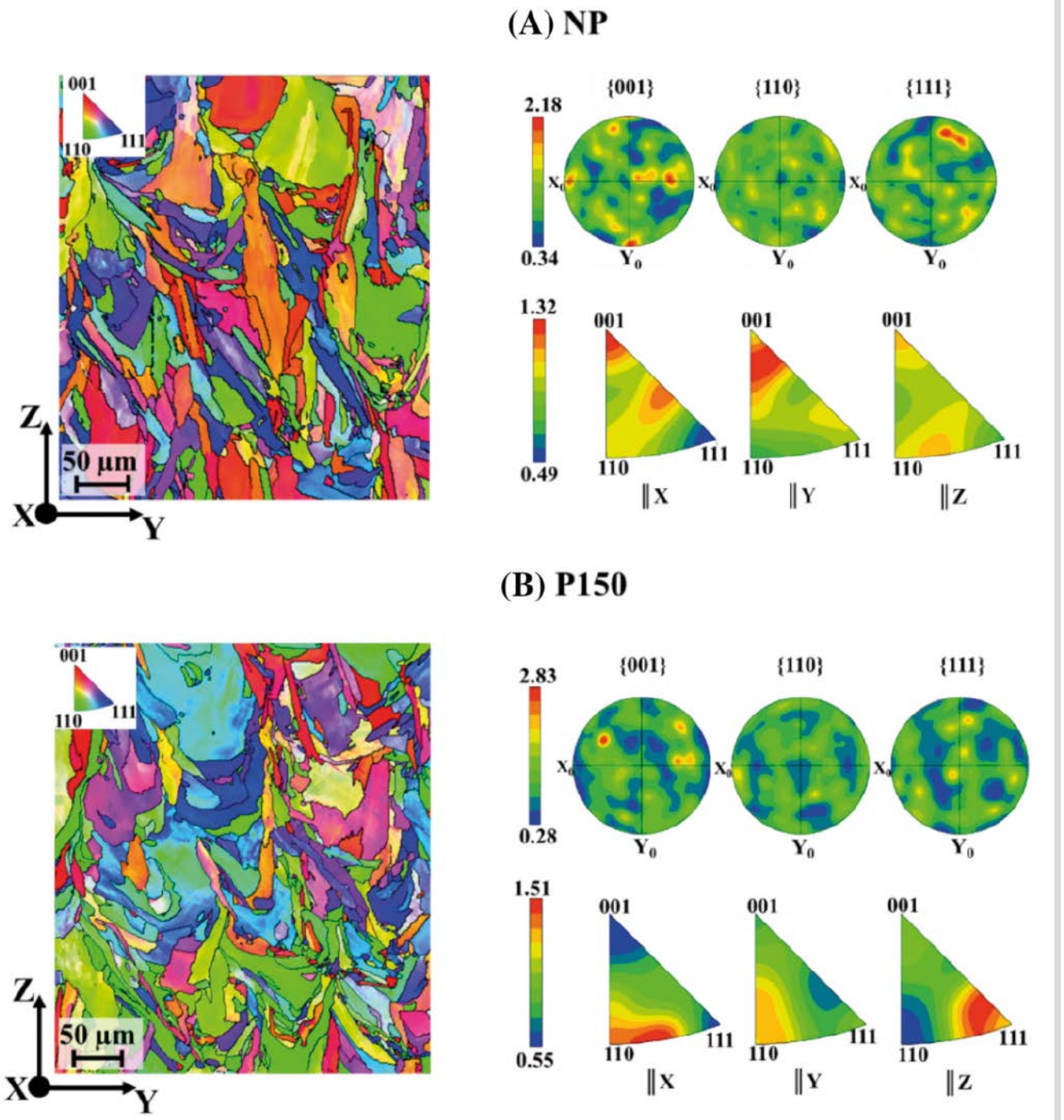

Fig. 3: Microstructure and crystallographic characterization on the longitudinal plane; inverse pole figure (IPF) maps along the z-axis as well as pole figures and IPFs for (A) non-preheated (NP) and (B) preheated to 150°C (P150) specimens

increase in the ductility of the P150 specimen without jeopardizing the material strength. This increase in ductility for the P150 specimen is most likely to be associated with the lower volumetric defects and orientation of the grains along the FCC preferred slip system (<110>-/<111>-oriented grains), which helps the dislocations to slip and glide easily. Figure 4 shows the tensile fracture surfaces for both NP and P150 samples, where a higher level of volumetric defects is observed on the fracture surface of NP specimens (Figure 4A) as compared to their P150 counterparts (Figure 4B). Large LoF defects are characterized on the fracture surface of the NP specimen containing un-melted powder particles and they are believed to be contributing to the lower ductility. On the other hand, preheating the build platform reduces such defects and assists with the increase in the ductility under quasi-static tensile loading for the P150 specimen.

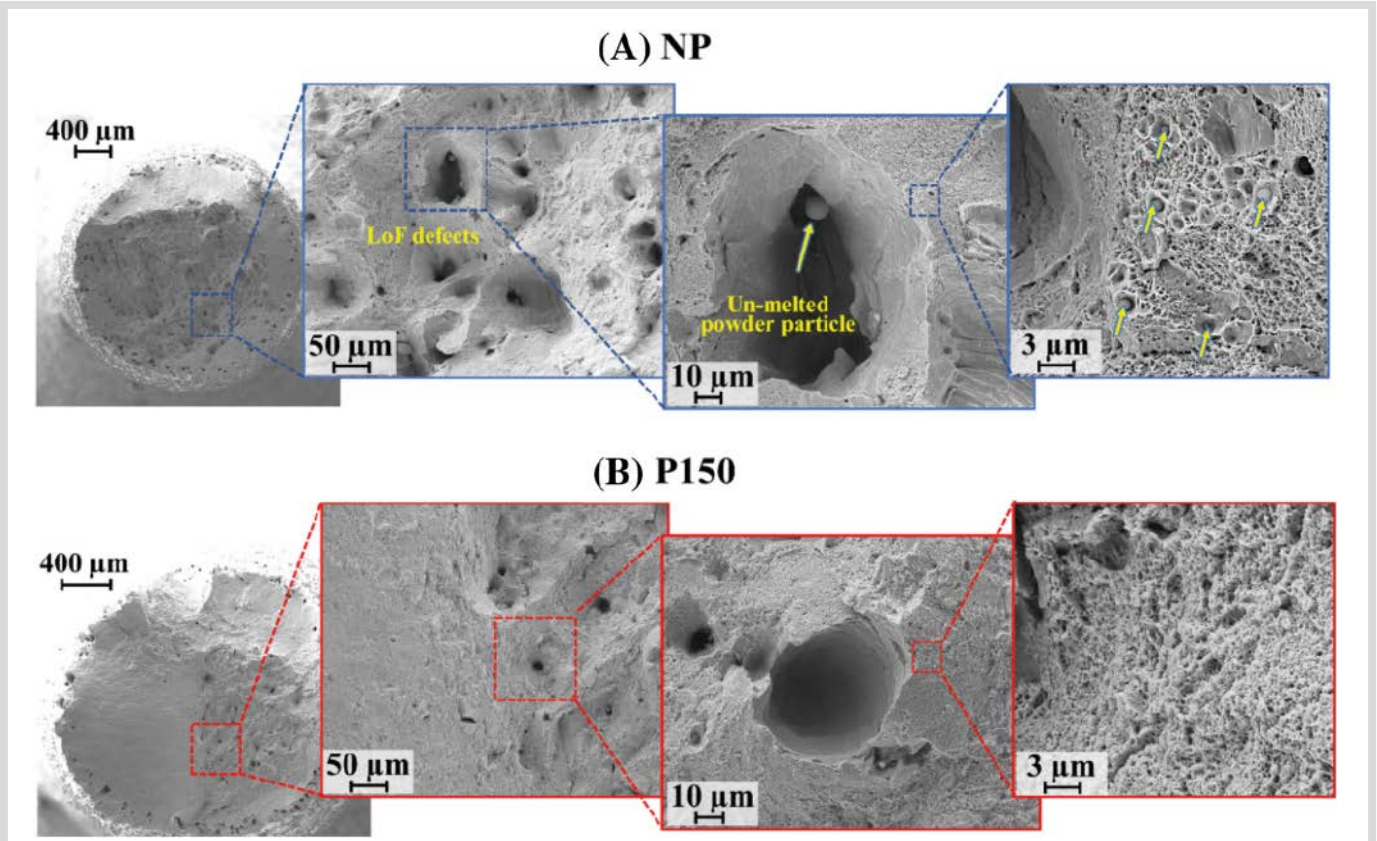

Fig. 4: Tensile fracture surfaces of laser beam powder bed fused (LB-PBF) 316L stainless steel (SS) specimens fabricated in (A) non-preheated (NP) and (B) preheated to 150°C (P150) conditions. The unmelted powder particles found in the lack of fusion (LoF) defects are shown by yellow arrows

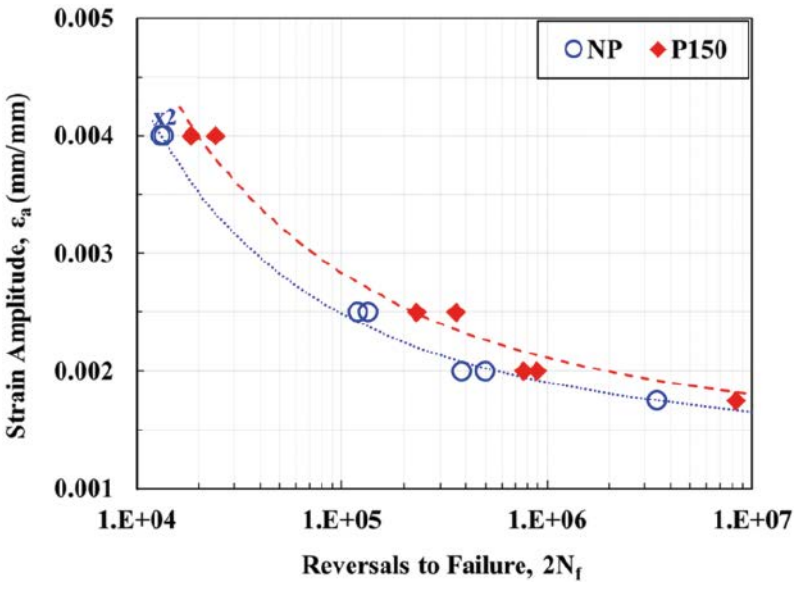

Fig. 5: Strain-life fatigue data and fits for machined laser beam powder bed-fused (LB-PBF) 316L stainless steel (SS) specimens fabricated in non-preheated (NP) and preheated to 150°C (P150) conditions

Fatigue behaviour

Figure 5 shows no significant effect of pre-heating the build platform on the cyclic deformation of NP and P150 specimens, as they exhibit similar cyclic deformation behaviours, initial cyclic hardening followed by cyclic softening. The stable stress-strain hysteresis loops are found identical for both conditions. Still, some improvement in the fatigue performance across all life regimes is noticed for the P150 condition, which is most likely due to the lower volumetric defects, specifically LoFs as compared to the NP counterparts. Moreover, the fracture surfaces of both NP and P150 specimens tested at 0.0020 $mm.mm^{-1}$ of strain amplitude show several cracks initiated from LoF defects. The crack initiating defect size is calculated from Murakami's $\sqrt{area}$ approach and the number of cracks started from LoF defects close to the surface are found as four and one for NP and P150 conditions respectively. The $\sqrt{area}$ values of 144, 83, 71, and 24 µm respectively are found for NP condition as compared to 68 µm for

P150 condition indicating a reduction of volumetric defects and enhancement of the fatigue performance due to preheating of the build platform. When the strain amplitude is reduced to 0.00175 $mm.mm^{-1}$, then the fatigue life of the P150 specimen is found 2.5 times longer than the NP specimen. However, it should be noted that the fatigue performance of the 300 SS series is not very sensitive to defects, but the effects are typically alleviated by the microstructure and ductility.

Summary

The effect of preheating the build platform on the microstructural and mechanical properties of LB-PBF 316L SS was investigated under both NP and P150 test conditions. P150 condition lowered the solidification rates resulting in deeper melt pools as compared to the NP condition due to the reduced temperature gradient between the melt pool and the bulk solidified material. P150 condition changed the crystallographic orientation of grains from <100> to <110> and <111> and developed finer and more equiaxed cellular structures as compared to the NP condition, which contained more needle-like dendritic cellular structure. Subgrains were formed in the P150 microstructure, however insufficient preheating could not lead to full recrystallization. P150 condition also led to fewer and smaller volumetric defects due to higher melt pool and overlap depths. The fewer volumetric defects and fine cellular structure increased the elongation to failure under quasi-static tensile loading ~18% and improved the fatigue resistance for P150 condition compared with the NP counterpart.

Digest of
Nezhadfar PD, Shamsaei N, Phan N; Enhancing ductility and fatigue strength of additively manufactured metallic materials by preheating the build platform; Fatigue & Fracture of Engineering Materials & Structures 2021;44, 13372. © 2020 John Wiley & Sons Ltd.
https://onlinelibrary.wiley.com/doi/10.1111/ffe.13372

Multiscale Additive Manufacturing of Metal Microstructures

Ercolano G, Zambellii T, van Nisselroy C, et al.

Additive micro-manufacturing of metal objects

The additive micro-manufacturing of metal objects can be produced either in a one-step or two-step procedure. An advantageous one-step approach is local electrochemical (EC) reduction of metallic ions, which offers fully dense, conductive and mostly contaminant-free metal features without pre or post-processing operations. EC 3D printing methods involve confinement of the EC reaction in a small volume either by using a droplet cell configuration or by local delivery of precursor species in liquid. The first approach requires a glass pipette filled with the metal ion solution and equipped with a counter electrode (CE), whereas the second approach involves a double-barrel pipette or a FluidFM probe that is used for local dispensing of metal ions in a liquid. Particularly in FluidFM probe, a micro-channelled atomic force microscope (AFM) cantilever containing metal ion solution progresses to the working electrode (WE) of a standard three-electrode cell using the cantilever deflection as a feedback signal. This signal is further used to detect the plating completion, as the voxel that reaches completion underneath the aperture pushes against the probe apex, causing a deflection of the AFM cantilever. This makes the printing method fully automated, accomplishing a true layer-by-layer process. The recent developments in EC printing include: (i) use of platinum for electroplating instead of copper (Cu) and (ii) enlargement of the printing area combined with a feedback control via meniscus-confined protocol, however, they do not address the industrial requirements for high volumetric throughput. This can be obtained by either increasing the voxel area or minimizing the effects on the spatial resolution by controlling the individual size of each voxel. To increase the printing throughput, a novel printing set-up has been designed where the voxel size has been adjusted by varying the nozzle aperture and the applied pressure.

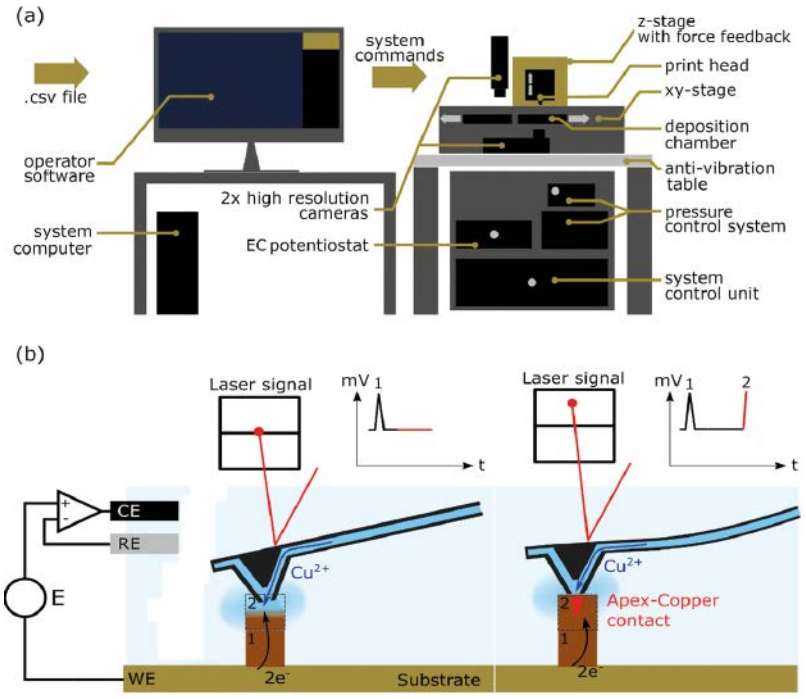

Fig. 1: (a) Schematic of the additive micromanufacturing system. On the left, a system computer sends commands to the system control unit on the right. On the right, the system control unit governs the printing process using an embedded controller. The FluidFM probe sits on the printing head and is moved in the EC deposition chamber by the z-stage. A microfluidics control system regulates the electrolyte flow through the cantilever aperture. (b) Schematic representation of the printing process: Cu^{2+} ions are locally injected in the EC cell through the cantilever aperture in close proximity (Δz = 500 nm) of a growing structure (WE), these ions are electrochemically reduced to Cu^0 on the metal surface forming the printed voxel. When the reduction front reaches the cantilever, the latter is deflected (optical beam deflection), automatically triggering the positioning to the next location. WE, CE, and RE indicate the working electrode, counter electrode, and reference electrode, respectively.

Design of a novel micro-manufacturing setup

The novel micro-printing setup has been designed to maintain complete automation and coordination of the probe positioning system with the liquid flow, applied substrate potentials, and AFM deflection signal to detect the voxel growth. The limitations include restriction in printed feature height (15 µm) and instrumentation synchronization delay leading to slower printing rates. Figure 1a shows a redesign of the micro-printing setup from both the hardware and software perspectives and Figure 1b shows the schematic representation of the

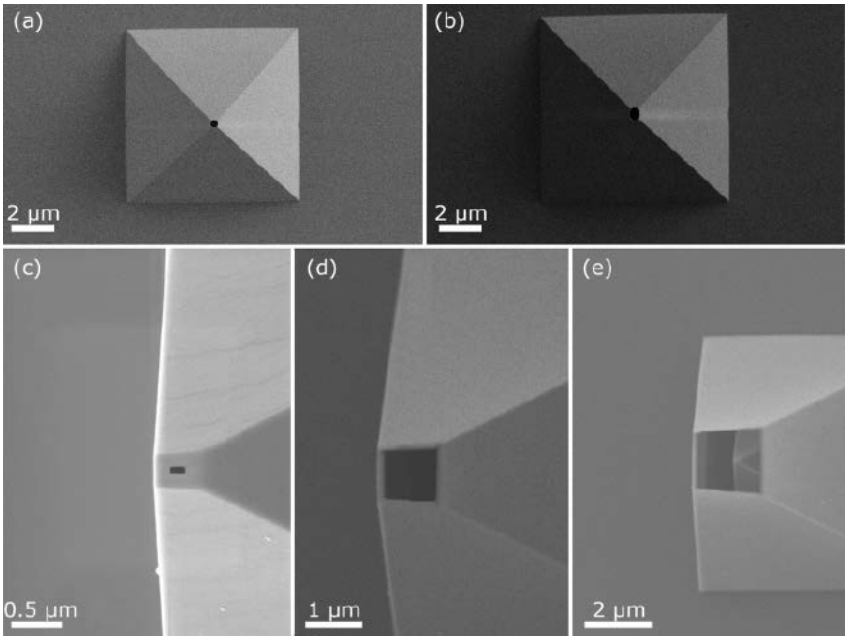

Fig. 2: Scanning electron microscopy (SEM) images of the different tip apertures. Top view of a (a) 300 nm and (b) 500 nm diameter aperture, obtained by contact lithography. Top view of a (c) 100 nm, a (d) 1 µm, and a (e) 2 µm side-square aperture, obtained by FIB milling of closed pyramidal probes.

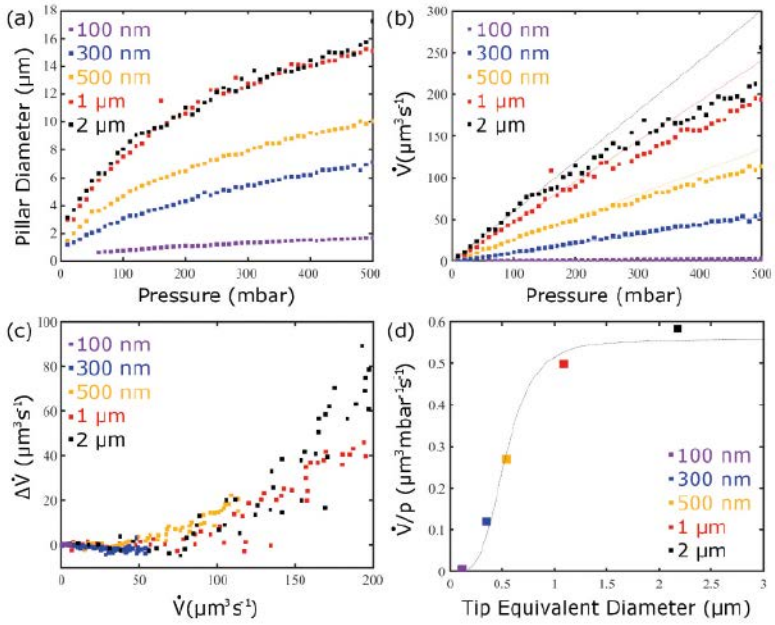

Fig. 3: (a) Pillar diameter obtained as function of the pressure applied during printing. (b) Volumetric deposition speed as function of the pressure. (c) Difference between the experimental volumetric deposition speed and the corresponding linear fit (see (b)) versus the volumetric deposition speed. (d) Volumetric deposition speed normalized by the pressure for the different tip equivalent diameters $D_e \equiv 2\sqrt{A/\pi}$.

printing process. Some important features of this solid Teflon-made set-up include: (i) fast feedback loop with very low latency, where controller responds within 1 ms by retracting the tip from the voxel surface and moving to the next point when deflection threshold exceeds due to the voxel touching the tip, (ii) stable and long-term operation, in which continuous printing can be done up to tens of hours without any delay regarding lack of voxel coordinate information, (iii) introduction of two high-resolution optical systems (top and bottom views) for loading of the nozzle, printer adjustment and calibration followed by imaging of the printed structures, and (iv) in-built computer-assisted alignment for printing on the already existing structures. A 3-axes positioning stage (Exaddon AG, CH) ensures a maximum volume of 200 × 70 × 60 mm^3 for the printing space with ±250 nm and 5 nm positioning accuracy along *x-y* and *z* directions respectively at a 0.1 nm sensor resolution. The positioning time from a voxel to the next is under 50 ms and the printing substrate area is 12 × 12 mm^2, with which the WE is connected.

Influence of voxel size and volumetric deposition speed on different apertures

The micro-printing setup is capable to finely tune the nozzle aperture, applied pressure (p), electrodeposition potential (E) and voxel height (Δz). The work aims to achieve a printing speed of 1 µm/s along *z* direction with constant E and Δz, while varying nozzle opening size and p. Figure 2 shows SEM images of different tip apertures obtained by contact lithography (300 nm and 500 nm) and FIB milling of closed pyramidal probes (100 nm, 1 µm and 2 µm). For electrodeposition of Cu in form of pillars, a printing speed of ~1 µm/s can be obtained at E= -500 mV and p=10–500 mbar. In the micro-printing setup, the pillar array is plated in a voxel-by-voxel manner with constant Δz= 500 nm leading to a print rate of 2 voxels/s. The array contains 50 µm long cylindrical pillars (100 voxels) printed at different p (with 10 mbar step size) for each aperture size. The pillar growth is observed linear after exceeding the first 5 µm length. While analysing the pillar diameter, it has been found that the pillar diameter can be tuned in the range of almost one order of magnitude by adjusting the pressure for each aperture (Figure 3a). Similarly, the voxel diameter can be adjusted by almost two orders of magnitude while varying both the aperture size and pressure. This leads to a throughput of Cu over three

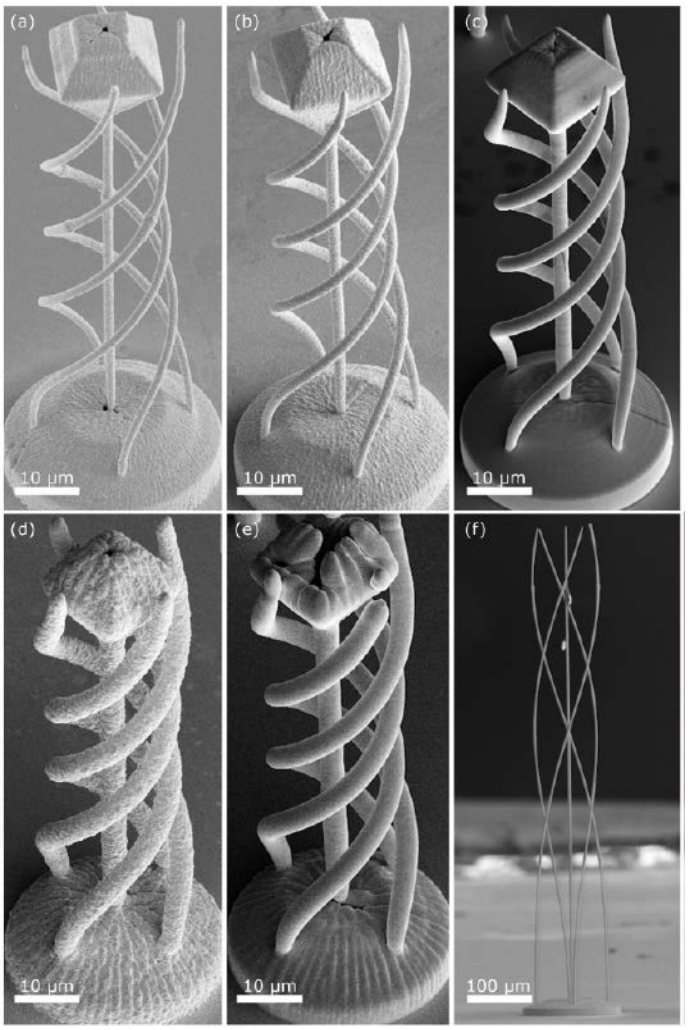

Fig. 4: *A demonstration structure printed each time with a different tip aperture ranging in size from (a-e) 100 nm to 2 µm like in figure 3. (f) A larger 650 µm-tall structure was printed with a 300 nm tip, reaching an aspect ratio of 1:100 (strands).*

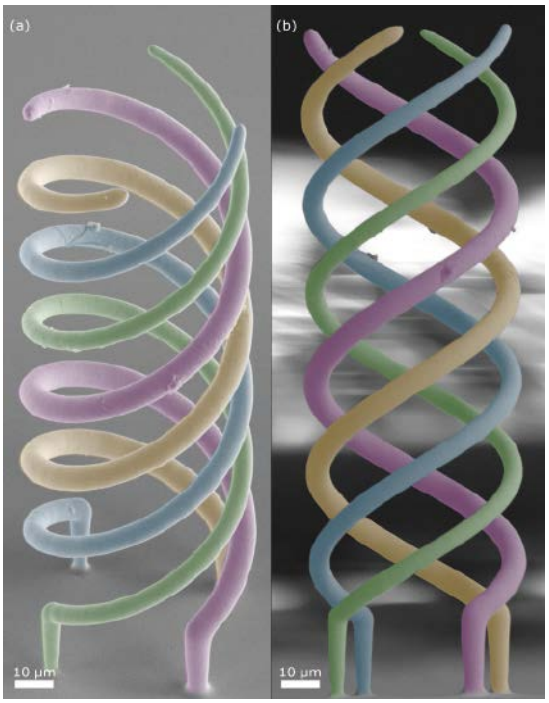

Fig. 5: *SEM images (colored) of four intertwined helices printed with a 500 nm nozzle, each helix printed at a different pressure to showcase the flexibility and the ability to change and control the voxel diameter within the same structure. About 3056 voxels were printed in 25 min to obtain the 180 µm-tall structures. (a,b) Two different views of the same subject.*

orders of magnitude (µm³/s). The volumetric deposition speed ($\dot{V}$) increases linearly when p< 100 mbar and the corresponding linear fits indicate constant plating efficiency over a wider range, particularly at the smaller aperture size. An example of this is very small $\dot{V}$ values for 100 nm aperture tip. On the other hand, $\dot{V}$ deviates from linearity and begins to saturate at p> 100 mbar indicating electroplating of a smaller fraction of ejected Cu ions on the pillars (Figure 3b).

An analytical model for the laminar flow of Newtonian fluids based on the Hagen–Poiseuille equation has been used to theoretically assess the flow through the micro-channel. The elliptical and rectangular duct shapes are used to mimic lithographic and FIB milled apex tips respectively. Both micro-channel and tip opening have their own flow resistance and the flow is assumed to be proportional to the measured $\dot{V}$. Calculations show a linear relation between $\dot{V}$ and p at either low p or more precisely at low $\dot{V}$, whereas a loss of linearity is observed at high $\dot{V}$ indicating a reduction in the plating efficiency (Figure 3c). So, the fraction of Cu ions is reduced at high $\dot{V}$, which is caused by the flow ejected from a small aperture. When the ratio $\dot{V}$/p (within the linear range) is plotted as a function of the equivalent diameter of tip aperture, the flow is dominated by the aperture for smaller diameters but by the micro-channel for larger diameters with a transition zone in between them (Figure 3d).

Layer-by-layer printing at different apertures and pressures

After the thorough analysis of EC printing process related to cylindrical pillars, a complex-shaped micro-scale structure is designed. The structure contains four intertwined helices with a pillar in the middle, and a double truncated pyramid sitting on the top of that (Figure 4). The true layer-by-layer nature of the printing process is highlighted while printing the combination of the helices with the pillar, whereas printing the pyramid shows the ability to produce any overhanging details. The total number of voxels associated with this structure is 9171. During printing of this voxel coordinate list, 90 mbar and 40 mbar pressures have been

used for 100 nm and 300 nm apertures respectively (Figure 4a,b), whereas 25 mbar pressure has been applied for other large apertures (Figure 4c,d,e). The voxel area is found uniform within each structure. The total printing time is observed as 100 min and 35 min for the smallest (100 nm) and largest (2 µm) apertures respectively. Further to this, a 650 µm long structure with 120 µm diameter base and 3 µm diameter strands have been printed at 100 mbar pressure for 300 nm aperture size. This structure contains 20,000 voxels and takes 120 min to be completed (Figure 4f).

Layer-by-layer printing with each voxel at a different pressure

To emphasize the possibility of tailoring the voxel area by only adjusting the pressure, a structure of four helices having four different diameters has been designed. Figure 5 shows SEM images of such a structure, where four resulting wires are artificially coloured for better visualization. This kind of structure can be obtained in a layer-by-layer fashion by using a single aperture (i.e. 500 nm), where each of the four voxels from each layer is plated at different pressure (such as 20, 40, 60, and 80 mbar). However, time response of the pressure value is the main challenge during growth of multiple strands in parallel at different pressures. As a result, the cloud of Cu^{2+} ions rapidly changes with the movement of nozzle from one strand to another leading to a visible difference in the wire diameter. Figure 5 confirms that the four intertwined wires are homogeneous along the length, but have diameters of 5, 6, 7, and 8 µm respectively. For individual pillars, the expected diameters at those pressure values are 2, 3, 3.7, and 4.4 µm respectively (from Figure 3a). This additional growth observed for the intertwined helices is attributable to the plating occurring during the lateral motions from a strand to the next, which is absent during printing of the individual pillars.

Summary

A novel additive micro-manufacturing system has been designed to optimize EC printing of copper by minimizing the response and positioning times and the same approach can be applied for other conventional metals. The influence of the applied pressure and probe aperture on the lateral diameter of the electroplated copper voxels has been investigated while keeping the EC deposition potential and the voxel height fixed. This has enabled the voxel area to cover over three orders of magnitude and more importantly over two orders of magnitude using the same aperture. The capability has been exploited to fabricate copper micro-scale structures of 60 × 60 × 180 μm^3 and 120 × 120 × 650 μm^3 with a submicron resolution, followed by a 50 × 50 × 170 μm^3 structure of four helical wires by changing the pressure on a voxel-by-voxel basis. Each of these four helical wires is homogeneous along the entire length but has a different diameter as obtained when deposited at different pressure during layer-by-layer printing. This indicates a significant throughput increase with a possibility of tuning the voxel size depending on the feature dimensions within the same design.

Digest of
Ercolano G, Zambellii T, van Nisselroy C, et al.; Multiscale additive manufacturing of metal microstructures; Advanced Engineering Materials 2020;22, 1900961.
https://onlinelibrary.wiley.com/doi/10.1002/adem.201900961

Multi-step Crystallization of Self-organized Spiral Eutectics

Moniri S, Bale H, Volkenandt T, et al.

Introduction

With decade-long research on crystallization phenomena in many scientific fields, it is possible to control the processing of virtually all metals and alloys to produce different transient states by solidification via crystallization at any intermediate time scale. The non-equilibrium routes to create metastable states are advantageous in terms of unveiling patterns unknown or unseen to the conventional equilibrium techniques. One such appealing research field with immense technological promise is spiral eutectics, where mixtures of two or more solid phases grow simultaneously from a parent liquid phase and arrange into intricate spiralling patterns. The conventional route to manufacture spiral eutectics is a top-down approach, where speed and complexity increase with the number of helices leading to a bottleneck for large-scale production. However, their implementation has been largely hindered due to the lack of technical insight on their growth mechanism as no dominant influence of any process parameters on the spiral formation has been recognized. To date, the spiral patterns have been obtained for Al-Th, Al-Ag-Cu, and Zn-Mg alloy systems along with a few other non-metallic systems. In this work, a systematic investigation has been undertaken to investigate the origin of spiral growth in Zn-Mg alloys produced via directional solidification (DS). To trace the development of as-solidified microstructures from the parent liquid, correlative and multiscale microscopy incorporating 3D measurements together with *in situ* and atomic-resolution imaging has been employed. Machine learning has been used to track the interfaces of the complex eutectic colonies, in which metastable $MgZn_2$ Laves phase initially nucleates from the liquid, followed by screw dislocations intersecting the solid-liquid interfaces and catalysing the spiral growth of the two-phase microstructure. Extensive dislocation-driven growth, which allows simultaneous growth of two phases upon spiral eutectic crystallization, is observed. It indicates the opportunities for rapid fabrication and additive manufacturing of 3D chiral photonic materials.

Experimental details

A vacuum arc-melting (VAR) cast Zn-3 wt% Mg alloy was EDM cut into cylindrical rods (1 mm diameter by 5 mm length) followed by two-phase eutectics growth via DS in a three-zone vertical Bridgman furnace. The temperatures of the three zones were independently fixed to impose the temperature gradient on the fully molten samples. For stationary samples, growth velocity was controlled by the upward, simultaneous movement of the zones. For gradient freeze samples, zone temperatures were decreased at fixed rates under the imposed thermal gradient. Optical microscopy was used to locate the spiral regions-of-interest in these DS samples and then a laser micro-machining system was used to thin down the region-of-interest (60 µm diameter by 100 µm height) for 3D imaging via lab based X-ray nano-tomography (nTXM). 3D EBSD measurements were obtained to understand the hetero-epitaxial relationship, crystallographic growth direction, and interphase habit plane orientation between two spiral eutectic constituents. *In situ* synchrotron high-energy X-ray diffraction (HEXRD) was used to understand the sequence of phase formation during solidification. Both TEM and S/TEM were used to observe the screw dislocation defects within seed $MgZn_2$ crystals.

Microstructure and morphology of spirals

The crystallization pathway leads to two competing growth forms depending on the combination of constant velocity and unidirectional thermal gradient – (i) thermodynamically stable, rod-like Zn-Mg_2Zn_{11} and (ii) metastable, spiral Zn-$MgZn_2$ eutectics as confirmed via energy-dispersive X-ray spectroscopy. Combining the scanning electron micrographs of all DS Zn-$MgZn_2$ samples, a total of 195 spirals are observed among which an equal proportion of spiral handedness (99 right-handed and 96 left-handed spirals) is found. Typically eutectic spirals show helical morphology and the same holds for Zn-$MgZn_2$ spirals (~100 nm spiral thickness and ~1 µm interphase spacing) as observed from the nTXM microstructures. The reconstructed 3D nTXM images are segmented via a machine-learning algorithm to label both the eutectic Zn and $MgZn_2$ phases and an excellent agreement between the segmented and fully reconstructed output structures is observed in the unprocessed data. Figure 1 shows the complete 3D morphology of spiral eutectics. The pyramidal-shaped spiral eutectic nodules (colonies) are randomly oriented inside the bulk volume and an irregular Zn-$MgZn_2$ spiral with coarser and non-periodic lamellar spacing is observed outside the colonies (Figure 1A). The internal microstructure displayed orthogonally along the z-axis (Figure 1B) and its close-up view (Figure 1C) confirms that the crystallographic anisotropy of the $MgZn_2$ phase plays an important role during solidification resulting in hexagonal-shaped colonies, spirals with intra-facet angle $\phi = 10°$ and dihedral angle $2\theta = 18°$, uniform spiral thickness and a common nucleation site for termination. The degree of directionality of these colonies in the reference frame is quantified by calculating the stereographic projection of the normal to the solid-solid interfacial patches (Figure 1D) and the resulting interface normal distribution (IND) represents the superposition of all lamellar orientations found within the colony indicating six-fold symmetry of the Zn-$MgZn_2$ facet planes as denoted by sharp peaks (Fig-

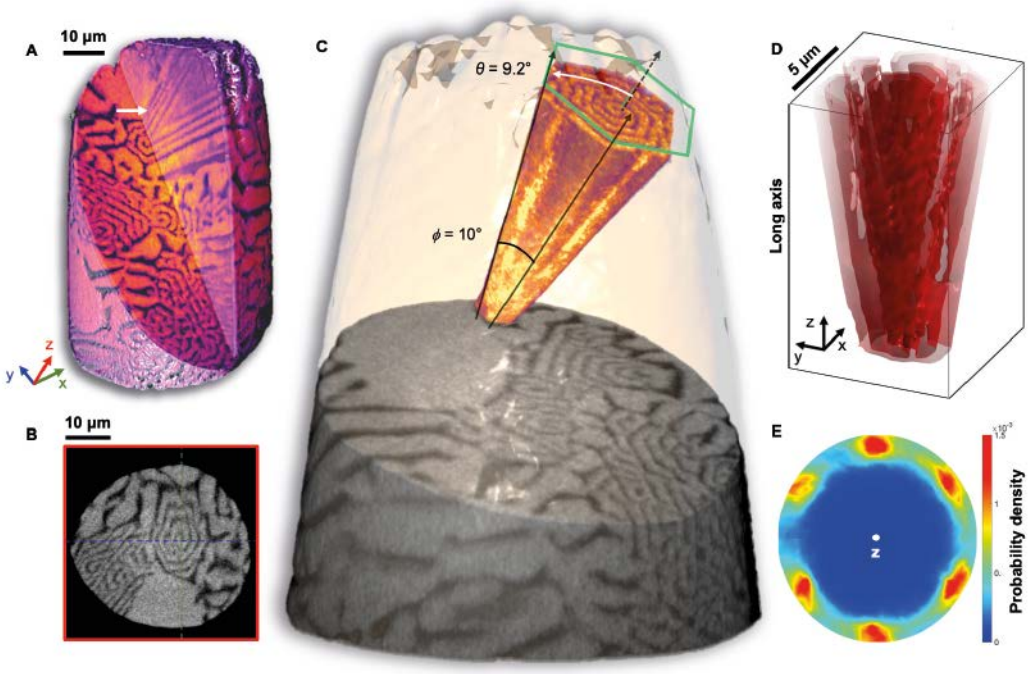

Fig. 1: 3D morphology of spiral eutectics. (A) Full X-ray nano-tomographic region-of-interest displaying multiple spiral eutectic colonies. The white arrow shows the pyramidal shape of a spiral colony. The reconstruction is cut out to reveal the microstructure internally. The eutectic $MgZn_2$ and Zn phases are shown in dark and light false colours, respectively. (B) View along the cut seen from the y-axis. The eutectic $MgZn_2$ phase is shown in dark grey. (C) Close up view of the spiral. The spiral colony pointed to by arrow in (A) is extracted, and its surrounding is rendered translucent orange for clarity. The graduation in the spiral's color is due to the false colouring scheme used for visual clarity. The hexagonal enveloping shape along with the inter-planar (dihedral) angle 2θ (≈18°) and intra-facet angle (10°) are annotated. (D,E) Solid-solid interfaces and their directionality within the spiral. The Zn-$MgZn_2$ interfaces (D) are extracted from the 3D reconstruction and are used to quantify the preferential directionality of the colony in the laboratory frame (E). The interface normal distribution (defined in main text) reveals the sixfold symmetry of the solid-solid interfaces, which correspond to the sharp peaks.

ure 1E). These nTXM results show the first direct evidence for the hexagonal-shaped spiral Zn-$MgZn_2$ eutectic colony, terminated at an apex by a nucleation center.

Epitaxial relationship between spiral constituents in 3D

The crystallographic texture, particularly the grain rotations, is assumed to influence the complex morphology of the faceted spirals. Figure 2 summarises the hetero-epitaxial relationship between two eutectic spirals. Figure 2A shows the 3D orientation map of a spiral eutectic colony situated at the junction of three single-crystalline Zn grains. It has $[0001]_{MgZn2}$ growth direction along with a negligible intra-lamellar misorientation (~1°). The misorientation between the two eutectic phases can be visualized from the individual 2D cross-section orientation maps along Z direction and superimposing the unit cell on each grain using the respective Euler angles (Figure 2B). Both single-crystalline Zn and $MgZn_2$ phases within the given colony maintain their epitaxial relationship, which is verified by the small (<3°) angular deviation between the pairs of coincident planes between Zn and $MgZn_2$. This also helps to understand the solid-solid interfaces by constructing an IND in the crystallographic frame. Figure 2C shows the crystallographic interface normal distribution (CIND) along $[0001]_{MgZn2}$ providing a quantitative perception into the crystallographic properties of the spiral eutectic. The six peaks of the CIND indicate $\{7072\}_{MgZn2}$ orientation for solid-solid interfaces, where interphase boundaries shown on opposite ends of the CIND (such as $(\bar{7}072)_{MgZn2}$ and $(70\bar{7}2)_{MgZn2}$) meet at the apex of the pyramidal spiral and the interplanar angle is calculated ~18°, verifying the nTXM observations (Figure 1).

Two-step crystallization pathway

Figure 3 summarizes the HEXRD results for sequencing phase formation by acquiring Laue patterns as a function of diffraction angle 2θ. The fast kinetics of nucleation can be temporally understood from the summary of the 400 diffraction spectra collected during 200 seconds of solidification time. The diffraction peak for the first solid phase to form belongs to the $MgZn_2$ (dashed line at ~1.0 s, 2θ ~2.9°), whereas peaks correspond to the Zn phase appearing ~2 seconds later. These results confirm

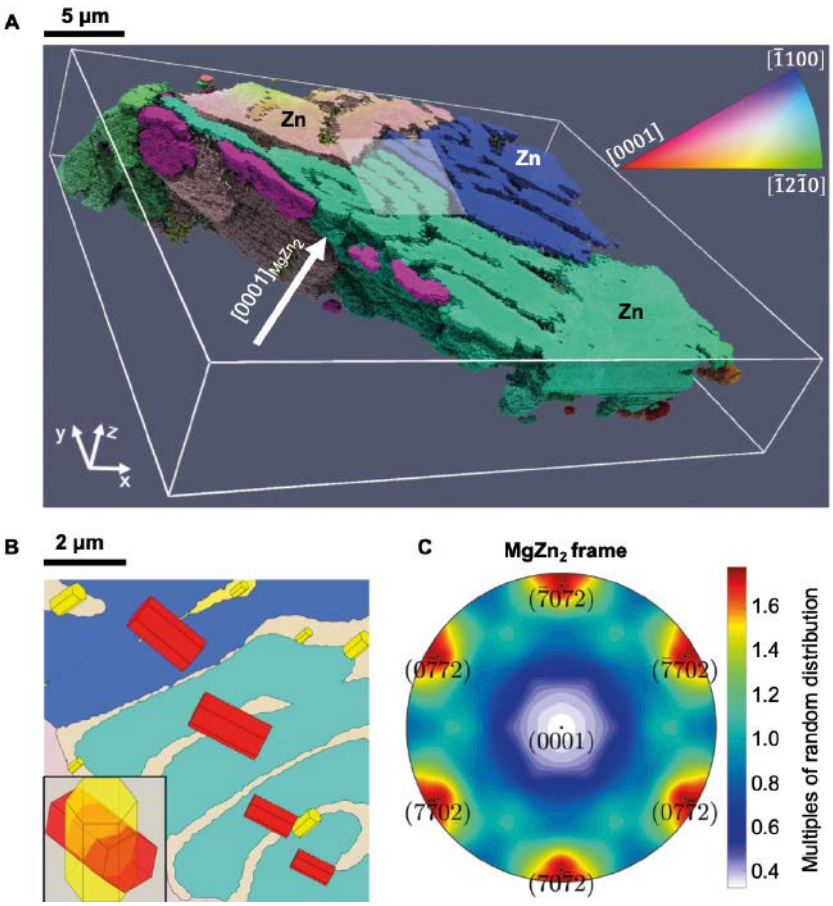

Fig. 2: Heteroepitaxial relationship between the two spiral eutectic constituents. (A) 3D orientation map (3D EBSD) of a spiral eutectic colony. The spiral is situated at the junction of three single crystalline Zn grains (navy, turquoise, tan). The faceted $MgZn_2$ phase is rendered transparent for clarity; the Zn grains (voxels) are coloured according to their orientation following the stereographic triangle on the top-right. The growth direction of the spiral is along $[0001]_{MgZn2}$. (B) Orientation map of one representative slice with unit cells superimposed using the respective Euler angles (Zn: red; $MgZn_2$: yellow). Facets of the unit cells correspond to the $\{10\bar{1}0\}$ and {0001} planes. Both phases are single-crystalline. The map corresponds to the transparent box shown in (A). Inset: the misorientation between the two phases. (C) Distribution of the crystallographic orientation of the solid-solid Zn-$MgZn_2$ interfaces. The plot of the crystallographic interface normal distribution (defined in main text) is shown along {0001} axis of $MgZn_2$. The six crystallographically symmetric poles of high probability reveal that the solid-solid interfaces have the $\{70\bar{7}2\}_{MgZn2}$ orientation. The interplanar angle, for example, between $\{\bar{7}072\}_{MgZn2}$ and $\{70\bar{7}2\}_{MgZn2}$ is ≈18°, matching the observation from X-ray nano-tomography (Figure 1).

the sequence of phase formation and more importantly provide direct evidence of the initial $MgZn_2$ particle formation, which promotes nucleation of the Zn-$MgZn_2$ eutectic. These observations further support the detection of seed crystals in nTXM at the apex of the pyramidal spirals (Figure 1 and Figure 2).

Atomic visualization and development of spiral patterns from nano- to micro-scale

The TEM and S/TEM images in Figure 4 confirm the presence of screw dislocations within hexagonal-shaped seed $MgZn_2$ crystals. When TEM images are taken along $[\bar{1}2\bar{1}0]_{MgZn2}$ zone axis, the dislocation contrast remains invisible upon exciting the (1010) family of diffraction spots (Figure 4A), but becomes visible during excitation of the (1011) diffraction vectors parallel to the spiral growth axis (Figure 4B). Thus the dislocation lies preferentially along with the $[0001]_{MgZn2}$ spiral growth direction, which is consistent with the dislocation of a screw character. As $MgZn_2$ has a hexagonal crystal structure and an elastically symmetric basal plane along with its perpendicular planes, thus all dislocations lying on those planes exhibit pseudo-elastic isotropy. Direct visualization of the screw dislocation is observed in Figure 4C with coloured lines guiding the shearing of the atomic planes. The equal probability of spiral-handedness suggests an equal probability of the dislocation sense, and thereby further supporting the screw-mediated spiral growth.

The crystallization mechanism of spiral Zn-$MgZn_2$ eutectics under non-equilibrium conditions is schematically shown in Figure 5. The first phase to crystallize is $MgZn_2$ and its preferential nucleation demonstrates considerably low solid-liquid interfacial energy (due to its poly-tetrahedral structural similarity between the melt and $MgZn_2$ Laves phase) as compared to the stable Mg_2Zn_{11} phase. The spiral growth of the seed $MgZn_2$ crystal is permitted through self-perpetuating steps provided via axial screw dislocations (Figure 5A). As the seed crystal grows, the high strain field around the screw forms a hollow core to relieve the strain energy, which is energetically more favourable than retaining the strain energy of the dislocation (Figure 5B). When the system cools down below metastable eutectic temperature, the Zn phase hetero-epitaxially nucleates along with the spiral $MgZn_2$ growth steps and grows in a coupled manner with $MgZn_2$ phase (Figure 5C). During this eutectic growth, low-energy solid-solid $\{70\bar{7}2\}$

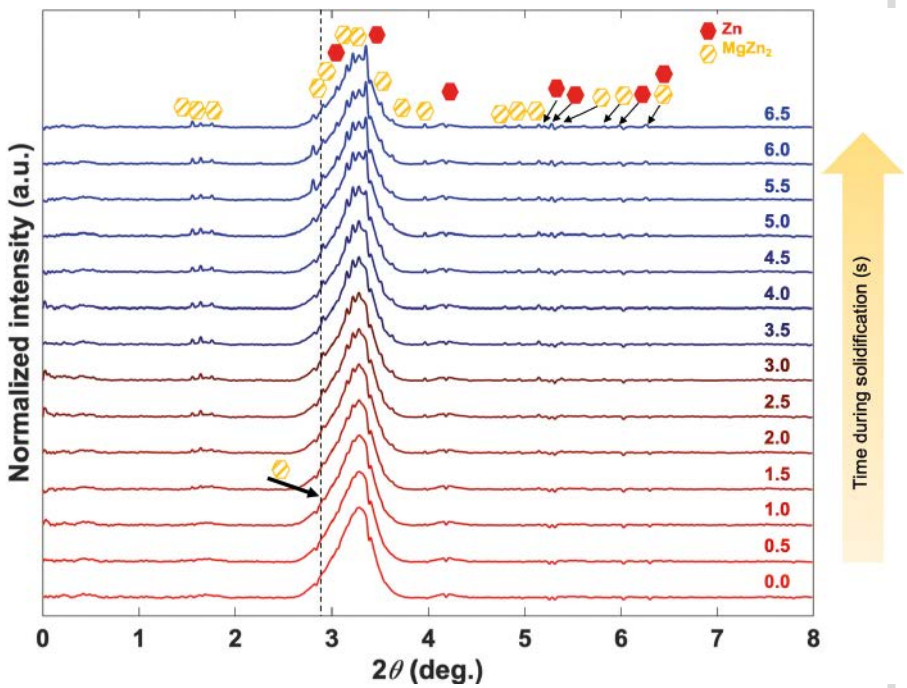

Fig. 3: Sequence of phase formation during solidification. The in situ high-energy X-ray diffraction (HEXRD) spectra acquired at the indicated time-steps after the start of solidification (0.0 s) show that $MgZn_2$ is the first solid phase that forms (dashed line at 1.0 s, $2\theta \approx 2.9°$)

$_{MgZn2}$ interfaces are maintained and the interphase boundaries follow a specific crystallographic growth direction. As the eutectic spirals nucleate on the axial screw dislocations, the regularity of the two phases is ensured by the spiral growth steps. Figure 5D shows a fully-developed spiral colony with solid-solid interfaces, intra-facet angles, and growth direction. Conventionally, the solid-liquid interface of the rod-like Zn-Mg_2Zn_{11} eutectic consists of a regular orthogonal to macro-faceted cellular structure, in which parallel, regularly spaced lamellae connect to a common trigonal spine. As this cannot describe the complex regular spiral morphology of Zn-$MgZn_2$, the current work explains the role of screw dislocations of the primary $MgZn_2$ phase in catalysis of the heterogeneous nucleation of the eutectic phases during solidification eventually causing the spiral growth form. The proposed crystallization mechanism indicates the 'hidden' role of poly-tetrahedral phases in assisting heterogeneous nucleation.

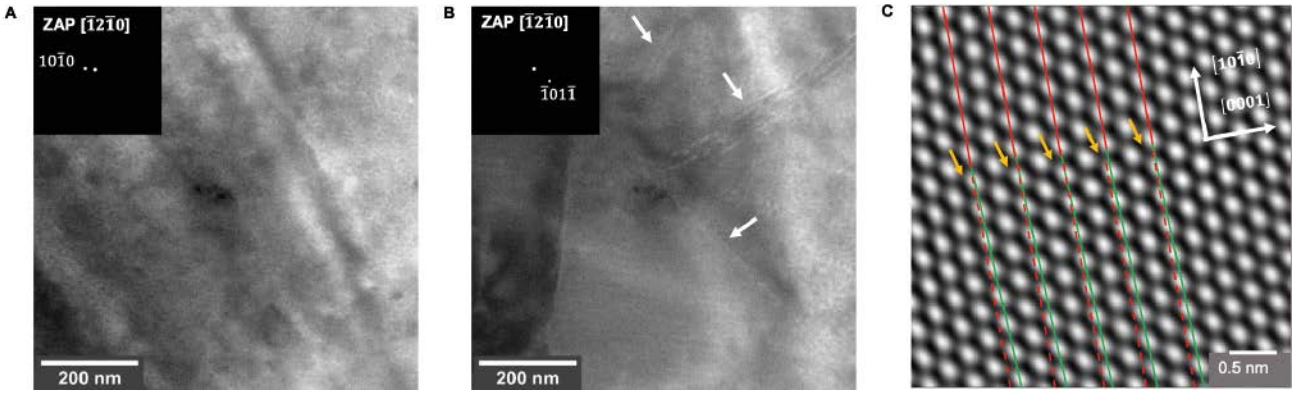

Fig. 4: S/TEM observation of screw dislocations within "seed" $MgZn_2$ crystal. (A,B) Diffraction-contrast TEM images taken under the strong two-beam conditions defined by the diffractions as insets to the images near the $[\bar{1}2\bar{1}0]_{MgZn2}$ zone axis. Dislocations are invisible upon excitation of diffraction vectors perpendicular to the $[0001]_{MgZn2}$ direction, for example the $[10\bar{1}0]$ spot in (A). Dislocation lines become visible (white arrows) when the diffraction vector has a parallel component to the $[0001]_{MgZn2}$ direction, for example, the $[\bar{1}01\bar{1}]$ spot in (B). Therefore, the dislocation lies along the $[0001]_{MgZn2}$ direction, which is also the growth direction (Figure 2). Since both the growth and dislocation directions are along $[0001]_{MgZn2}$, this behaviour is consistent with a dislocation of screw character. (C) Atomic-resolution high-angle annular dark-field (HAADF) image taken along $[11\bar{2}0]_{MgZn2}$ showing screw dislocations aligned along $[0001]_{MgZn2}$. Solid red and green lines indicate the shearing of atomic planes, characteristic of the side-view of a screw dislocation; dashed red lines indicate the position of atomic columns in the absence of screw dislocation. The orange arrows point to atomic columns around the screw dislocation core.

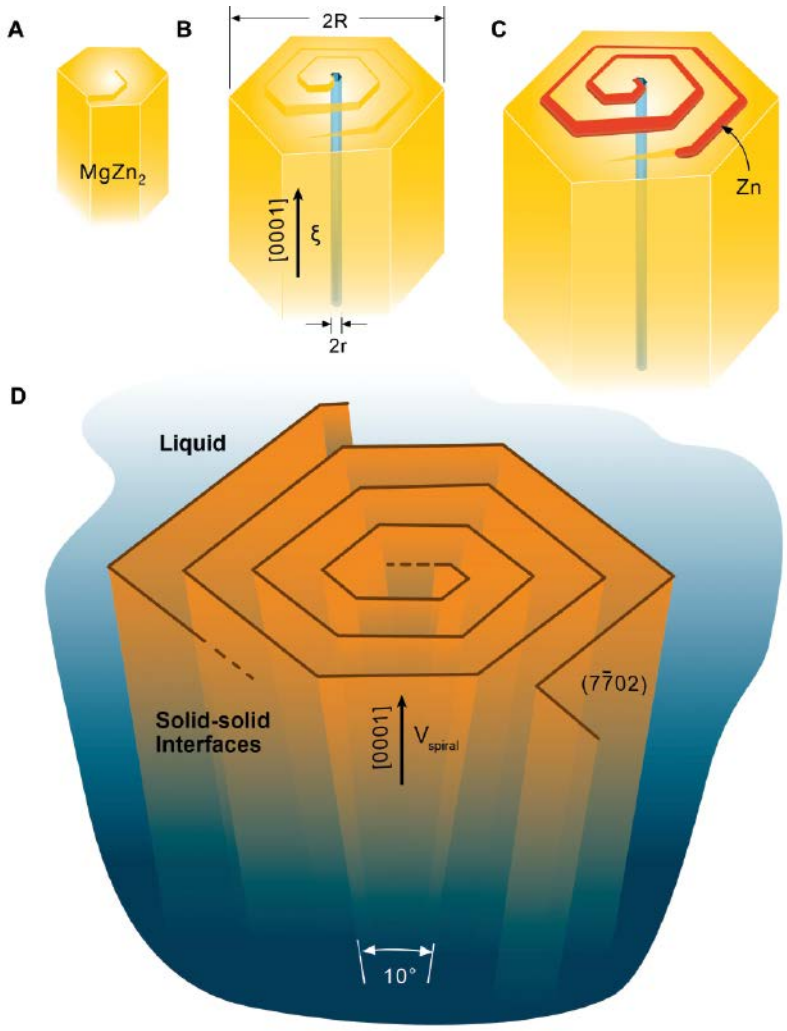

Fig. 5: Illustration of the screw dislocation mediated growth of spiral eutectics. (A) Establishment of a spiral ramp due to axial screw dislocation on the seed $MgZn_2$ crystal. The ramp provides self-perpetuating steps that enable spiral growth. (B) Growth of the seed crystal and formation of a hollow core. The axial growth direction of the spiral is along $[0001]_{MgZn2}$. For sufficiently large Burgers vector, the strain energy is alleviated by hollowing out the dislocation core (thin blue cylinder), in agreement with Frank's hollow-tube mechanism.[30] Radii of the seed and hollow-core are R and r, respectively; ξ is the sense vector of the dislocation. (C) Heteroepitaxial growth of Zn (red, not to scale) along the exposed $MgZn_2$ growth steps (ledges). (D) Spiral eutectic colony during the growth process. Only solid-solid interfaces are shown for clarity. The habit planes of the spiral are $\{7\bar{7}02\}_{MgZn2}$. The intra-facet angle is ≈10°, for example, between $\{7\bar{7}02\}$ and $\{70\bar{7}2\}$.

Summary

A spiral, two-phase microstructure with an intrinsic chirality and a faceted, periodic architecture has been synthesized and its formation mechanism along with morphological and hetero-epitaxial relationships between two phases has been investigated by the correlative characterization assisted by data science methods. The macroscopic spirals appear via microscopic defects through a two-step crystallization process. Initially, the poly-tetrahedral phases readily nucleate in the liquid due to their low interfacial energy and provide adequate screw dislocations for crystallization of the spiral eutectic representing the widespread applicability of Frank's defect-driven growth mechanism to multi-phase materials. The 3D simulation of complex spiral self-organization patterns has set a benchmark for designing the next-generation alloys with superior properties. This tends to open exciting opportunities for multi-phase structures serving as templates for rapid fabrication or additive manufacturing of 3D chiral photonic crystals.

Digest of
Moniri S, Bale H, Volkenandt T, et al.; Multi-step Crystallization of Self-Organized Spiral Eutectics; Nano°Micro°Small 2020;16, 1906146.

https://onlinelibrary.wiley.com/doi/10.1002/smll.201906146

X-ray Microtomography of Thermal Cycling Damage in Sintered Nano-silver Solder Joints

Regalado IL, Williams JJ, Joshi S, Dede EM, Liu Y, Chawla N

Introduction

High power density devices made of wide band-gap materials such as silicon carbide and gallium nitride have improved the maximum operating temperatures to 300°C, operating voltages over 600V, and switching frequencies to high enough. Differences in mechanical strength, electrical conductivity, and coefficient of thermal expansion (CTE) between various layers in a module of the semiconductor devices are critical to determining its lifetime at these extreme conditions. A very important part is the die attachment, which is required to have low processing temperatures (<300°C), stability of bonds over operating temperatures of 300°C, mechanical stability under shear loads, and good thermal and power cycling performances. Sn-based solder alloys have usually been used as die attachments in semiconductor devices, but their application has been limited due to the low melting point and tendency to form intermetallic compounds leading to brittle interfaces and premature failures. A promising material fulfilling these requirements is sintered nano-Ag solder, which has excellent thermal and electrical conductivities, relatively low processing temperature (250°C), and high melting temperature similar to that of bulk-Ag properties. Thermally induced damages are the leading cause of failure in power electronics, thus thermal and power cycling reliability tests are used to evaluate the reliability of die attachments. Samples are typically subjected to cyclic heating and cooling to induce damage on the solder followed by the analysis of the microstructural damage, however, that is not sufficient to quantify the crack formation and growth within the same sample as a function of time. Among the non-destructive testing techniques, 3D X-ray tomography has been proven to be excellent to analyse and quantify the degradation of various material systems, such as Al-7075, Cu_6Sn_5 intermetallic, etc. This work focuses on a 4D approach to study the thermal cycling damage of sintered nano-Ag solder as a function of time. X-ray tomography has been used to study the thermally induced solder degradation and accurately quantify the cracks/void growth. Moreover, theoretical models have been utilized to estimate Young's modulus as a function of porosity and then experimentally validated using nano-indentation and shear testing.

Experimental details

Figure 1 shows the die attachment structure consisting of a direct bonded copper (DBC) substrate with a 600 µm AlN layer bonded to a 200 µm Cu layer on either side. Both the DBC and Si die (500 µm thick, polished on a single side) were metalized via electron beam deposition technique to enhance good bonding of the die attachment. Single side metallization on the DBC and Si die con-

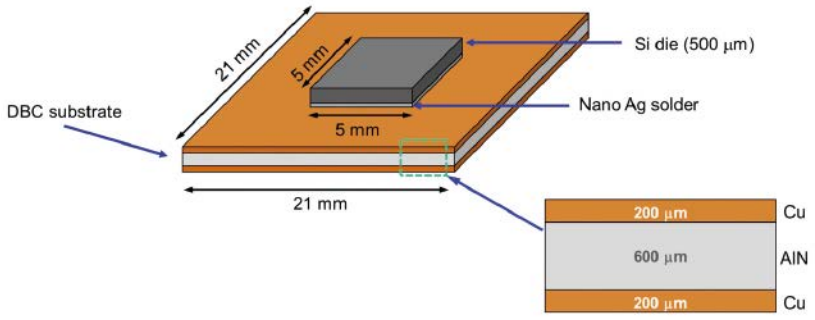

Fig. 1: Die attachment structure consisting of a DBC substrate, nano-Ag solder as a die attach material and a single side polished Si die.

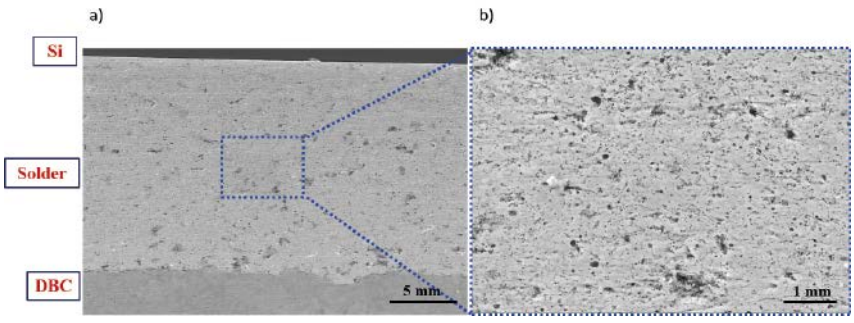

Fig. 2: (a) Fifteen µm-thick nano-Ag solder bond, good adhesion can be seen at the Si-solder and solder-DBC interfaces, (b) Zoomed image of nano-Ag bond, homogenous distribution of pores can be observed.

sisted of a 50 nm adhesive titanium layer, followed by a 1 µm strong Ag base layer and a 50 nm thick oxidation protective Au layer. Samples from the die attachment structure were prepared using a low temperature-low pressure sintering procedure (heating ramp rate of 4°C min^{-1} until 250°C peak temperature was reached, which was then held for 30 min at 0.4 MPa pressure, followed by the bond cooling rate of 20°C min^{-1}) on a programmable hot plate. The shear tests were done in displacement control, with a nominal strain rate of 10^{-4} s^{-1} and the fractography analysis was carried out in an SEM. The thermo-mechanical behaviour of the bonded samples was tested at three different thermal cycling conditions of 230°C, 180°C, and 155°C respectively at constant heating and cooling rates of 2–4°C min^{-1}, dwell time of 45–60s and total cycle time of 4 min $cycle^{-1}$. 3D X-ray tomography was done on a lab-scale X-ray microscope system before and after the thermal cycles to understand the effect of thermal cycles on the microstructure. Nano-indentation was used to analyze the mechanical properties of the individual micro-constituents in the stack with a Berkovich indenter at a depth of 1 µm.

Microstructural characterization and nano-indentation of constituents

Figure 2 shows a 15–30 µm thick cross-section of the nano-Ag bond at different magnifications. The sintered solder showed good densification with a total macroscopic porosity <10% and FIB cross-sections showed that the microscopic porosity is ~35%. A few pores of ~100–200 nm diameter were homogeneously distributed through the solder volume. Good adhesion was observed at the Si/solder and solder/DBC interfaces due to the metallization layers deposited on the bonding side of the chip and DBC substrate. From the nano-indentation results, the highest and lowest Young's modulus (347.4 GPa and 20 GPa respectively) and hardness values (15.2 GPa and 0.5 GPa respectively) were observed in the AlN layer of the DBC substrate and nano-Ag solder respectively. This low modulus value of nano-Ag solder was due to the inherent porosity within the sintered bond, whereas ~35% volume fraction of the pores explained the difference in Young's modulus seen between bulk Ag (~76 GPa) and nano-Ag solder. The Young's modulus was further calculated as 28 GPa and 33 GPa from the O'Connell and Budiansky model and Wachtman and MacKenzie model respectively, however, both models led to slight over-estimation.

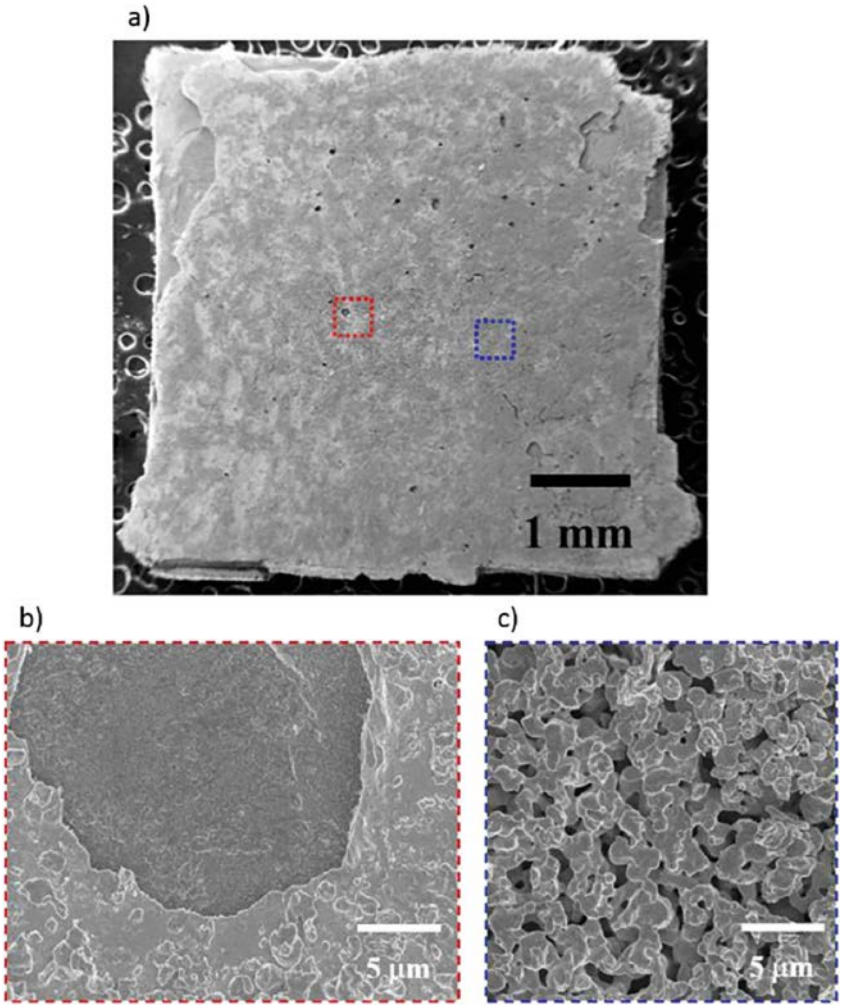

Fig. 3: Fractography SEM image of nano-Ag solder joint after shear testing, (a) fracture occurred through the thickness of the solder as seen in this image of the Si die side, (b) delamination occurring at few places on the Si die-solder interface, (c) magnified view of the nano-Ag solder showing coalescence of nano-Ag spheres.

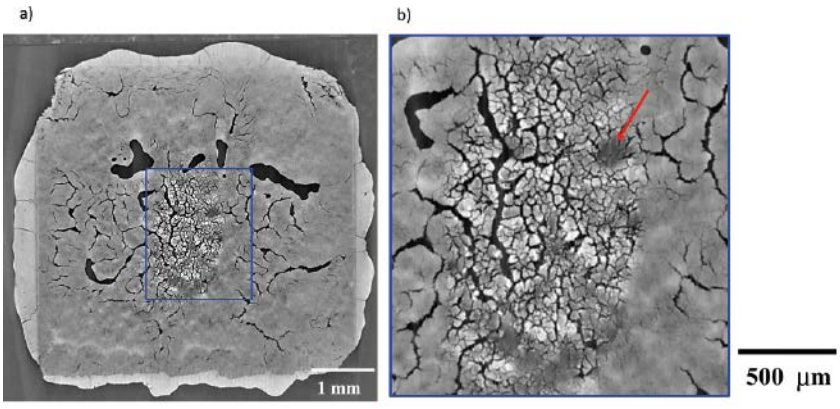

Fig. 4: (a) Microstructure of nano-Ag solder after 3000 thermal cycles with ΔT=230°C, the blue box shows the region where the delamination damage was seen, (b) Magnified view of the region of delamination of solder.

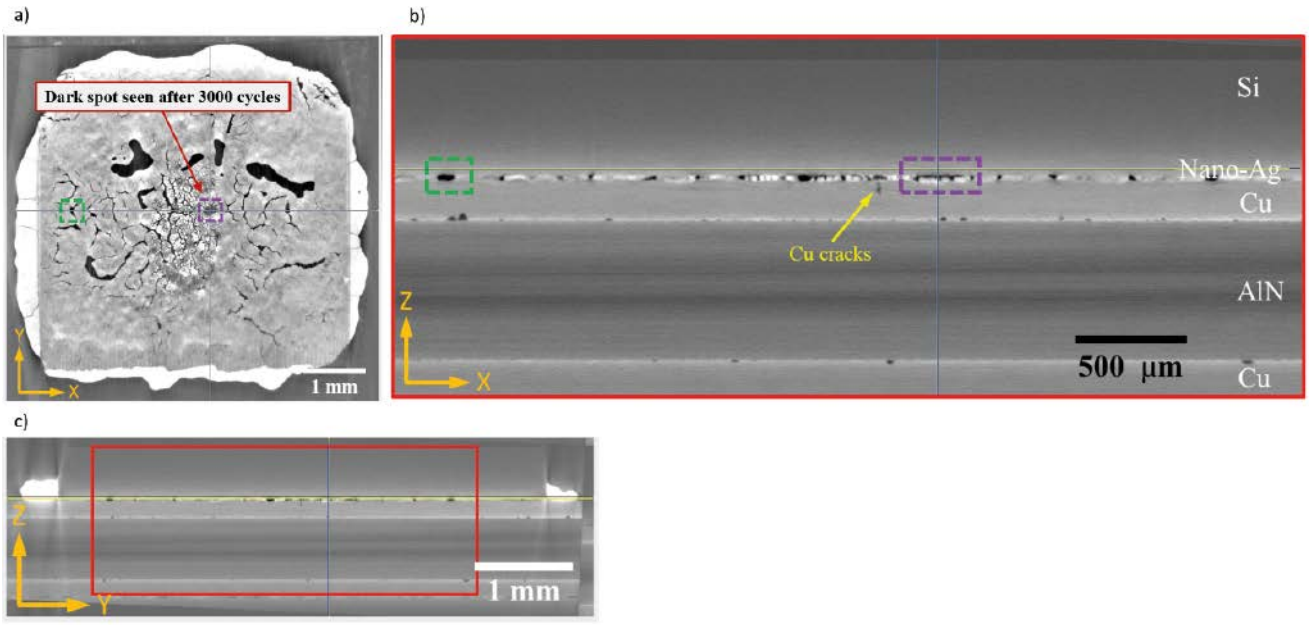

Fig. 5: Nano-Ag solder joint after 3000 thermal cycles at ΔT=230°C viewed at different planes, (a) XY view of sample showing nano-Ag solder, (b) XZ view of the solder stack showing the multiple layers in the solder joint, (c) YZ view of sample.

Shear testing

Shear testing was done to evaluate the strength of the nano-Ag bonds and the adhesion of the solder at the interfaces before the thermal cycles. The mean shear strength was 15±2.5 MPa. Figure 3a shows the occurrence of fracture through the thickness of the solder, indicating good bonding at the interfaces. A few delaminations were observed at the Si/solder interface, which might be caused by the imperfections during the metallization (Figure 3b). Figure 3c shows a magnified image of the solder after shear testing.

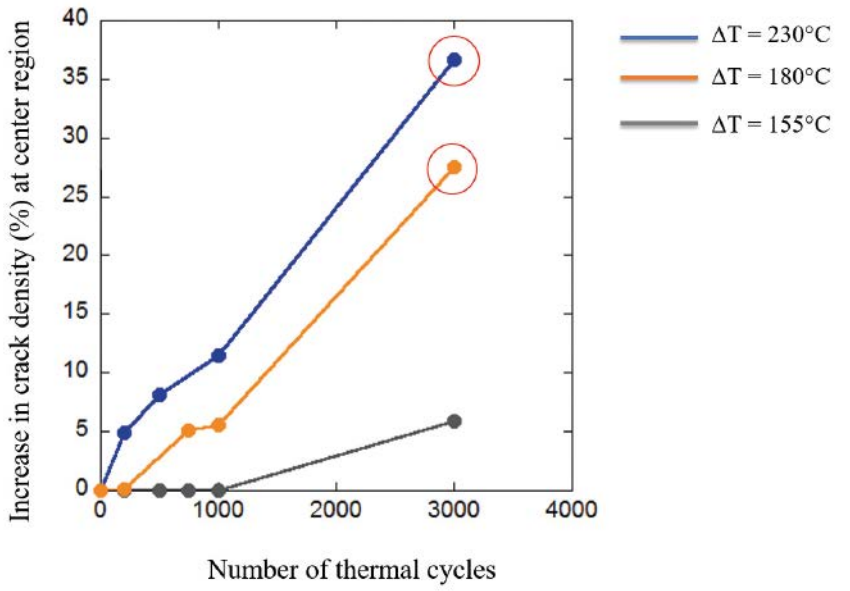

Fig. 6: Analysis of increase of crack density as a function of number of thermal cycles for Sample 1 (ΔT=230°C), Sample 2 (ΔT=180°C), and Sample 3 (ΔT=155°C). The red circle on the plot indicates delamination occurring at the solder-Si interface.

Thermal cycling and solder degradation

The as-fabricated solder contained pores due to either shrinkage of the solder or residuals of evaporated organics. The initial porosity was found as 6.9%, 8.3%, and 3.5% at 230°C, 180°C, and 155°C respectively. After 3000 thermal cycles, X-ray tomography revealed an increase in crack density within the solder volume with most of the crack formation concentrated close to the center of 230°C and 180°C samples indicating the possibility of delamination occurring at the interfaces. Figure 4 shows the degradation of the solder after 3000 thermal cycles at 230°C. Figure 5 further confirms the solder delamination from the 3D X-ray stacks analysed on different orthogonal planes. The delamination was observed at the Si/solder interface due to localized failure that occurred as a result of excessive micro-crack formation. Besides, 30–50 µm long cracks were also formed within the Cu layer in the DBC substrate only after initial 300 and 500 thermal cycles at 230°C and 180°C respectively. These cracks were observed directly below the most damaged section of the solder leading to delamination after 3000 cycles. Interconnection of poros-

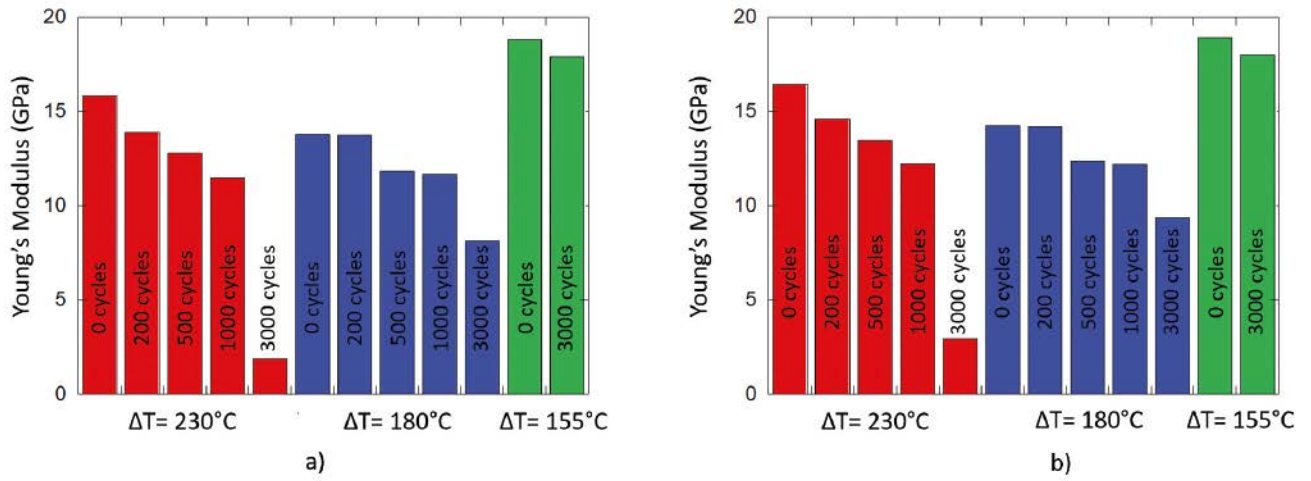

Fig. 7: Decrease in Young's modulus for quadrant 5 for ΔT=230°C, ΔT=180°C and ΔT=155°C according to (a) Wachtman and MacKenzie relation (b) O'Connell and Budiansky relation.

ities and cracks favoured the rapid crack growth at higher crack densities. The rate of crack formation was decreased significantly at 155°C, where micro-cracks were initiated only after 3000 cycles causing no delamination. Figure 6 shows a comparison in crack density for each sample from a particular region, where the crack formation was highest and delamination was appeared. When crack density exceeded 30%, the delamination was occurred for all samples except the tests performed at 155°C.

Damage analysis and related modelling

Overlay of the segmented images experiencing 0 and 3000 thermal cycles at 230°C, 180°C, and 155°C were used to quantify the induced damage on the solder. The volume of the samples was divided into 9 sections for a thorough analysis of the microstructural degradation. ~35% increase in the crack density was observed at the centre (section 5) of the sample tested at 230°C with the least amount of cracks at the corners. The increase in crack density at the centre was observed as ~15% and ~3.5% for samples tested at 180°C and 155°C respectively indicating the effect of peak temperature on solder degradation. Both Wachtman and MacKenzie model and O'Connell and Budiansky model were further used to calculate Young's modulus value at each of the 9 sections of all three samples, however, the accuracy and effectiveness of the O'Connell model were unknown for >56% crack density. As most of the thermal-induced damage was observed at the centre, so the highest decrease in Young's modulus was found there at 230°C and 180°C, but less pronounced at 155°C. Figure 7 shows histogram plots summarizing this decrease in Young's modulus using both equations.

The individual layers of the sample stack experienced cyclic stresses due to flexure during thermal cycles. The expansion of DBC was more than Si die due to its larger form factor and CTE. Particularly, the solder edges remained unconstrained and hence flexed more making the Cu layer prone to delaminate from the AlN layer. However, the solder centre was heavily constrained by both DBC and Si. During cooling, the CTE mismatch between DBC and Si formed a high density of micro-cracks at the centre, which in turn weakened the Cu layer under the solder followed by the delamination from the solder interface. Currently, the authors are developing a microstructure-based finite element model to accurately demonstrate the temperature dependence on flexure and stress state within the various layers of the sample stack.

Summary

The microstructural and mechanical properties of the sintered nano-Ag bonds were characterized. Homogenously distributed pores were observed at the cross-section of the bond line. 15–20 MPa shear strength was observed and the fractography analysis revealed the occurrence of fracture through the solder thickness indicating good bonding at both the Si/solder and solder/DBC interfaces. 3D X-ray tomography scans showed both macro and microscopic pores present in the initial microstructure (up to 35%) due to entrapment of the organic binder in the solder paste. The micro-cracks were formed during thermal cycling and localized failure via delamination occurred as the crack density exceeded 30%. Warpage due to CTE mismatch between the multiple layers in the solder joint was assumed to be the reason for degradation at the centre of the sample and as a result, higher stresses and crack formation were mainly observed there. A minor crack formation was observed at the outer edges of the solder.

Digest of
Regalado IL, Williams JJ, Joshi S, Dede EM, Liu Y, Chawla N; X-ray microtomography of thermal cycling damage in sintered nano-silver solder joints; Advanced Engineering Materials 2019;21, 1801029.
https://onlinelibrary.wiley.com/doi/epdf/10.1002/adem.201801029

3D Grain Reconstruction from Laboratory Diffraction Contrast Tomography

Bachmann F, Bale H, Gueninchault N, Holzner C, Lauridsen EM

Introduction

Non-destructive volumetric orientation imaging techniques based on X-ray diffraction microscopy have been widely used to study spatio-temporal relationships between crystallographic microstructure and material behaviour of polycrystalline materials. Particularly, monochromatic high-energy parallel synchrotron beam 3DXRD and high-energy diffraction microscopy are techniques developed at and remain accessible at synchrotrons. These methods typically allow us to determine the grain maps describing grain-averaged orientation, intra-granular orientation, shape, size, strain, etc. More recently, these methods have been implemented using polychromatic divergent X-ray tubes on laboratory X-ray microscopes, allowing to obtain the grain centroid and crystallographic orientations. However, the grain shape and morphology is then typically modelled and estimated via algebraic reconstruction techniques. Fast geometric indexing is a versatile reconstruction diffraction model presented in this study for grain mapping, where individual grain scattering contributions are treated independently and the acquired data are reduced to binarized diffraction contrast patterns. To optimize the crystallographic orientation for each grain, the diffraction geometry is rigorously exploited by systematic traversing of the sample space followed by successive indexing and grain by grain mapping. This tailors the implementation of the reconstruction scheme resolving grain morphology and crystallographic orientation, particularly for LabDCT data.

Fast geometric indexing – data acquisition and implementation

A ZEISS Xradia 520 Versa X-ray microscope, equipped with a specialized LabDCT imaging modality, has been used for grain mapping. Figure 1 shows the LabDCT setup, where the sample is placed on a micro-positioning rotation stage equidistant from the transmission-type micro-focus tube producing a polychromatic white cone beam source and the detector. An aperture mounted in front of the X-ray source defines a narrow cone beam that limits illumination to just the sample. Further down the X-ray beam, an in-line beam-stop shields the high-sensitivity scintillator from overexposure by the direct X-ray beam, there by allowing diffracted signals to be recorded at enhanced contrast in the remaining part of the scintillator. The first step of data acquisition is to determine the illuminated sample volume using conventional absorption contrast tomography, where symmetric 1:1 distance ratio corresponds to a geometric magnification of factor 2. The second step includes determining the same illuminated volume via diffraction contrast tomography with the identical acquisition geometry, and recording diffraction contrast patterns (usually >181) acquired by rotating the sample once ~2° or finer steps. The elongated diffraction spots are formed on the detector due to the Laue-focusing effect and a higher number of Laue spots can be recorded with less overlap and a higher signal-to-noise ratio on the same projection. Adjusting the illuminated volume and pattern quality by using different-sized apertures and beam stops can control the information of diffraction contrast patterns formed on the detector.

The acquired experimental data is used to extract the scattering volume via standard segmentation methods. The extraction of binarized diffraction contrast patterns from the raw projection images consists of background correction, exclusion of the beam stop area, followed by a binarization of the pre-corrected diffraction contrast patterns using a Laplacian of Gaussian segmentation approach, which in turn influences the reconstruction quality. Usually, >15 reciprocal-space vectors correspond to three (BCC) or four (FCC, HCP) strongest {hkl} lattice plane families are required for indexing, i.e. to produce a reliable grain map that identifies any possible pseudo-twin orientations. This fast geometric indexing reconstruction algorithm is discretized on a voxelated volume of arbitrary choice, where a top-down hierarchical cubic close-packing subdivision into a set of levels is used to recognize the set of locations to be traversed systematically. This reconstruction is successively refined level by level and this procedure is implemented in the workflow-based commercially available software package GrainMapper3D.

Fast geometric indexing – grain mapping and algorithm

Please refer to the full version of this article for further insights into the mathematical description of the reconstruction algorithm.

Results and discussion

To demonstrate the capabilities of LabDCT using the reconstruction algorithm, a cylindrical aluminium rod (1400 micrometers gauge diameter) having grain boundaries decorated with copper was chosen as a model material system. A standard pin vise was used to mount the sample on the rotational stage being positioned 14 mm away from both source and detector, and the scans were performed at 160 kV accelerating voltage and 62 mA current. Both absorption and LabDCT scans were acquired with 1601 projections of 1s exposure time and 181 projections collected at 2° steps with 300s exposure time respectively as illustrated in Figure 2. The absorption and LabDCT scan volumes were 380 µm × 1100 µm and 0.573 mm of the aluminium rod respectively. The {111}, {200}, {220} and {311} lattice planes were selected for indexing with 4, 3, 6 and

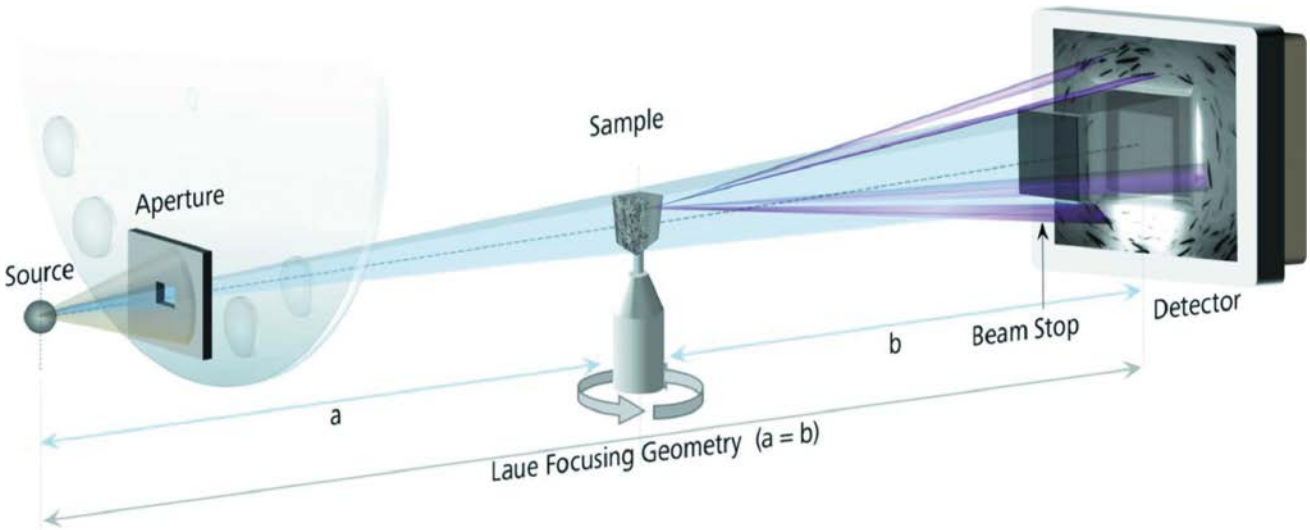

Fig. 1: *Setup of the LabDCT imaging modality.*

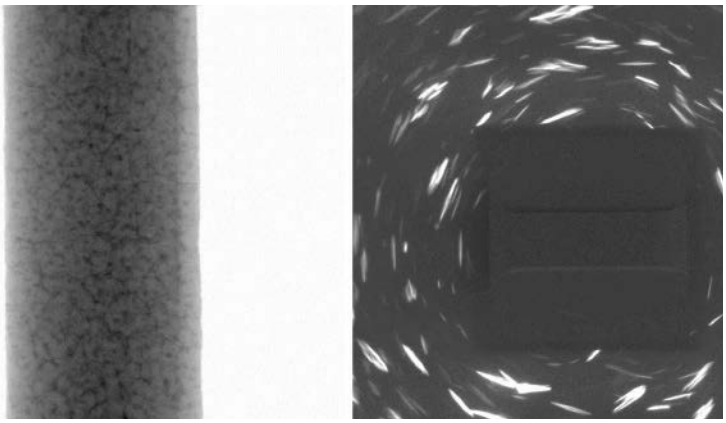

Fig. 2: *(Left) Acquired absorption projection and (right) diffraction contrast pattern.*

12 reciprocal-space vectors respectively. The initial reconstruction was based on the instrument calibration, which was further improved via self-consistent fitting and minimization of the residuals between observed and forward simulated diffraction spots.

Figure 3 shows the reconstruction performance of different levels using the reconstruction parameters trust completeness c_{trust} = 85%, minimum completeness c_{min} = 45% and drop-off = 2% for 5 µm and 10 µm voxel edge lengths. The reconstruction algorithm starts with coarse sampling from top-level L7 and refined sampling is continued up to down-level L2 till a gradual filling up of volume with reconstructed grains is noticed. Most information on the reconstructed crystallographic microstructure is gained after completing indexing of level L4, where more than half of all voxels have a completeness >80%. Figure 4 shows a good agreement along grain boundaries after overlaying the absorption contrast data of Al-Cu sample with 168 µm average spherical grain diameter on top of the LabDCT reconstruction. The forward-projected outline of the first four lattice planes used for indexing of grain boundaries in the reconstructed microstructure describes most of the binarized diffraction spots and reveals a good agreement in position, size, and shape. Generally, low-angle grain boundaries are found not to be decorated with Cu and thus can only be revealed by LabDCT. Grain clusters with low-angle grain boundaries above ~0.05° can be distinguished, clearly separated, and validated in the forward projection as observed in Figure 5.

As the reconstruction scheme is formulated in a general framework and independent of the acquisition geometry and X-ray spectrum used, thus it could be adapted to the classical synchrotron 3DXRD or DCT techniques, where parallel monochromatic beams are used instead of a polychromatic beam. However, a polychromatic beam forms more complex diffraction contrast patterns and reveals more information captured simultaneously than a monochromatic beam, therefore grain size, mosaicity, and lattice deformation can significantly limit the use of classical synchrotron technique in this case. Typically LabDCT is capable to resolve only 2 – 3 times higher spherical grain diameter than a synchrotron DCT and this corresponds to a minimum grain size of >20 – 40 µm depending on the diffracted intensities. The Laue-focusing effect enables the elongation of the diffraction spots and maintains an acceptable degree of spot overlapping allowing up to 400–500 grains to be illuminated. The diffraction spots become extractable and separable on the detector after a certain point. A reduction of illuminated volume also limits the lattice defects, deformation, and mosaicity that affects the pattern quality. The increase in angular sensitivity due to Laue-focusing geometry can resolve sub-grain boundaries >0.05–0.1° by adjusting working distances, sample, and grain sizes. Thus appropriate binarization of the diffraction contrast patterns is a critical step to avoid any over or under segmentation jeopardizing the completeness. Overall, the well-established absorption tomography reconstruction shows a good agreement with and is complemented by this LabDCT reconstruction scheme.

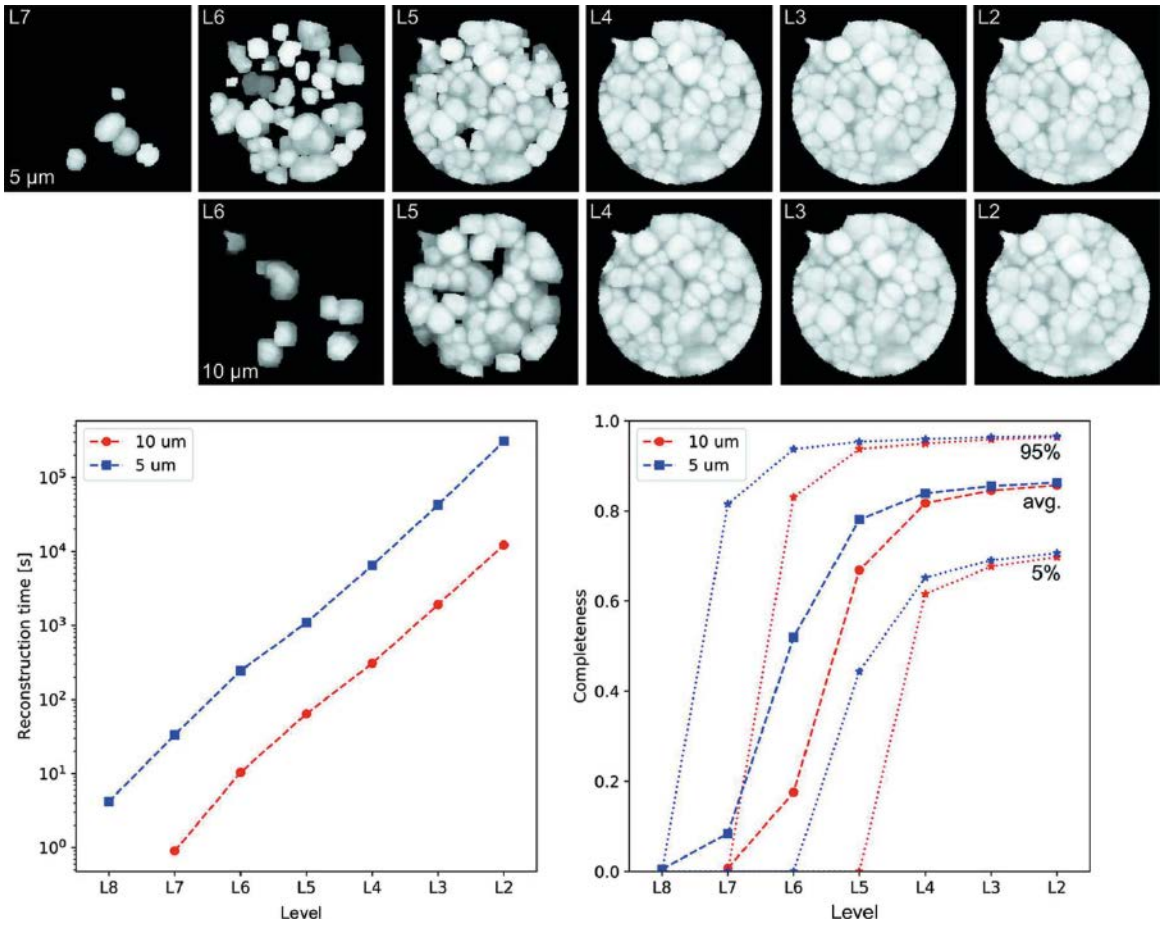

Fig. 3: (Top) Completeness maps with 5 and 10 µm resolution through reconstruction levels L7 to L2 and their corresponding (bottom left) reconstruction time and (bottom right) average completeness, 5 and 95% completeness percentiles.

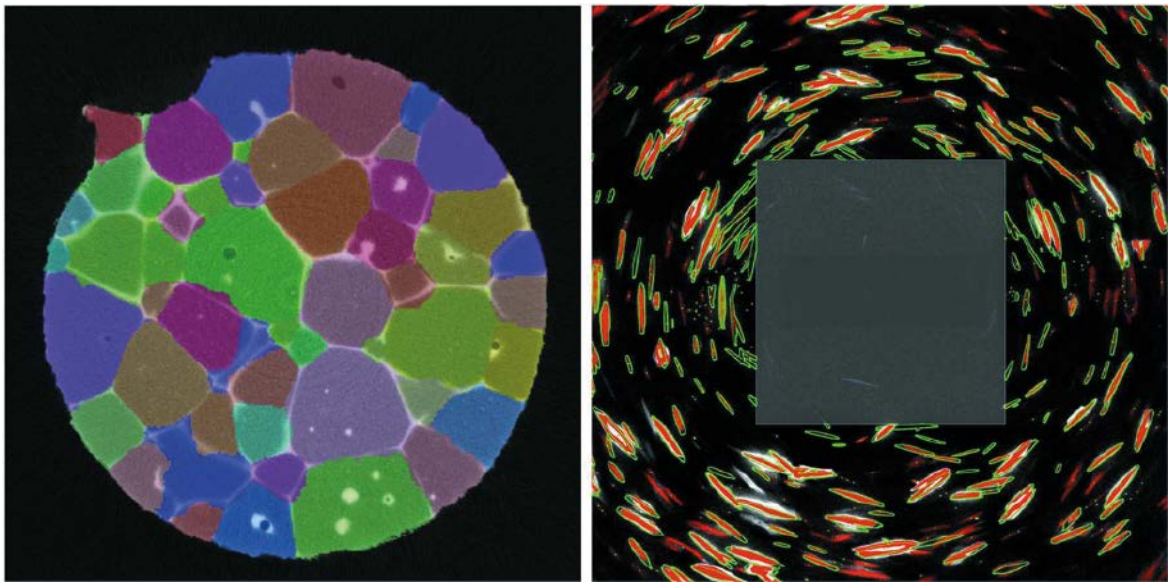

Fig. 4: (Left) Overlay of absorption and colour-coded LabDCT reconstruction and (right) binarized diffraction images (red) and forward-projection outline (green) of the diffraction spot.

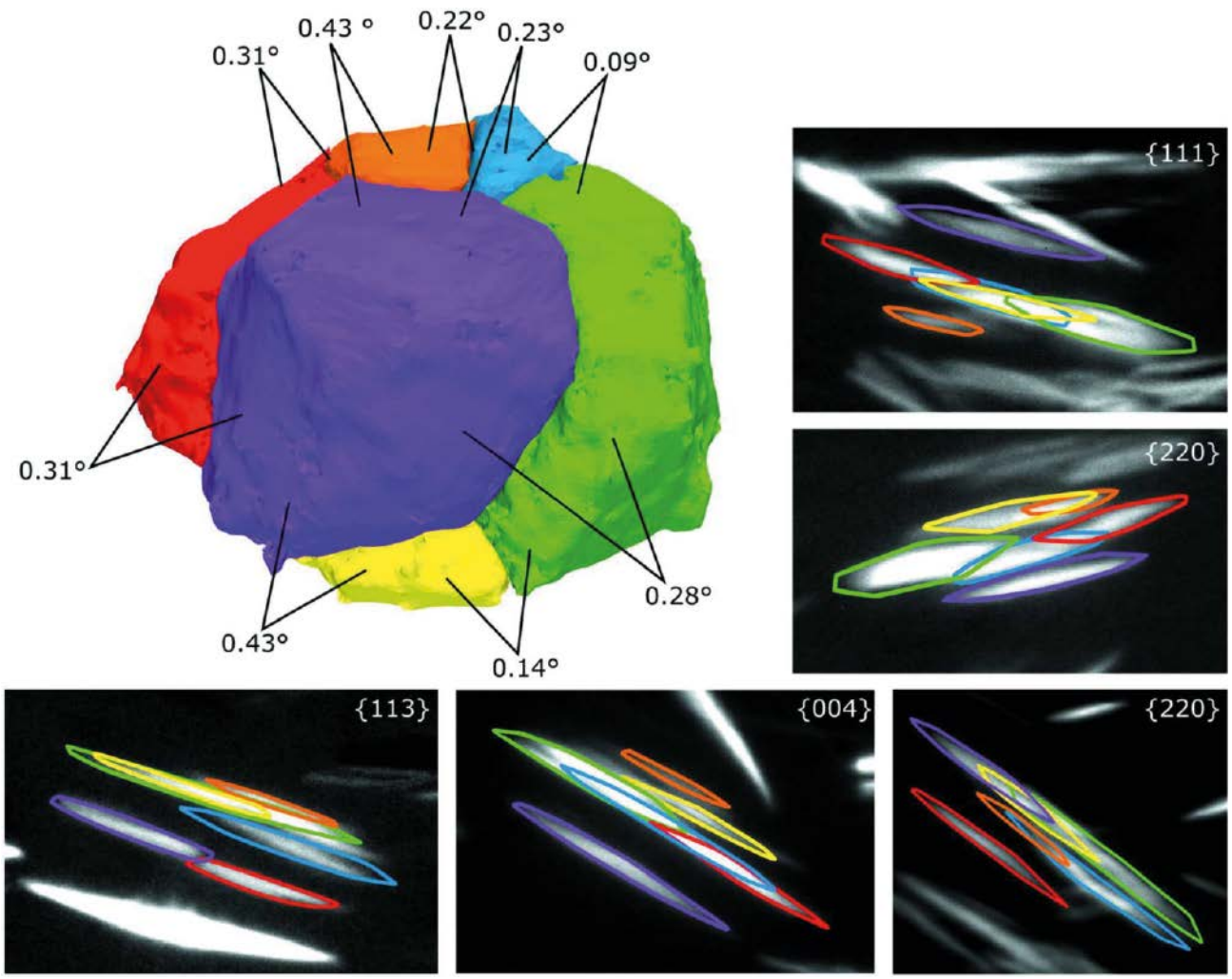

Fig. 5: Grain cluster with low-angle grain boundaries and samples of their forward-projected convex hulls, coloured according to the grain.

Summary

A versatile fast geometric indexing reconstruction scheme is discussed to capture the crystallographic orientation and morphology of a polycrystalline microstructure via LabDCT. Laue-focusing geometry is used to record the diffraction contrast patterns, which expose the grain shape information. The correctness of this information is further verified using an absorption contrast reconstruction and large grain maps can be stitched together from several reconstructions. Both absorption and phase contrast reconstructions can be combined with the LabDCT reconstruction enabling correlative analysis and this reconstruction scheme successively traverses and refines solution space until a realistic reconstruction is reached. The LabDCT implementation concludes the gap to synchrotron grain mapping and produces fast and efficient results.

Digest of
Bachmann F, Bale H, Gueninchault N, Holzner C, Lauridsen EM; 3D grain reconstruction from laboratory diffraction contrast tomography; Journal of Applied Crystallography 2019, 52.
https://onlinelibrary.wiley.com/iucr/doi/10.1107/S1600576719005442

Advanced Microscopy Characterization of Metals and Alloys

An Interview with Kaoru Sato

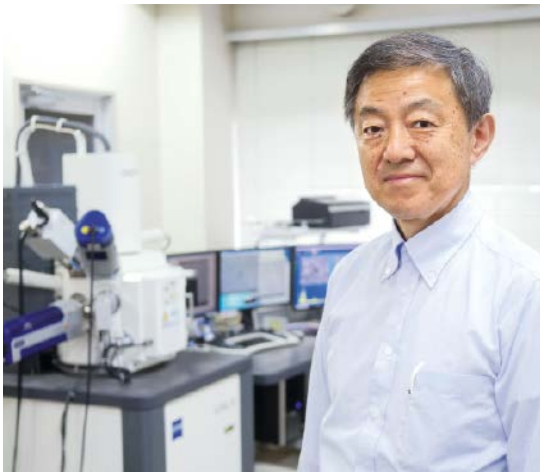

Kaoru Sato joined Nippon Kokan KK (NKK, predecessor of JFE Steel) in 1981. After he received a PhD from the University of Cambridge, UK, in 1989, he worked at JFE Steel as the General Manager of the Analysis & Characterisation Research Department. In 2011 he advanced to Principal Researcher at JFE Steel Corporation. From 2016 onwards, he has worked as a fellow of JFE-TEC, specializing in electron microscopy and microbeam analysis of material/surface design. He is also actively engaged in advanced analysis using synchrotron radiation and neutrons.

Here Dr Sato draws on his years of experience to share with us his views on current key issues in metal and alloy analysis, together with his expectations for the future.

Dr Sato-San, it seems like there is a strong momentum in the field of traditional metals and alloys, with research interest picking up both in academia and industry. Can you share your view about the driver for such a strong push?

When I give a talk on metals/steel to non-experts, I often quote Sir Alan Cottrell's remark:[1]

"Above all, there remains the continuing challenge of steel. For many reasons - an abundance of rich and reducible ores, high intrinsic strength and melting point, ease of alloying and richness of phase transformation behaviour - steel remains by far the best source of cheap, reliable tensile strength, and is unlikely ever to be overtaken in this 'mass-market' role."

It's encouraging that scientists are studying so called nano-tech materials such as carbon-nanotubes or cellulose nanofibres however it is unlikely that these materials will be used to a large degree in, for example, automobile production for several more decades. Demands for metal and steel are huge: developing countries need more steel. Not only the quantity but also the quality is vital. An article on Tokyo Skytree[2] highlights how the development of steel contributed to construction of this piece of modern architecture.

Limited amounts of rare metals and precious metals are available, and new alloy designs are vital to minimize the use of those metals for heat-resistant metals, magnets and catalysts.

In your opinion, what are the burning issues within the metals and alloys that are being addressed by academic and industrial researchers?

Our understanding of metals and alloys is still limited and the scope for future study is vast. Recent investigations suggest a new deformation mechanism for magnesium alloys. High-entropy alloys are of high interest among academia. We need an in-depth knowledge to make various materials with minimum addition of rare metals or precious metals. The role of H, B and C in steel is yet to be studied.

What do you consider as the significant milestones in the development of imaging technology for materials characterization that have and will continue to impact traditional metals research?

Imaging sciences have seen great advancement in this last half a century. Bright pri-

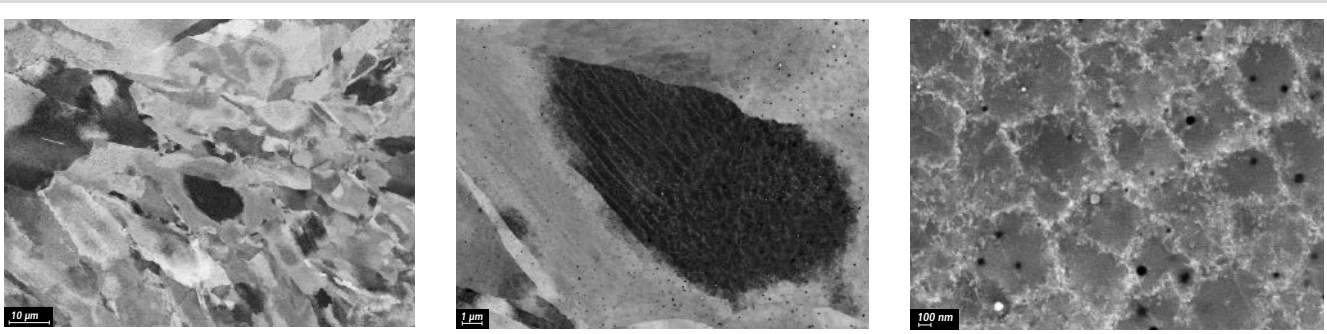

See the wood and the trees: Application to additive manufactured 316L stainless steel. Electron channelling contrast image (ECCI) reveals inhomogeneous strain distributions at low (left) and medium (centre) magnifications. Dislocation cell structures are discerned at high magnification (right).

mary beams, such as filed-emission gun and synchrotron sources, are routinely used today. Aberration correction in TEM and beam-deceleration optics, together with in-lens image detection in SEM, have dramatically improved the power of electron microscopy. We have strengthened our knowledge of atomic, interface and surface microstructures. Enhancements in light elements such as H, Li, B and C detection, detection and visualization of low-concentration elements in alloys, 3D imaging and *in situ* capabilities will give additional value to electron microscopy.

What are the benefits of your research with regard to the engineering materials supply of the future? What visions do you have for this?

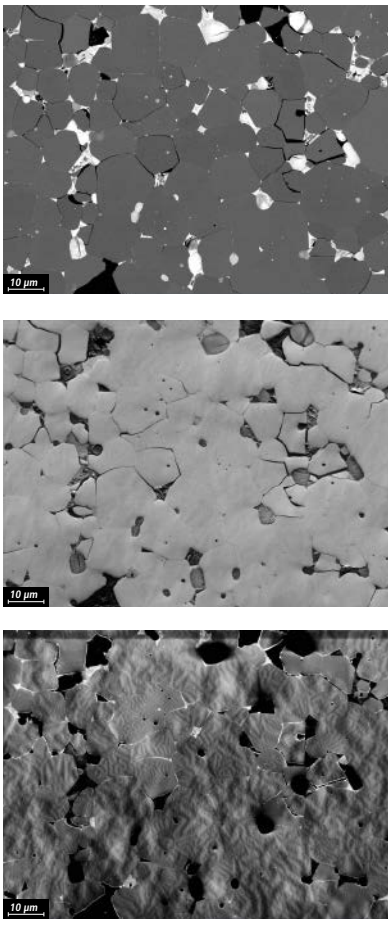

Power of multiple detectors: Application to Fe-Nd-B magnet. In-lens backscattered electron, E-T and In-lens secondary electron detectors give compositional, topographic and magnetic contrast, respectively (from top to bottom).

My motto is "What cannot be seen or measured cannot be controlled", and this appears on the JFE-TEC webpage. I have a strong belief in observational science. Unless you understand or measure, you are not able to control. Let me emphasize that "It is not easy to find something in the total darkness, Microscopy is like light."

SEM is truly a powerful method. It allows observations from below x100 to above x100,000, thus you can see the wood and the trees, which is very important for engineering materials. We have been promoting imaging at the "sweet spot". In this context the ZEISS Gemini column was an eye-opener. This innovative instrument is giving new insights into understanding microstructure by providing unique image contrasts.

Through use of enhanced imaging and the analytical capabilities that I mentioned in the previous section, we will be able to contribute to sustainable development goals (SDGs) by designing alloys with minimum environmental loads.

You work extensively with electron microscopy and microbeam analysis. What advantages does this method offer you in your work and which areas of application have not yet exhausted the potential of this technology in your opinion?

Materials properties (e.g. mechanical and electrical properties) are governed by microstructure. Consequently, chemical bulk analysis alone cannot elucidate properties. A variety of methods using electrons, X-rays and neutrons can be successfully applied to the understanding of both hard and soft materials.

JFE-TEC work with many clients in the field of heat-resistant alloys, batteries, magnets and catalysts in order to achieve SDGs.

Atomic-level characterizations have become routine and they are contributing to material design. However, our challenges continue: we want to see atoms in motion, how materials break or corrode, and how the structure changes at elevated temperatures.

What has been your most important insight into metals and advanced materials technology to date, where modern imaging methods have served you well?

We have succeeded in developing novel steel products, including high-strength and high-formability steel and excellent press-formability surface coatings. Both TEM and SEM have played a crucial role in this development. It is indeed the nanostructure that governs properties. We are proud that we can stably produce nanostructure-controlled steel products in large volumes.

JFE-TEC have been promoting imaging at the "sweet spot". Apart from topographic information, SEM can give richer information provided you optimize the signal detection. This technique gives true surface information and a quick-and-handy assessment of precipitates in heat-resistant alloys.

What expectations do you have of equipment and software development with regard to the further improvement of microscopic analyses in your research area?

In situ/*operando* observation for both dry and wet specimens should be strengthened. Light elements and minor elements detection are another issue. To achieve this goal, further integration of the microscope and analytical instruments/*in situ* attachment will be crucial. Microscope manufacturers and analytical instruments companies should work more closely together in order to optimize their instruments.

Today we are dealing with more and more data: Giga-sized image acquisition has become routine, and we cannot inspect such huge data manually. AI or machine learning and implementation of automatic data inspection are strongly required.

Further integration of microscopes and analytical instruments will come. This will improve, for example, the detectability of low-concentration elements. Automated image acquisition and inspection of high-precision micrographs will be realized. Stored images will be archived and utilized as large databases.

References

[1] Pettifor DG, Cottrell A. Electron Theory in Alloy Design. Institute of Materials, 1992. ISBN 10: 0901716170, ISBN 13: 9780901716170

[2] Bringing neutrons into industry. Physics World, October 2017. https://physicsworld.com/a/bringing-neutrons-into-the-steel-industry/

JFE-TEC Gemini team in Kawasaki.

Linking materials performance to microstructure

In Situ Lab for ZEISS FE-SEM

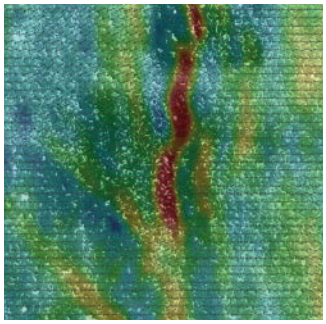

Implement unattended automated in situ workflows with the in situ lab for your ZEISS FE-SEM. Combine a tensile or compression stage, a heating unit, and high-temperature detectors with EDS or EBSD. Control all components from a single PC. Collect highly reproducible, precise, and reliable data with high throughput. Create statistically representative results. Process your data using digital image correlation.

zeiss.com/fesem-insitu

ZEISS

Seeing beyond

From nano to macro in femtoseconds.

ZEISS Crossbeam laser

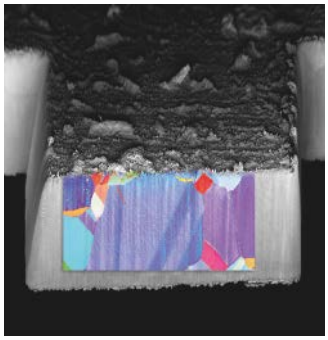

The LaserFIB enhances your *in situ* studies. Gain rapid access to deeply buried structures, if needed guided by X-ray microscopy data in a multi-modal setup. Prepare cross-sections up to mm in width and depth for EBSD within minutes. Machine meso-scale large structures for mechanical tests. Minimize sample damage and avoid contamination of your FIB-SEM chamber as you perform work with the femtosecond laser in a dedicated chamber.

zeiss.com/crossbeam

ZEISS

Seeing beyond